The Pennsylvania State University

The Graduate School

Department of Engineering Science and Mechanics

A SOLVENT-FREE COARSE-GRAINED MODEL FOR BIOLOGICAL AND BIOMIMETIC FLUID MEMBRANES

A Dissertation in

Engineering Science and Mechanics

by

Hongyan Yuan

© 2010 Hongyan Yuan

Submitted in Partial Fulfillment
of the Requirements
for the Degree of

Doctor of Philosophy

August 2010

The dissertation of Hongyan Yuan was reviewed and approved* by the following:

Sulin Zhang
Assistant Professor of Engineering Science and Mechanics
Dissertation Advisor
Chair of Committee

Peter J. Butler
Professor of Bioengineering

Long-Qing Chen
Professor of Materials Science and Engineering

Bruce J. Gluckman
Associate Professor of Engineering Science and Mechanics and Neurosurgery

Bernhard R. Tittmann
Professor of Engineering Science and Mechanics

Judith A. Todd
Professor of Engineering Science and Mechanics
Head of the Department of Engineering Science and Mechanics

*Signatures are on file in the Graduate School

ABSTRACT

Mechanics of biological membranes is involved in numerous intriguing biophysical and biological cellular phenomena of different length scales. On the length scale much larger than the membrane thickness, fluid bilayer membranes or biomimetic membranes, from the mechanics viewpoint, can be simplified as “thin fluid shells” with their mechanical behaviors dictated by only a few effective mechanical properties such as bilayer membrane bending rigidity, area compression modulus, in-plane viscosity, line tension between two different components, and spontaneous curvature. Solving mechanics problems of the fluid membranes with complicated shapes or multi-components in static or dynamic conditions largely resorts to computer simulations. There are two approaches to establish a simulation model for fluid membranes at the large length scale. One is the numerical implementations of the continuum membrane models. The other is the highly coarse-grained inter-particle interaction-based membrane simulation models. One of the drawbacks of the former class of models is that extra or dedicated computational effort is needed to take into account the in-plane fluidity and topological changes. Conversely, the latter class of models can naturally capture the in-plane fluidity and viscosity, and simulate topological changes. On the other hand, the disadvantage of the inter-particle interaction-based models is that they suffer length scale limitations due to the small intrinsic particle size, which is not the case for the former class of models.

In this study, we established a one-particle-thick fluid membrane model, where each particle represents a cluster of lipid molecules. The model features an inter-particle pair potential with the interaction strength weighed by the relative particle orientations. The model is solvent-free, and the orientation dependence of the inter-particle pair potential substitutes for the hydrophobic effect. Particles can robustly self-assemble into fluid membranes with experimentally relevant membrane properties such as bending rigidity. Three potential parameters separately and effectively control diffusivity, bending rigidity, and spontaneous curvature of the model membrane. The high level of coarse-graining and the efficiency of the model enable the studies of large-scale membrane problems that are typically not accessible by previous coarse-grained models.

This model is well suited to study the mechanics of both homogeneous and heterogeneous fluid vesicles, such as morphology and shape changes in static or dynamic situations. In order for this solvent-free membrane model to be biologically or experimentally relevant in the fluid vesicle case where the vesicle volume is controlled by the osmotic pressure, the membrane model is extended to the fluid vesicle case by incorporating a volume-control algorithm based on an external potential associated with vesicle volume. The instantaneous volume of the vesicles is calculated via an efficient, accurate and robust local triangulation algorithm. The shape transformation pathways produced by the present model agree strikingly well with previous experimental data. Furthermore, we have studied very first the non-equilibrium behaviors of fluid vesicles under different volume-change rate. The results show that both the intermediate and equilibrium vesicle configurations depend on the volume-change rate, which manifests the viscous effect of the fluid membrane.

Recently, the membrane-mediated repulsive interactions between liquid-ordered domains in model membranes are believed to play important role in stabilizing the finite domain size. Using the membrane model, we studied the domain growth dynamics on a binary fluid vesicle. The both normal and slow domain growth dynamics observed in the experiments was reproduced in our simulations. The results show that the repulsive interactions depend on domain size and domain curvature. As budded domains grow bigger, the repulsive energy becomes comparable to the thermal energy and thus set an energy barrier to slow down approaching and further coalescence of domains.

The membrane model developed in this thesis research is mathematically and physically easy to follow, of the highest level of coarse-graining with the inter-particle interaction, and naturally includes the various key mechanics elements of fluid membranes such as in-plane fluidity and viscosity, out-of-plane bending rigidity, line tension, edge energy, topological changes, effective spontaneous curvature, thermal fluctuations. The model provides a computationally reliable and powerful alternative to experiments and continuum theories for the study of large-scale fluid membrane mechanics. In addition, the model itself provides a simple model system for 2D self-assembled membranes in the mesoscopic scale, and thus can help understand the fundamental aspects of the condensed soft matter physics of self-assembled membranes, similar to the Lennard-Jones potential for 3D condensed matter physics.

TABLE OF CONTENTS

LIST OF FIGURES viii

LIST OF TABLES xii

ACKNOWLEDGEMENTS xiii

Chapter 1 Introduction 1

Chapter 2 Review of membrane models from atomic to continuum scale 4

- 2.1 Atomistic simulations 7
- 2.2 Mesoscopic membrane models 8
  - 2.2.1 explicit-solvent coarse-grained models 9
  - 2.2.2 solvent-free coarse-grained models 10
  - 2.2.3 “Aggressive” solvent-free coarse-grained models 11
- 2.3 Continuum scale modeling 12
  - 2.3.1 Theoretical modeling 13
  - 2.3.2 Numerical implementations 17

Chapter 3 The coarse-grained membrane model 19

- 3.1 The anisotropic inter-particle pair potential 19
- 3.2 Molecular dynamics simulation algorithms 25
  - 3.2.1 Equations of motion 25
  - 3.2.2 Tension and temperature coupling algorithms 26
- 3.3 Model membrane properties 28
  - 3.3.1 Self-assembling 28
  - 3.3.2 Phase diagrams 29
  - 3.3.3 Bending rigidity and area compression modulus 36
  - 3.3.4 Spontaneous curvature 40
  - 3.3.5 Length and time scale mapping 41
- 3.4 Volume-control algorithm for fluid vesicles 43
- 3.5 Cauchy-Born analysis and zero-temperature properties 46

Chapter 4 Configurations of fluid vesicles 50

- 4.1 Static shape transformations 51
- 4.2 Dynamic shape transformations 55
- 4.3 Conclusions 58

Chapter 5 Domain growth and interactions in a fluid vesicle 60

- 5.1 Introduction 60
- 5.2 Simulations and preliminary results 63

Chapter 6 Conclusions and future work 69

- 6.1 Conclusions 69
  - 6.1.1 The membrane model 69
  - 6.1.2 Non-equilibrium shape transformations of fluid vesicles 70
  - 6.1.3 Membrane mediated interactions between domains 71
- 6.2 Future work 71
  - 6.2.1 Membrane fluctuations 71
  - 6.2.2 Domain diffusion on a non-Euclidian 2D space 72
  - 6.2.3 Simulating nanoparticle endocytosis 73
  - 6.2.4 Extending the model to dissipative particle dynamics 73
  - 6.2.5 Parallelizing the MD code 74

Appendix 75

- A1 Euler's equations of rigid body dynamics 75
- A2 Implementation of Nose-Hoover thermostat 76
- A3 Membrane tension formula in one-particle-thick fluid membranes 79
- A4 Removal of rigid body motion 81
- A5 Derivations for inter-particle forces 81

References 84

LIST OF FIGURES

Figure 1.1. Animal cell schematic. The plasma membrane separates the cell interior from its outside. Biological membranes also compartmentalize the intracellular space, which gives rise to various membrane-bound intracellular organelles such as endoplasmic reticulum, Golgi apparatus, mitochondrion, and nucleus. It is interesting to mention that in such a small world, as pointed out early by Purcell [9], the Reynold number for motions of structures inside the cell is small, therefore microorganisms feel water much more "viscous" than animals in the macroscopic world. Since inertial effect is neglect at low Reynold number, Aristotle's mechanics is correct: velocity is a constant and proportional to the pulling force. (This image is from *wikipedia.org* under Entry "Eukaryote". This image has been released into the public domain by its author, LadyofHats.) 2

Figure 2.1. Schematic of a lipid bilayer membrane in an atomistic view. The carbon atoms are blue. The oxygen atoms are red. (a) A single lipid with a polar head group and two apolar hydrocarbon tails. (b) Lipid molecules in a water solution, hydrophobic tails are hiding from water molecules, polar head regions contact with water molecules. (c) Lipid molecules are horizontally shifted to see the hydration region of the lipid bilayer. 6

Figure 2.2. Membrane simulation models. (a) all-atom model of the DMPC lipid molecules; (b) a 10-particle coarse-grained model; (c) a 3-particle coarse-grained model. (d) one-particle-thick membrane models; (e) numerical methods based on continuum models (mesh elements) 8

Figure 2.3. A Monge representation of a 2D membrane. 14

Figure 3.1. Schematics of inter-particle interactions. Kinetically, each particle is axisymmetric with a particle-fixed unit vector $\mathbf{n}$ representing the axis of symmetry and a mass of m. The inter-particle interaction is both distance- and orientation-dependent. The angle θ_0 is a model parameter charactering the spontaneous curvature. The configuration at $\theta_i = \theta_j = \theta_0$ corresponds to the energetically most favorable relative orientation between two particles. The two halves of each particle are colored distinctly to indicate the orientation of the particle. 20

Figure 3.2. The distance-dependent function $u(r)$ consisting of a repulsive branch and an attractive branch. The slope of each branch can be tuned by changing the empirical exponents η (repulsive branch) and ζ (attractive branch). Both η and ζ affect particle diffusivity. The solid curves correspond to $\eta = 2$ and $\zeta = 4$, which are the representative values used in the most simulations later. 22

Figure 3.3. The orientation-dependent inter-particle pair potential U as a function of r for three different θ_i ($\theta_j = \theta_i$) with η=2, ζ=4, μ=3, θ_0=0. The double arrows denote the orientations of a particle pair. 23

Figure 3.4. The functional dependence of a on θ_i and θ_j at $\theta_0 = 0$ shows the energetically favored and disfavored relative orientations of particles i and j. Both the 3D and 2D energy contours are plotted in the figure. A larger a corresponds to a lower interaction energy. 24

Figure 3.5. Snapshots from CGMD simulations demonstrating self-assembly of randomly distributed particles into vesicles. The parameters used in the simulations are ζ=4, μ=3, θ_0=0, and $k_B T = 0.17\varepsilon$. The two halves of each particle are colored distinctly to indicate its orientation, which facilitates visual observation of results. 29

Figure 3.6. Particle diffusion in the lateral direction, (a) initial configuration, (b) configuration after a certain period of time. 30

Figure 3.7. Phase diagram in the (ζ, T) plane at zero-tension. Three regions representing gel, fluid, and gas phases are identified, separated by solid lines. A broad fluid phase region with diffusion constant on the order of $0.1\,\sigma^2/\tau$ exists. 34

Figure 3.8. Diffusion constant D and inter-particle distance d as functions of the exponent ζ ($k_B T$=0.2ε) for tensionless membranes. 34

Figure 3.9. Diffusion constant D and inter-particle distance d as functions of the exponent η ($k_B T$=0.23ε) for tensionless membranes. 35

Figure 3.10. Diffusion constant D and inter-particle distance d as functions of temperature for tensionless membranes. The thermal expansion coefficient α_T of the membrane at different temperature ranges is fitted. 36

Figure 3.11. Fluctuation spectra under zero and finite tensions for planar membranes. Both q^{-4} and q^{-2} dependences are well predicted in simulations.

The parameters used in the simulations are ζ =4, μ =3, θ_0 =0, and $k_B T$ = 0.23 ε 37

Figure 3.12. Membrane bending rigidity (in zero-tension states) monotonically increases with μ, while the order of alignment of the axis of symmetry of particles monotonically decreases with μ. Other parameters used in the simulations are η =2, ζ =4, θ_0 =0, and $k_B T = 0.23\varepsilon$ 38

Figure 3.13. Membrane tension as a function of area strain $\Delta A/L^2$. Area compression modulus K_A is fitted to be about $18\,k_\mathrm{B}T/\sigma^2$. The parameters used in the simulations are ζ =4, μ =3, θ_0 =0, and $k_B T = 0.23\varepsilon$ 40

Figure 3.14. Spontaneous curvature (related to the model parameter θ_0) induced budding domains.......... 41

Figure 3.15. Schematics of the local triangulation algorithm.......... 45

Figure 3.16. Invoking the Cauchy-Born hypothesis to analytically derive the relationships between the effective properties of the model membrane and the inter-particle potential parameters. (a) Biaxial stretch λ, (b) bending to curvature c. 47

Figure 3.17. A flat membrane (a) and a membrane tube (b) of 2D hexagonal close-packed lattice.......... 48

Figure 3.18. The bending rigidity of the zero-temperature membrane.......... 49

Figure 4.1. Shape change pathways of fluid vesicles induced by the volume change. The vesicle volume was controlled by adding salt into the solution. Reprinted with permission from [118]. Copyright 2008 American Physical Society. 51

Figure 4.1. Map of vesicle equilibrium shapes and shape transformation pathways. The upper pathway branch ($\theta_0 = 3.4^\mathrm{o}$): sphere, prolate, dumbbell, and outward budding (or tubular) shape for slow (or fast) volume change rate; the lower pathway branch ($\theta_0 = -2.3^\mathrm{o}$): sphere, biconcave, stomatocyte, and inward budding; the central pathway branch ($\theta_0 = 0^\mathrm{o}$): spherical, prolate, and dumbbell shapes, and then bifurcates into two sub-pathways. A slow volume change rate promotes dumbbell to tube shape transformation; for fast volume change rate, the vesicle follows a biconcave-stomatocyte-inward budding transformation pathway. The biconcave shape cannot be directly induced from the dumbbell shape, but from the spherical shape.......... 53

Figure 4.2. Changes of the hydrostatic pressure (a) and average membrane tension (b) with vesicle volume. 55

Figure 4.3. Effect of the volume-change rate on the vesicle shape transformation pathways. Top panel: shape transformation pathway for fast volume-change rate ($\dot{v} = 1.75 \times 10^{-3} \tau^{-1}$); bottom panel: shape transformation pathway for low volume-change rate ($\dot{v} = 1.94 \times 10^{-4} \tau^{-1}$). 57

Figure 4.4. Stress relaxation in dynamically evolving homogeneous vesicles at different volume-change rates. (a) Shear stress; (b) membrane tension. Note that shear stress is shifted by subtracting the average value, so the resulting average value in (a) is zero. 58

Figure 5.1. Two different coarsening speeds in giant ternary vesicles using fluorescence microscopy. (a) Normal coarsening, (b) slower coarsening. Reprinted with permission from [128]. Copyright 2007 Biophysical Society. 61

Figure 5.2. The membrane morphologies in the flat domain case (a) and the budded domain case (b) and (c). 62

Figure 5.3. The phase separation dynamics. Three rows from top to bottom correspond to three different spontaneous curvature $\theta_0^{\mathrm{AA}} = 0.0^\circ$, $\theta_0^{\mathrm{AA}} = 2.3^\circ$, and $\theta_0^{\mathrm{AA}} = 4.6^\circ$, respectively. 65

Figure 5.4. The cross sections of the vesicles in the simulations, showing curved domains and the deformed matrix membrane. Top row: $\theta_0^{\mathrm{AA}} = 0.0^\circ$, bottom row: $\theta_0^{\mathrm{AA}} = 4.6^\circ$ 66

Figure 5.5. Domain number as a function of time. Three sets of data correspond to different spontaneous curvature of component A. The guide line is $N_d \sim t^{-2/3}$. 68

Figure 6.1. Domain diffusion on a non-Euclidian 2d space. Six snapshots in time sequence (from top to bottom, left to right) show that domains tend to locate in the rim region of the oblate vesicle. 72

Figure 6.2. Simulation snapshots of nanoparticle endocytosis. The snapshots show the sequence of endocytosis of the NP (from left to right): docking, partial wrapping, pinching off. 73

LIST OF TABLES

Table 3.1. The phase diagrams of the diffusion constant on the (T, ζ) plane. The abscissa represents temperature $k_B T$ in units of ε, the y-axis represents ζ. The value in the table elements denotes diffusion constant in units of σ^2 / τ. 31

Table 3.2. The phase diagrams of the diffusion constant on the (η, ζ) plane. The x-axis represents η, the y-axis represents ζ. The value in the table elements denotes diffusion constant in units of σ^2 / τ. 32

Table 3.3. The inter-particle distance d on the (T, ζ) plane. The abscissa represents temperature $k_B T$ in units of ε, the y-axis represents ζ. The value in the table elements denotes d in units of σ. 33

Table 3.4. Membrane bending rigidity on the (T, ζ) plane. The x-axis represents temperature $k_B T$ in units of ε, the y-axis represents ζ. The value in the table elements denotes bending rigidity in units of $k_B T$ 39

ACKNOWLEDGEMENTS

I am indebted to Prof. Sulin Zhang, whom I was lucky enough to have as my advisor, for his constant guidance, encouragement, and support throughout my PhD study. This dissertation would have not been possible without his guidance and encouragement. The knowledge and experience on many aspects of academic research gained through discussion with him are priceless.

I thank my other committee members Prof. Peter J. Butler, Prof. Long-Qing Chen, Prof. Bruce J. Gluckman, and Prof. Bernhard R. Tittmann for their advice, time, and effort as committee members.

I thank all my fellow lab mates Xu Huang, Wentao Liang, and Changjin Huang, who were always encouraging and willing to lend a hand. I also thank Guerau Cabrera and Dr. Jian Zou for helpful discussions.

I thank the Department of Engineering Science and Mechanics and the College of Engineering at Penn State for the financial assistance for attending conferences.

My deep appreciation goes to my wife, son, parents, sister, and brother for their support, prayers, patience, and love.

Chapter 1

Introduction

Molecular and Cellular biophysics and biomechanics, focusing on physical laws obeyed by the smallest living unit of life – cells, cover a wide variety of topics ranging from as small as ions to as large as whole cells. The essential driving force behind the biophysics and biomechanics research is to unravel mechanisms behind biological phenomena, which in turn helps understand the cause of diseases, and develop new therapeutics, biomimetic materials, and diagnostic devices. The intensive biomembrane research over the past half century has greatly advanced our understanding in cellular biology. Many books and review articles on biophysics that pull together findings and ideas made in past decades have been written [1-8] (The reference lists here and hereafter should not be considered as exhaustive).

Cells are an extremely complicated multiscale system involving countless types of molecules and many sub-cellular organizations of various levels (see Figure 1 for a schematic of an animal cell). Modern cellular biologists work on details and view every molecule distinctly, while physicists prefer simple models and aim to draw similarities from differences. Physicists treat multiscale systems by a coarse-graining process which involves establishing models for specific problems as simple as they can by neglecting a certain amount of finer lever details. The multiscale system of cells from atomistic to tens of micrometers provides rich choices for physicists to pick. The challenge is to pick just the right amount details for specific problems.

In a relatively large length scale, cells can be considered to be made of soft matter materials including biomembranes and cytoskeletons. Soft condensed matter physics is an emerging field in biophysics, which addresses a specific group of materials whose physical behaviors can be easily affected by the thermal fluctuations at room temperature. Soft matter materials are large assemblies formed by self-organization of small building blocks (molecules) with multiple weak interactions such as electrostatic interactions, van der Waals interaction, and hydrogen bonding. Consequently, such structures lead to rich phase behaviors and remarkable static and dynamic properties that are essential for the biological systems to react to changes in environment and to adopt changes in different cellular processes.

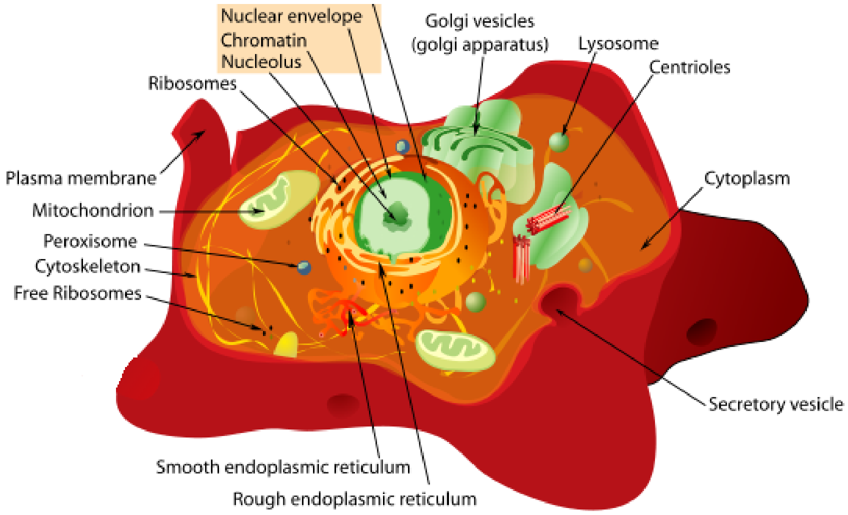
Nuclear envelope
Chromatin
Nucleolus
Golgi vesicles (golgi apparatus)
Lysosome
Centrioles
Ribosomes
Plasma membrane
Mitochondrion
Peroxisome
Cytoskeleton
Free Ribosomes
Cytoplasm
Secretory vesicle
Smooth endoplasmic reticulum
Rough endoplasmic reticulum

Figure 1.1. Animal cell schematic. The plasma membrane separates the cell interior from its outside. Biological membranes also compartmentalize the intracellular space, which gives rise to various membrane-bound intracellular organelles such as endoplasmic reticulum, Golgi apparatus, mitochondrion, and nucleus. It is interesting to mention that in such a small world, as pointed out early by Purcell [9], the Reynold number for motions of structures inside the cell is small, therefore microorganisms feel water much more "viscous" than animals in the macroscopic world. Since inertial effect is neglect at low Reynold number, Aristotle's mechanics is correct: velocity is a constant and proportional to the pulling force. (This image is from *wikipedia.org* under Entry "Eukaryote". This image has been released into the public domain by its author, LadyofHats.)

One may view biological or biomimetic membranes from three different aspects. From the macromolecule viewpoint, they are self-assembled one- or two-molecule-thick membrane-like structure. Due to lack of chemical bonding between amphiphilic molecules, molecules such as lipids or proteins can diffuse in the lateral direction, and membranes can easily undergo topological changes via disassembling and re-assembling, or via microstructure remodeling as in membrane budding. Second, from a fluid mechanics point of view, biomembranes are 2D single- or multi-phased microfluid flowing on a curved moving surface. While from a solid mechanics point of view, they are elastic thin shells but with zero in-plane shear resistance.

In this thesis, within the soft matter framework, we developed a particle-based coarse-grained fluid membrane model that incorporate the abovementioned three aspects naturally based on an orientation-dependent inter-particle pair potential. In the current stage of the model, the surrounding bulk fluid is only implicitly modeled. Thus the hydrodynamic effect of the bulk fluid is neglected assuming the viscosity of the water is much smaller than the membrane. Such a model is well suited to study membrane physics in length scales much larger than the membrane thickness. Although a high level of coarse-graining is adopted in our model, in which much atomic information of constituting molecules is neglected, there are many biological phenomena can be adequately studied and explained using the model. Examples includes: the effect of membrane fluctuations on membrane-substrate adhesion, shape transformations of red blood cells [10] and fluid vesicles [3], sculpting protein-mediated membrane morphology remodeling [11, 12], membrane budding dynamics involved in exo- and endocytosis and viral entry in living cells, phase separation dynamics in multi-component membranes [13], and the effect of membrane elastic interactions on domain stabilization [14].

Amphiphilic block copolymers can also self-assemble into polymersomes of various shapes, which are proven to be much tougher and more flexible than natural membranes [15, 16]. Such synthetic fluid vesicles may find a wide range of applications such as drug delivery and encapsulation. Artificial supported membranes have been proposed to be used as biosensors [17]. In addition, the mechanical properties and responses of the whole cell has been considerably studied in tissue engineering [18]. Biomembranes as one of the two load-bearing building block of cells, the other one being cytoskeleton, play important role in whole cell response to forces and deformations. The fluid membrane model developed in this thesis research is also applicable to those bioengineering topics.

Chapter 2

Review of membrane models from atomic to continuum scale

In this chapter, the membrane simulation models from atomistic to continuum scale are reviewed. Computer simulations of biological membranes are a booming field recently due to the useful insights they can offer to help understand experiment results or to inspire future experiments.

Biological membranes found in living cells, including plasma membranes and intracellular membranes, are composed of a double layer of lipid molecules and membrane-associated proteins. Both lipids and proteins can be of many species [19]. The lipid bilayer is a result of self-assembly of amphiphilic lipids in water due to the hydrophobic effect (see Figure 2.1 for an atomistic schematic of a lipid bilayer in water). Membrane proteins are usually sub-categorized into integral and peripheral membrane proteins, which are the active players performing biological functions. The most salient feature of the lipid bilayer is the low permeability to charged, polar, or large molecules, which makes the lipid bilayer as an excellent chemical and electrical insulator. Serving as a passive barrier, the lipid bilayer separates the cell interior from the outside and compartmentalizes the intracellular space, which is essential for life to be possible. Passively or assisted by membrane proteins, biological membranes provide a regulated transport of substances as small as protons to as large as entire cells. Due to the fast molecular diffusion in the lateral direction, the lipid bilayer is in a fluid phase at physiologically relevant temperatures, which was concluded in the standard fluid mosaic model of biomembranes [20].

With the advances of experimental techniques, the ideas in the fluid mosaic model that proteins are randomly distributed in a lipid sea, and the lipid bilayer merely provide a fluid medium to host proteins, is fading out. Biomembranes are thought to be patchy and heterogeneous [21]. It has been found that the lipid bilayer itself has a functional role in many biological and biochemical processes, such as formation of lateral lipid organizations, lipid-protein hydrophobic mismatch, lipid-peptide interaction, mechanosensation [22, 23], membrane trafficking [24], etc.

Facilitated by both the advances in experimental methods and large-scale parallel computer simulations, biomembrane physics has entered a fully multiscale era. Although lipid bilayer membranes are only about 5 nm thick, the lateral dimensions of a lipid membrane can be up to tens of micrometers, manifesting their truly multiscale nature. Computer simulations of biomembranes, spanning from atomistic to continuum scales, have been successfully utilized to study biomembrane physics. Many membrane simulation models that are tailored to be suited for different length and time scales have been developed.

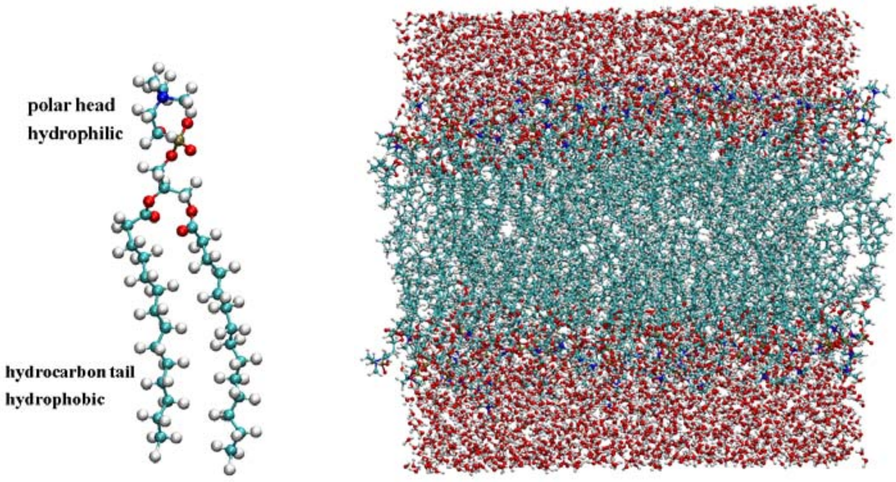

(a) (b)

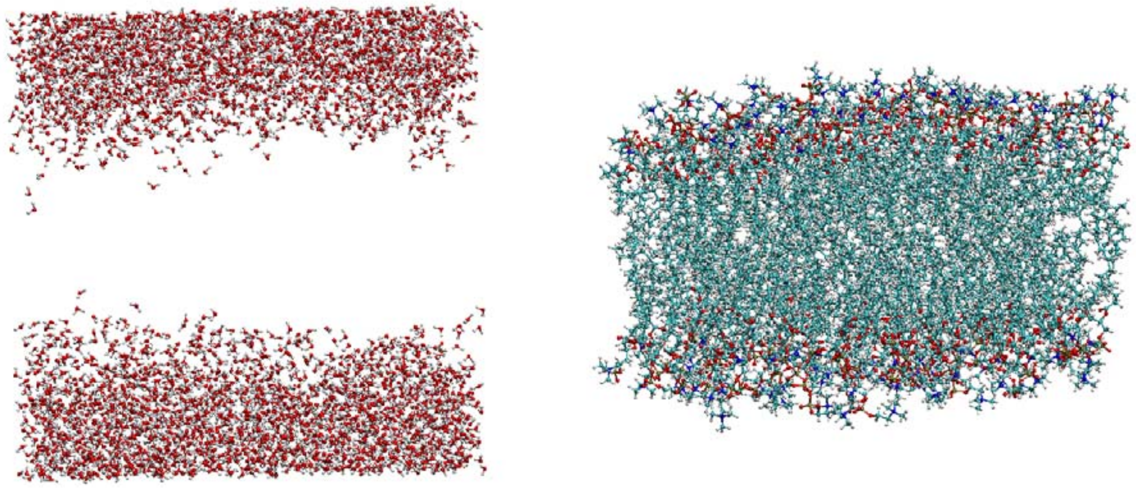

(c)

Figure 2.1. Schematic of a lipid bilayer membrane in an atomistic view. The carbon atoms are blue. The oxygen atoms are red. (a) A single lipid with a polar head group and two apolar hydrocarbon tails. (b) Lipid molecules in a water solution, hydrophobic tails are hiding from water molecules, polar head regions contact with water molecules. (c) Lipid molecules are horizontally shifted to see the hydration region of the lipid bilayer.

Membrane simulation models can be classified into three main groups in the following review: atomistic force-fields, coarse-grained models, numerical implementations based on continuum models. Each main group will be further categorized into subgroups, for example, coarse-grained models will be divided into explicit-solvent and solvent-free models. It should be noted that many very informative review articles have been written on the subject of membrane simulations [6, 7, 25-30]. Because the model we developed in the present work is intimately related to the solvent-free coarse-grained models and the continuum theories, these two classes of simulations are emphasized in the following review. For detail description of other types of models and applications, the reader is referred to the abovementioned review articles and the references therein. Note that the boundaries between the atomistic, mesoscopic, and continuum scales are by no means a matter of black and white, and different length scales are hierarchically related. Some models were intended to be in a coupled multiscale methodology [31].

2.1 Atomistic simulations

Statistical mechanics provides a powerful theoretical framework to study the relation between the macroscopic and microscopic worlds. Molecular simulations, such as molecular dynamics simulations and Monte Carlo simulations, are powerful computational tools as part of the statistical mechanics. Molecular simulations have been utilized in a variety of scientific and engineering fields, such as nanotechnology [32, 33], and material science [34, 35], to explore the small scale phenomena.

In the atomic scale, the best explanation is to observe. However, due to the fluidity (molecular diffusion) of the membrane in biologically relevant states, direct observation of dynamics of small molecules or lipids in experiments is troublesome. Atomistic molecular dynamics (MD) simulations can be used to track motions of single molecule and thus obtain more detail than can be obtained experimentally. For example, the Butler group has studied the dynamics and interactions of a dye molecule with membrane lipids and water [36].

Atomistic simulations of biomembranes can be performed using all-atom force-fields or united-atom force fields. In all-atom force-fields, the degrees of freedom of every atom in a lipid is taken into account explicitly, while in united-atom force fields, each aliphatic carbon and associated hydrogen atoms are treated as one particle. In molecular dynamics simulations, the system is treated classically, therefore the chemical reactions are generally not considered. The interactions between atoms are divided into bonding interactions (which are functions of bond length, bond angle, and dihedral angle), and non-bonding interaction (such as electrostatic force and van der Waals force). The interaction parameters are usually determined through experiments or quantum mechanics (first principles calculations). The time evolution of the system is obtained by numerically integrating the Newton’s equations of motion. Applying concepts from statistical mechanics, the dynamic and thermodynamic properties can be evaluated from the simulated phase trajectory. Extensive reviews on atomistic simulations of biomembranes can be found in [6, 26].

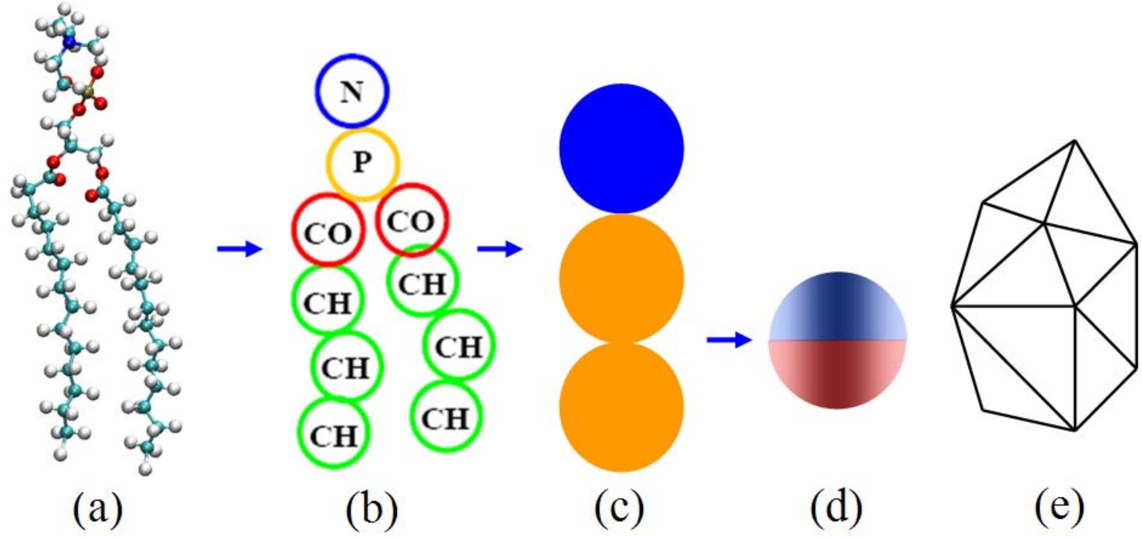

Figure 2.2. Membrane simulation models. (a) all-atom model of the DMPC lipid molecules; (b) a 10-particle coarse-grained model; (c) a 3-particle coarse-grained model. (d) one-particle-thick membrane models; (e) numerical methods based on continuum models (mesh elements)

2.2 Mesoscopic membrane models

Even with current massive parallel computational power, the length and time scales accessible to atomistic simulations are limited to a few tens of nanometers and microsecond [6]. On the other hand, experimental techniques are still being developed to observe membrane domains smaller than the resolution limit (~250 nm) for conventional optical microscopy. There are many biological problems occur in the intermediate length scale from a few tens of nanometers to a few hundreds nanometers, in which both the molecular details and the behavior of the whole membrane patch are concerned. Such problems include, for example, lipid raft formation [37, 38], membrane fusion and fission [39, 40], the effect of molecular scale detail on membrane elastic properties and phases [6, 16]. To bridge the gap between the atomistic simulations and experimental techniques, coarse-grained membrane simulation models were intensively used.

Coarse-grained membrane models are developed in order to extend the length and time scale of atomistic simulations through grouping several atoms into one bead and neglecting certain details of the molecular structure and interactions, assuming a priori the essential aspects of interest are known. Because coarse-grained simulations involve much less degrees of freedom and can adopt larger time step in time integration, both the accessible length and time scale can be increased orders of magnitude. Of course, the trade-off is that the coarser the membrane models, the more atomistic information are lost.

2.2.1 explicit-solvent coarse-grained models

Depending on whether the solvent (i.e., water) is explicitly modeled, coarse-grained models can be further divided into explicit-solvent and solvent-free models. Explicit-solvent models can be divided into generic and specific models based on the way the interaction parameters are obtained. For specific membrane models, the effective interactions between coarse-grained particles of lipid molecules are determined based on a comparison to the atomistic simulations or experimental data [27, 41, 42]. Several such models have been developed and successfully applied to many interesting membrane phenomena that are inaccessible to atomistic simulations [16, 38]. For generic models, the interactions between beads (the coarse-grained particles in a molecule) are designed in a rather empirical and abstract manner, and usually only the amphiphilic feature and rod-like shape of lipid molecules are inherited from realistic lipids in such models [43, 44].

Recently, dissipative particle dynamics (DPD) has been applied to membrane simulations using generic explicit-solvent models [45-48]. Dissipative particle dynamics, in which a cluster of molecules are represented by one DPD particle, was first developed to extend the time and length scales of molecular dynamics simulations of fluid dynamics, and later become a theoretically well-supported method to perform mesoscopic simulations for complex fluids [49-51]. It was shown that in DPD simulations, the hydrodynamics effect of bulk fluid was incorporated correctly due to the local conservation of linear momentum.

2.2.2 solvent-free coarse-grained models

In explicit-solvent membrane simulations, the degrees of freedom of water represent a substantial fraction of the simulated system. Water becomes even more significant when simulating a non-planar membrane such as vesicles, where membrane particles spread on a 2D surface, whereas solvent particles occupy the bulk. The solvent degrees of freedom thus vastly outnumber the lipid particles even for a modest sized membrane, limiting the accessible length and time scales of explicit-solvent coarse-grained models. In the case where the presence of water is merely to mediate hydrophobic interactions that drive the self-assemble of lipids, solvent-free coarse-grained models can be used to significantly increase the simulation efficiency and thus to further extend the length and time scale compared to explicit-solvent coarse-grained models. For this reason, significant efforts have been devoted in developing solvent-free coarse-grained models in recent years [52-57].

For a class of solvent-free models, effective intermolecular attractive interactions are added to substitute for the hydrophobic interactions that are missing due to neglecting of water. Therefore in such models, lipids can self-assemble into membranes in absence of water. Devising effective attractive interactions between lipids is validated by whether some critical features of lipid bilayer membrane can be reproduced, such as membrane self-assembly, in-plane fluid phase, biologically relevant bending rigidity. Reproducing these features constitutes the major challenge in the development of solvent-free membrane models. In the models of modest level of coarse-graining, each amphiphilic molecule is coarse-grained into a chain of multiple connected beads [52-57]. These models differ from each other in certain aspects such as tail length, flexible or rigid chain, with multi-body potential or not, etc. A more detailed review can be found in [7]. There are other solvent-free models that do not have effective attractive interactions to substitute for the hydrophobic effect. Instead, specific methods varying in different models are used to stabilize bilayer structure, such as forcing head groups on a reference plane [58], or using “phantom” solvent [59].

Reduced unites are typically used for solvent-free coarse-grained models, and lipid length and diffusion constant are in practice used to map the reduced units back to real physical quantities. However, the speed-up process due to the coarse-graining may not be the same to all motions in system. Therefore, care must be taken when interpreting the time scale of simulations [6].

2.2.3 “Aggressive” solvent-free coarse-grained models

As estimated by Marrink et al. [6], a reasonable limit on molecular simulations at the moment is a million particles. Given that, the coarser the membrane model is, the larger the length scale can be accommodated. To further speed up simulations involving large membranes, “aggressive” solvent-free coarse-grained models have been developed, in which a single or a cluster of lipids are represented by a single particle. The resulting assembled membranes are only two- or one-particle-thick, which are much simplified membrane system. The particles in such models are different from traditional coarse-grained particles or beads in that they have orientational degrees of freedom that are represented by a particle-fixed unit vector. Anisotropic interactions, in the same spirit as the Gay-Berne liquid crystal potential [60, 61], are defined as functions of particle orientations, so that the alignment of particles into a planar membrane is energetically favored. The difference from the Gay-Berne liquid crystal potential is that only the 2D membrane configuration is favored, not a 3D liquid crystal. Attempts to develop such models are often frustrated by reproducing the bilayer properties such as membrane self-assembly, in-plane fluid phase, and biologically relevant bending rigidity. In the pioneering model of Drouffe et al. [62], particles are able to self-assemble into one-particle-thick fluid phase. However, membrane bending rigidity of this model is significantly lower than the experimental range. In addition, its use of multibody potential necessarily compromises the computational efficiency. Along this direction, several other models were proposed, aiming to avoid using multibody potentials or to reproduce experimentally relevant membrane properties [31, 63-65]. In a recent model of such type, Kohyama [65] extended the model of Drouffe et al. [62] to a pair potential, where the bending rigidity is controlled by a time-dependent variable. Despite varying degrees of success of these models, it remains unclear whether an anisotropic pair potential as simple as Lennard-Jones (LJ) in 3D exists to mimic the hydrophobic interactions while yielding biologically relevant membrane properties.

There are two approaches to establish a simulation model for fluid membranes at the large length scale. One is the numerical implementations of the continuum membrane models. The other is the highly coarse-grained inter-particle interaction-based membrane simulation models. One of the drawbacks of the former class of models is that extra or dedicated computational effort is needed to take into account the in-plane fluidity and topological changes. Conversely, the latter class of models can naturally capture the in-plane fluidity and viscosity, and simulate topological changes. On the other hand, the disadvantage of the inter-particle interaction-based models is that they suffer length scale limitations due to the small intrinsic particle size, which is not the case for the former class of models. The model developed in this thesis research belongs to the latter class of models. The top-down membrane simulation models will be reviewed in the following section.

2.3 Continuum scale modeling

On the length scales much larger than membrane thickness, bilayer membranes can be regarded as a 2D surface embedded in 3D space with its deformation behavior dictated by only a few effective mechanical properties such as bending rigidity, area compression modulus, and viscosity. Many examples of such case, such as vesicle shape transformations [3, 8, 10, 66], micropipette aspiration [67, 68], membrane tethering [69, 70], membrane undulation [71-73], have been intensively studied.

2.3.1 Theoretical modeling

Unraveling the mystery of the intriguing biconcave shape of normal red blood cells (RBC) motivated very early continuum mechanics modeling of biomembranes. It is important to point out that in RBC membranes, a protein network with fixed connectivity is attached to the lipid bilayer, which complicates the study of RBC composite membranes. The spectrin network is still stimulating some active research, such as what is the stress stress-free shape of the spectrin network [74], the spectrin network dynamic remodeling in membrane deformation [75], and coupling between the lipid bilayer and the spectrin network [72, 73]. In this thesis, we only focus on the lipid bilayer.

The well-established theory of thin elastic shells [76] have long been applied to engineering thin shells that are widely used in architectural structures, airplanes, ships, high-pressure containers, etc. An intuitive way seems to apply the theory of engineering shells to biomembranes. For example, in an early study [77], the RBC membrane was modeled as solid thin shells just as engineering shells and the sphering process of RBCs was investigated assuming the biconcave shape as the stress-free configuration. Lipid bilayers differ from engineering solid shells in many ways. First, the lipid molecules can undergo fast diffusion in the in-plane direction of bilayer membranes, giving rise to a fluid phase. For this reason, Lipid bilayers are essentially thin fluid shells. Second, lipid bilayers are only two-molecule thick and thus are highly molecular structure-based in the thickness direction. The in-plane fluidity makes bilayer membranes much more “soft” than an engineering thin shell with the same bending rigidity. For example, fluid bilayer can change from developable to undevelopable surface or vice visa without causing in-plane stretching and shearing. Due to the strong hydrophobic effect, lipids can stably form the two-molecule-thick but tens of micrometer large 2D membrane structure. An analog of such a nature-made thin fluid shell has not been seen in macroscopic world.

As early as in 1970, Canham [78] proposed that bilayer membranes are inextensible and shear-free in the lateral direction, and bending energy is the only elastic energy that determines the static equilibrium shapes of membranes. The bending energy expression in Canham's model was inspired by the bending deformation of engineering thin plate. Viewing lipid bilayers as liquid crystals, Helfrich proposed [79] the same conclusion and adopted a more general formula for describing the curvature energy. The so-called Canham-Helfrich curvature energy E_b takes the following form,

$$E_b = \frac{1}{2}\int \left(B\left(c_1 + c_2 - c_0\right)^2 + \bar{k}_c c_1 c_2 \right) \mathrm{d}A, \tag{1}$$

where B is the membrane bending rigidity, $\bar{k}_c$ is called Gaussian bending rigidty, c_1 and c_2 are the two principal curvatures of the membrane surface, and c_0 is the spontaneous curvature. In a typical theoretical treatment for a homogenous fluid vesicle, taking into account the area and volume constraints by the Lagrange multipliers, the free energy functional is written as,

$$E = E_b + \Sigma A + PV \tag{2}$$

where Σ is the Lagrange multiplier identified as the membrane tension, A is the membrane area, P is the Lagrange multiplier representing the osmotic pressure difference across the membrane, and V is the enclosed volume. Since the free energy function only depends on the current configuration of membranes, which is simpler than solid thin shells, it is possible to analytically derive the equilibrium equation of fluid membranes as the Euler-Lagrange equation of the membrane free energy functional. Subjected to the area and volume constraints, minimizing the bending energy in Eq. (1) or solving the shape equilibrium equation via semi-analytical methods produces thermodynamically stable fluid vesicle shapes that agree well with experiments [3, 80].

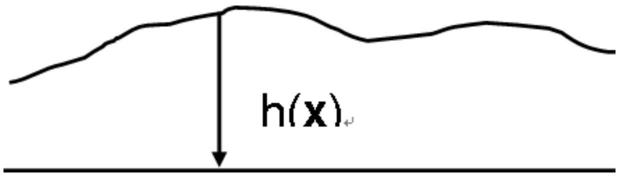

Figure 2.3. A Monge representation of a 2D membrane.

The seminal paper of Brochard and Lennon [81] first pointed out that the membrane undulations observed in optical microscopy were essentially the thermally excited membrane fluctuations subject to the Boltzmann distribution, and showed that the membrane bending rigidity could be derived from the mean square amplitude. These findings lead to a class of non-invasive experimental methods of measuring the bending rigidity of bilayer membranes [82-85]. The small fluctuation of a 2D membrane can be described by a Monge representation $h(\mathbf{x})$, where h is the height of membrane with respect to a reference plane, as shown in Figure 3, and $\mathbf{x}=(x,y)$ is a two-dimensional vector. In the Fourier space, the fluctuations with different wave vectors decouple. Via Fourier transform, we have,

$$h(\mathbf{x})=\frac{A}{4\pi^2}\int_{\Omega_\mathbf{q}}\exp(i\mathbf{q}\cdot\mathbf{x})h(\mathbf{q})d\mathbf{q}, \tag{3}$$

$$h(\mathbf{q})=\frac{1}{A}\int_{\Omega_\mathbf{x}}\exp(-i\mathbf{q}\cdot\mathbf{x})h(\mathbf{x})d\mathbf{x}, \tag{4}$$

where $\mathbf{q}=(q_x,q_y)=\left(\frac{2\pi}{\lambda_x},\frac{2\pi}{\lambda_y}\right)$, λ_x and λ_y are the wavelength along x and y directions, $A=L^2$ is the projected area of the membrane of length L.

In the low-tension regime, in which the tension is balanced by the entropy loss instead of area expansion resistance, the free energy of the fluid membrane is given as,

$$E(h(\mathbf{x}))=\frac{1}{2}B\int_{\Omega_\mathbf{x}}\left(\frac{\partial^2 h}{\partial x^2}+\frac{\partial^2 h}{\partial y^2}\right)^2 d\mathbf{x}+\Sigma\int_{\Omega_\mathbf{x}}\frac{1}{2}\left(\left(\frac{\partial h}{\partial x}\right)^2+\left(\frac{\partial h}{\partial y}\right)^2\right)d\mathbf{x}. \tag{5}$$

The first term in Equation (5) denotes the membrane bending energy which is a simplified form of the first term in Equation (1) under the small displacement assumption (assuming the spontaneous curvature C_0 is zero in this case). The second term accounts for the free energy associated with the membrane lateral tension. The free energy can be expressed in Fourier space [2],

$$E(h(\mathbf{q}))=\frac{1}{2}\frac{A^2}{4\pi^2}\int_{\Omega_\mathbf{q}}\left(\kappa_b q^4\right)h(\mathbf{q})h^*(\mathbf{q})d\mathbf{q}, \tag{6}$$

where * denotes the complex conjugate, $q=\sqrt{q_x^2+q_y^2}$. The equipartition theorem yields,

$$\left\langle \left|h(q)\right|^2 \right\rangle = \left\langle h(\mathbf{q})h^*(\mathbf{q}) \right\rangle = \frac{k_B T}{A\left(Bq^4+\Sigma q^2\right)}. \tag{7}$$

Mean square amplitude $\left\langle \left|h(q)\right|^2 \right\rangle$ in the Fourier space can be measured from optical microscopy or obtained from numerical simulations, and then can be fitted to Equation (7) to estimate the bending rigidity B. The mean square amplitude in terms of $h(\mathbf{x})$ in the bending-dominant wavelength range is given as [86],

$$\left\langle h^2(\mathbf{x}) \right\rangle \cong \frac{Ak_BT}{4\pi^3 B} \tag{8}$$

An estimation of the root of the mean square fluctuation can be made by choosing the following values: A = 20 μm^2, B = 20 k_BT, which yields $\sqrt{\left\langle h^2(\mathbf{x}) \right\rangle}$ ~90 nm which is observable by optical microscopy. It is interesting to point out that membrane fluctuation results in an entropic repulsive force between the membrane and a substrate which is used by cells as the main means to avoid the non-specific adhesions [87]. Membrane-substrate interactions are of paramount importance in cell related experiments [88].

It is worth noting that Equation (7) is only valid in the low-tension (entropic tension) regime. In the high-tension (area stretching tension) regime in which the contour area of the membrane is expanded, the out-of-plane fluctuations are largely suppressed and not visible to the optical microscopy. The stretching energy can be simply described by a quadratic form

$$E_s = \frac{1}{2}K_A \int_\Omega \varepsilon_A^2 \mathrm{d}A, \tag{9}$$

where K_A is the area compression modulus, ε_A is the contour area strain. Because K_A sets a much higher energy scale than the bending rigidity, bilayer membranes are usually considered as inextensible in continuum theories [3, 78] (see Eq. (2)). An equation describing the relationship between the relative projected area change and the membrane lateral tension was given by Helfrich [86],

$$\frac{\Delta A}{A}=\left(\frac{k_B T}{8\pi B}\right)\ln\left(1+\frac{\Sigma A}{\pi^2 B}\right)+\frac{\Sigma}{K_A}\,. \tag{10}$$

Equation (10) was applied in micropipette aspiration experiments to measure the bending rigidity B and the area compression modulus K_A [89].

In the abovementioned continuum modeling, viscous effects of fluid membrane itself and the bulk surrounding fluid are neglected, and only a static picture is adopted. Hydrodynamic continuum models of fluid membranes with or without the surrounding bulk fluid have been developed recently [90, 91]. In particular, Arroyo and DeSimone showed the importance of the viscosity on the dynamic relaxation of the membranes in their recent work [90]. In general, such hydrodynamic continuum modeling is mathematically much involved because the differential geometry must be used to describe the non-Euclidian surface in 3D space.

2.3.2 Numerical implementations

Analytically or semi-analytically solving continuum equations for membranes in either static or dynamic states is only possible for simple cases such as axisymmetric [92]. For complicated or arbitrary membrane shapes encountered in biologically relevant phenomena, one needs to resort to space discretization numerical methods. Here, the space discretization numerical method means that either the continuum free energy functional or its weak form is discretized in space via mesh elements [93, 94] or meshless particles [95].

Triangulated membrane models [66, 93, 96, 97] have been intensively used in simulating biological membranes [10] and protein networks [75, 98, 99]. For triangulated membrane models, the bending energy is calculated through the angles between adjacent triangles. The fixed connectivity of the triangular network gives rise to a solid membrane. In order to simulate fluid vesicles, a bond-flipping algorithm using Monte Carlo method is introduced in the dynamically-triangulated membrane models. The membrane area and volume are easy to calculate due to the known connectivity. Feng and Klug [94] developed a finite element framework for fluid membranes using subdivision thin shell finite elements. As they pointed out, much computational efforts are involved to deal with spurious zero-energy deformation modes induced by the in-plane zero shear resistance. In general, for numerical methods based on mesh elements, dedicated computational efforts or algorithms are needed to deal with fluid phase and topological changes of fluid membranes. Noguchi and Gompper [95] developed a meshless fluid membrane model, in which the membrane curvature is fitted via moving least-square methods. In addition, the phase field approach, which is a mathematical model for solving interfacial problems (see a review by Chen [100]), was applied to fluid vesicles in different conditions [101, 102]. For example, Du et al. applied the phase field approach to study the deformation of vesicle membranes under elastic bending energy in three dimensions [103, 104] and the vesicle-substrate adhesion [105].

Chapter 3

The coarse-grained membrane model

In the large scale, the membrane is mechanically regarded as a thin fluid shell, and thus the mechanical effective properties such as membrane bending rigidity and in-plane viscosity are believed to play a dominate role in determining membrane morphologies or vesicle shapes in various biological conditions, such as fluid vesicles in shear flow [66], membrane deformation in stem cell polarization. The main goal of this thesis research is to develop an efficient fluid membrane model to study the mechanics of the fluid membrane at large length scale.

The membrane model we developed here is an “aggressive” solvent-free coarse-grained model. Particle-based model can simulate fluidity as well as hydrodynamics naturally. The one-particle-thick feature of the model pushes the length scale of bottom-up coarse-grained models to the limit. Many unique features of the model that will be pointed out later make this model a powerful tool to study membrane mechanics and physics at large length scale.

3.1 The anisotropic inter-particle pair potential

The coarse-grained particles in our model are axisymmetric, with their axes of symmetry representing the longitudinal direction of lipid molecules. The model features a soft-core pair-wise inter-particle potential with the interaction strength weighed by the relative orientations of the particle pair. Correspondingly, the inter-particle potential is constituted of two functions, $u(r)$ and $\phi\left(\hat{\mathbf{r}}_{ij}, \mathbf{n}_i, \mathbf{n}_j\right)$, which respectively describe the distance and orientation dependences. Figure 1 depicts a generic relative position and orientation of such a particle pair, where the two halves of each particle are colored distinctly to indicate its orientation. We denote $\mathbf{r}_i$ and $\mathbf{r}_j$ the center position vectors of particles i and j, respectively. The inter-particle distance vector is then $\mathbf{r}_{ij} = \mathbf{r}_i - \mathbf{r}_j$. We also denote $r = |\mathbf{r}_{ij}|$ and $\hat{\mathbf{r}}_{ij} = \mathbf{r}_{ij} / r$. The unit vectors $\mathbf{n}_i$ and $\mathbf{n}_j$ represent the axes of symmetry of particles i and j, respectively. For simplicity, the rotational degree of freedom about the axis of symmetry of each particle is neglected. Therefore, each particle carries five degrees of freedom, i.e., three translational and two rotational degrees of freedom (noting the constraint $\mathbf{n} \cdot \mathbf{n} = 1$).

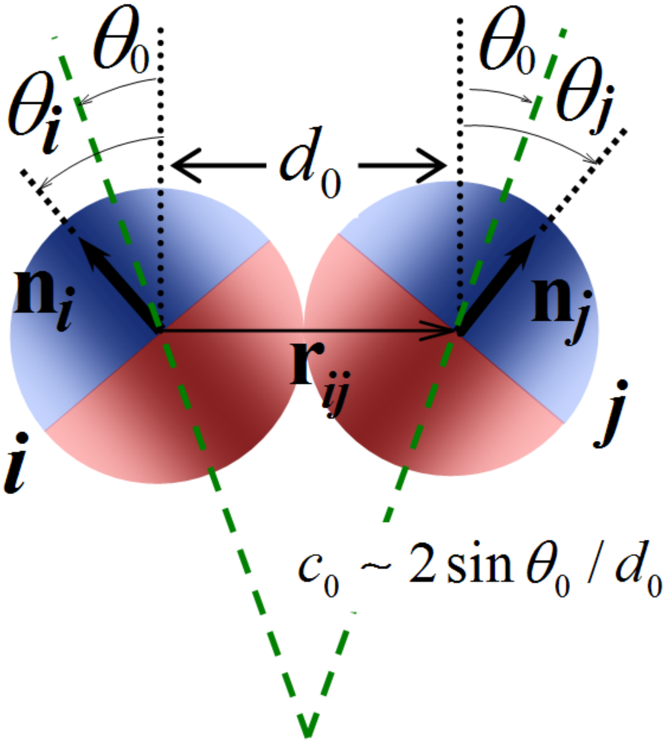

Figure 3.1. Schematics of inter-particle interactions. Kinetically, each particle is axisymmetric with a particle-fixed unit vector $\mathbf{n}$ representing the axis of symmetry and a mass of m. The inter-particle interaction is both distance- and orientation-dependent. The angle θ_0 is a model parameter charactering the spontaneous curvature. The configuration at $\theta_i = \theta_j = \theta_0$ corresponds to the energetically most favorable relative orientation between two particles. The two halves of each particle are colored distinctly to indicate the orientation of the particle.

In searching for the functional form of the distance-dependent function $u(r)$, we found that the classical 12-6 LJ potential only leads to solid membranes at low temperatures and gas phase at high temperatures. Missing of a fluid phase in between is due to the steep energy landscape of the 12-6 LJ potential: the inter-particle interaction forces are either too strong (near the equilibrium distance) to permit particle diffusion or too weak (once escaped from the equilibrium distance) to hold particles together. In order to be able to tune the restoring force, we adopt the following two-branch function $u(r)$:

$$u(r)=\begin{cases} u_R(r)=\varepsilon\left[\left(\frac{r_{\min}}{r}\right)^{2\eta}-2\left(\frac{r_{\min}}{r}\right)^{\eta}\right] , & r<r_{\min} \\ u_A(r)=-\varepsilon\cos^{2\zeta}\left(\frac{\pi}{2}\frac{(r-r_{\min})}{(r_c-r_{\min})}\right) , & r_{\min}<r<r_c \end{cases} , \qquad (11)$$

where ε and σ are the energy and length units, respectively. The repulsive branch $u_R(r)$ adopts the LJ type potential with the exponent η as an empirical parameter that can tune the restoring force at the equilibrium distance. The attractive branch $u_A(r)$ is of a cosine function that smoothly decays to zero at the cutoff radius r_c. The exponent ζ tunes the slope of the attractive branch (see Figure 2(a)) and hence the diffusivity of the particles. The two branches smoothly meet at $r=r_{\min}$ with C^1 continuity. We set the distance at the minimum of the potential $r_{\min}=\sqrt[6]{2}\sigma$, the same as that in the 12-6 LJ potential, and $r_c=2.6\sigma$ to include second-neighbor interactions.

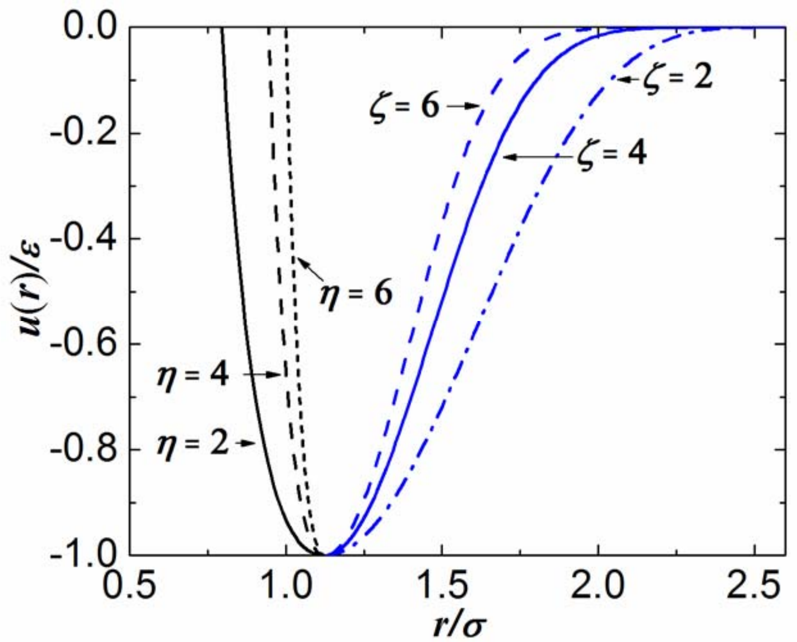

Figure 3.2. The distance-dependent function $u(r)$ consisting of a repulsive branch and an attractive branch. The slope of each branch can be tuned by changing the empirical exponents η (repulsive branch) and ζ (attractive branch). Both η and ζ affect particle diffusivity. The solid curves correspond to $\eta = 2$ and $\zeta = 4$, which are the representative values used in the most simulations later.

Following the treatment in anisotropic potentials for liquid crystal or colloids [60, 106], we use ϕ to weigh the interaction strength for different relative orientations, leading to the final form of the anisotropic pair potential:

$$U\left(\mathbf{r}_{ij}, \mathbf{n}_i, \mathbf{n}_j\right) = \begin{cases} u_R(r) + \left[1 - \phi\left(\hat{\mathbf{r}}_{ij}, \mathbf{n}_i, \mathbf{n}_j\right)\right]\varepsilon & , r < r_{\min} \\ u_A(r)\,\phi\left(\hat{\mathbf{r}}_{ij}, \mathbf{n}_i, \mathbf{n}_j\right) & , r_{\min} < r < r_c \end{cases}. \tag{12}$$

The orientation-dependent function scales the attractive branch of the distance-dependent potential, while shifts upward the repulsive branch (shown in Figure 2(b)). The separate operations ensure a fixed distance of minimum energy for different relative orientations between two particles. The orientation-dependent function substitutes for the hydrophobic effects and takes the following form:

$$\phi = 1 + \mu\left[a\left(\hat{\mathbf{r}}_{ij}, \mathbf{n}_i, \mathbf{n}_j\right) - 1\right], \tag{13}$$

where

$$a = \left(\mathbf{n}_i \times \hat{\mathbf{r}}_{ij}\right) \cdot \left(\mathbf{n}_j \times \hat{\mathbf{r}}_{ij}\right) + \sin\theta_0 \left(\mathbf{n}_j - \mathbf{n}_i\right) \cdot \hat{\mathbf{r}}_{ij} - \sin^2\theta_0 . \quad (14)$$

The function a (hence ϕ) reaches its maximum of 1 when $\theta_i = \theta_j = \theta_0$ (see Figure 1 for θ_i, θ_j, and θ_0), and is less than 1 otherwise. Hence, the relative orientation $\theta_i = \theta_j = \theta_0$ is most energetically favored. Since θ_0 specifies the favorable inter-particle orientations, it directly links to the spontaneous curvature of the model membrane. The parameter μ weighs the energy penalty when the particles are disoriented from θ_0, and is thus related to the bending rigidity of the model membrane.

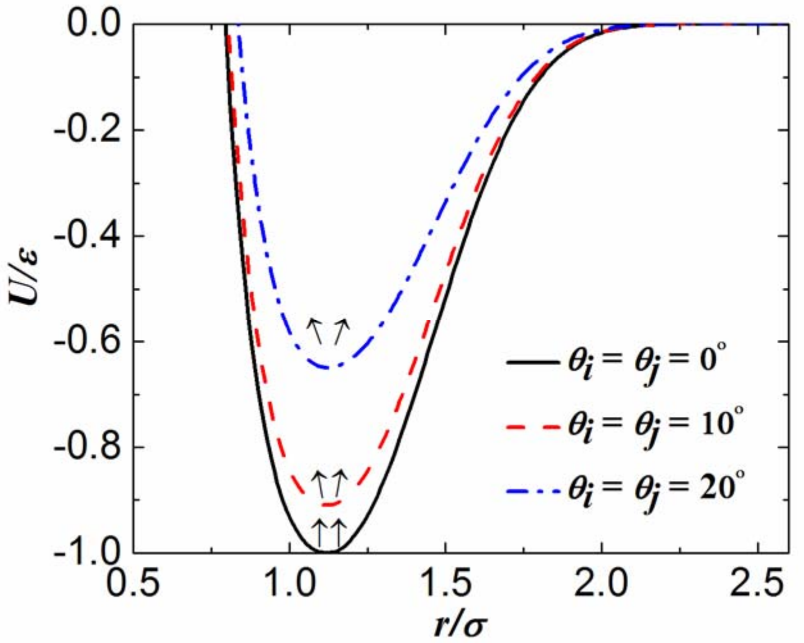

Figure 3.3. The orientation-dependent inter-particle pair potential U as a function of r for three different θ_i ($\theta_j = \theta_i$) with η=2, ζ=4, μ=3, θ_0=0. The double arrows denote the orientations of a particle pair.

The functional dependence of a on its three vector variables, i.e., $\hat{\mathbf{r}}_{ij}$, $\mathbf{n}_i$, $\mathbf{n}_j$, becomes clearer when all the vectors are confined in a 2D plane (see Figure 3.1). In this simplified case, function a is reduced to

$$a = \cos\theta_i \cos\theta_j + \sin\theta_0 \left(\sin\theta_i + \sin\theta_j\right) - \sin^2\theta_0 , \quad (15)$$

where the definitions of θ_i, θ_j, and θ_0 can be found in Figure 3.1. Assuming $\theta_i = \theta_j$ in Eq. (15), a can be further simplified to $a = 1 - \left(\sin\theta_i - \sin\theta_0\right)^2$, which implies that a maximizes when $\theta = \theta_0$. The spontaneous curvature c_0 is related to θ_0 via $c_0 = 2\sin\theta_0 / d_0$, where d_0 is the average inter-particle distance, as illustrated in Figure 3.1. To see the functional dependence of a on θ_i and θ_j, we consider the specific case of $\theta_0 = 0^{\mathrm{o}}$ at which $a = \cos\theta_i \cos\theta_j$. It follows that a reaches its maximum of unity when $\mathbf{n}_i$ is parallel to $\mathbf{n}_j$ ($\theta_i = \theta_j = 0^{\mathrm{o}}$) and perpendicular to vector $\hat{\mathbf{r}}_{ij}$. The functional dependence is plotted in Figure 3.4. The dependence of the potential U on the inter-particle distance at specified relative particle orientations is depicted in Figure 3.3. The relative particle orientation sets the depth of the energy well of the potential, but does not affect the inter-particle distance of the minimum energy.

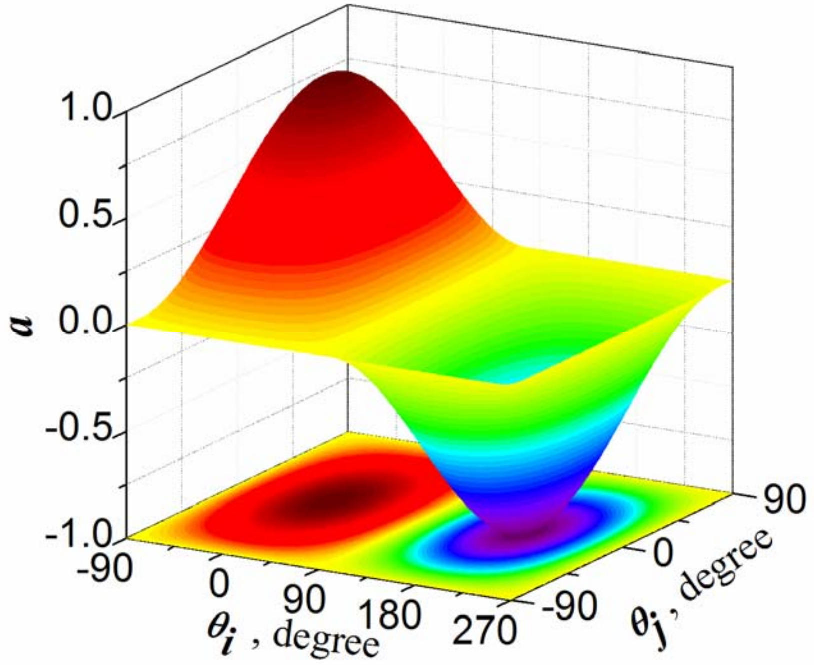

Figure 3.4. The functional dependence of a on θ_i and θ_j at $\theta_0 = 0$ shows the energetically favored and disfavored relative orientations of particles i and j. Both the 3D and 2D energy contours are plotted in the figure. A larger a corresponds to a lower interaction energy.

3.2 Molecular dynamics simulation algorithms

3.2.1 Equations of motion

Corresponding to the two sets of degrees of freedom, particle center positions and orientations, there are two sets of the equations of motion for the coarse-grained model. The first set governs the time evolution of the particle center positions,

$$m_i \ \ddot{\mathbf{r}}_i = -\frac{\partial U_i}{\partial \mathbf{r}_i}, \tag{16}$$

where m_i is the mass of particle i, $U_i = \sum_j U\left(\mathbf{r}_{ij}, \mathbf{n}_i, \mathbf{n}_j\right)$, and j runs over all the neighbors of i. The second set of equations governs the time evolution of the particle orientation, which can be derived from Euler's rigid body dynamics equations (see Appendix A1). However, considering that there are only five degrees of freedom, the equations of motion governing particle orientations can be derived in a more efficient manner. We treat $\mathbf{n}_i$ of particle i as three generalized coordinates with a geometric constraint $\mathbf{n}_i \cdot \mathbf{n}_i = 1$, the governing equations for $\mathbf{n}_i$ can be derived using the Lagrange equations with constraint forces as follows.

Since $\mathbf{n}_i$ is a body-fixed vector, the rate of change of $\mathbf{n}_i$ is $\dot{\mathbf{n}}_i = \boldsymbol{\omega} \times \mathbf{n}_i$, where $\boldsymbol{\omega}$ is the instantaneous angular velocity. Since rotating around $\mathbf{n}_i$ is neglected, the angular velocity $\boldsymbol{\omega}$ is then perpendicular to $\mathbf{n}_i$. Thus, one can obtain $\omega = |\boldsymbol{\omega}| = |\dot{\mathbf{n}}_i|$ from equations $\dot{\mathbf{n}}_i = \boldsymbol{\omega} \times \mathbf{n}_i$ and $|\mathbf{n}_i| = 1$. Therefore, for a rigid particle, the rotational kinetic energy for particle i is,

$$T_i^{rot} = \frac{1}{2} I \omega^2 = \frac{1}{2} I \left(\dot{\mathbf{n}}_i \cdot \dot{\mathbf{n}}_i\right),$$

where the moment of inertia I assumes to be $1 \cdot m\sigma^2$. The numerical coefficient of $m\sigma^2$ is not strict, values close to unity are all acceptable for the time integration in molecular dynamics simulations.

The constraint equations for $\mathbf{n}_i$ can be written as,

$$f_i\left(\mathbf{n}_i\right) = \mathbf{n}_i \cdot \mathbf{n}_i - 1 = 0,\ i = 1,2,\dots,N\,. \tag{17}$$

The Jacobian constraint coefficients are $\mathbf{g}_i = \frac{1}{2}\frac{\partial f_i}{\partial \mathbf{n}_i} = \mathbf{n}_i$ [107]. Thus, the Lagrange equations with the Lagrange multiplier for the three orientation degrees of freedom of particle i are,

$$\frac{d}{dt}\left(\frac{\partial T_i^{rot}}{\partial \dot{\mathbf{n}}_i}\right) = -\frac{\partial V}{\partial \mathbf{n}_i} + \lambda_i \mathbf{g}_i\,, \tag{18}$$

where V is the total potential of the system consisting of N particles. Substituting T_i^{rot} and $\mathbf{g}_i$ into Equation (18) yields,

$$I\ \ddot{\mathbf{n}}_i = -\frac{\partial V}{\partial \mathbf{n}_i} + \lambda_i \mathbf{n}_i\,. \tag{19}$$

Taking the derivative of Equation (17) with respect to time twice yields,

$$\ddot{\mathbf{n}}_i \cdot \mathbf{n}_i + \dot{\mathbf{n}}_i \cdot \dot{\mathbf{n}}_i = 0 \tag{20}$$

The Lagrange multiplier λ_i can be deduced from Equation (19) and (20) as,

$$\lambda_i = \frac{\partial V}{\partial \mathbf{n}_i} \cdot \mathbf{n}_i - I\ \dot{\mathbf{n}}_i \cdot \dot{\mathbf{n}}_i \tag{21}$$

Substituting Equation (21) in the equation (19) yields the final time evolution equations for the orientation degrees of freedom $\mathbf{n}_i$,

$$I\ \ddot{\mathbf{n}}_i = -\frac{\partial V}{\partial \mathbf{n}_i} + \left(\frac{\partial V}{\partial \mathbf{n}_i} \cdot \mathbf{n}_i - I\ \dot{\mathbf{n}}_i \cdot \dot{\mathbf{n}}_i\right)\mathbf{n}_i\,. \tag{22}$$

3.2.2 Tension and temperature coupling algorithms

Our coarse-grained molecular dynamics (CGMD) simulations presented below for planar membranes are performed in the ΣNT ensemble, where Σ is the membrane tension. Simulations for vesicles are performed in the NVT ensemble. We adopt the Nose-Hoover thermostat [108, 109] to maintain the system at desired temperatures (see

Appendix A2 for implementation detail). Since our model is solvent-free, the rigid-body translational and rotational motions are removed at each time step in our simulations, which may otherwise cause significant numerical errors (see Appendix A4). For a planar membrane with periodic boundary conditions, the Berendsen pressure coupling algorithm [110] is modified to a 2D case to maintain a desired tension Σ_0 in the membrane by rescaling the particle coordinates and box size at each time step. The scaling factor χ is

$$\chi = 1 + \frac{\Delta t}{3\tau_p K_A}\left(\Sigma_0 - \Sigma(t)\right), \tag{23}$$

where τ_p is the relaxation time, K_A (~ 4 ε/σ^2) is membrane area expansion modulus, Δt is the time step.

Membrane tension Σ can be calculated by applying the virial formula to the one-particle-thick 2D fluid membrane structure embedded in 3D space,

$$\Sigma = -\frac{3Nk_{\mathrm{B}}T}{2A} - \frac{1}{2A}\sum_{i,j>i}^{N} \mathbf{r}_{ij} \cdot \mathbf{F}_{ij} , \tag{24}$$

where A is the membrane contour area, $\mathbf{F}_{ij}$ is the force exerted on particle i by j. The first term on the right-hand side of Eq. (24), denoted by Σ_t, is the kinetic contribution, while the second term, denoted by Σ_f, is the potential contribution. Two features of the model membrane validate Eq. (24) for calculating membrane tension. First, considering that a small membrane patch is locally flat and essentially a particle-based surface, the out-of-plane stresses are negligibly small. Equation (24) thus computes the in-plane normal stress (the membrane tension), rather than the normal stress for 3D liquids. Second, for a fluid membrane in equilibrium, membrane tension is constant everywhere [111]. One follows that the membrane tension calculated by Eq. (24) is valid not only for flat membranes but also curved membranes. A more detailed description on Eq. (24) is given in Appendix A3.

3.3 Model membrane properties

3.3.1 Self-assembling

We next demonstrate that our inter-particle potential captures well the hydrophobic interactions and can lead to robust self-assembly of particles into fluid membranes. Starting with a random distribution of 5882 particles enclosed in a cubic box with periodic boundary conditions, CGMD simulations were performed. The particle system is thermostated at a constant temperature of $k_{\mathrm{B}}T = 0.17\varepsilon$, with k_{B} the Boltzmann constant and T the temperature. Figure 3.5 depicts four simulation snapshots. At intermediate stages ($t = 2000\tau$, where $\tau = \sigma\sqrt{m/\varepsilon}$ is the time scale.), membrane flakes are formed. The membrane flakes then coalesce into large planar membranes ($t = 5000\tau$), and finally close to form vesicles due to the edge effect ($t = 12000\tau$). In our simulations, the soft-core interaction potential allows us to adopt a relatively large time step ($\Delta t = 0.02\tau$).

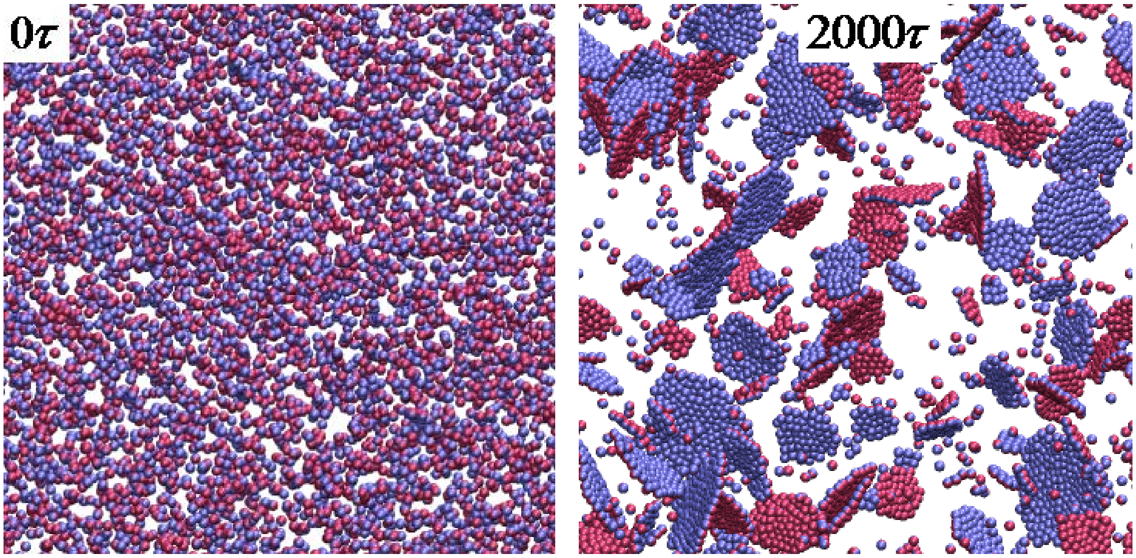

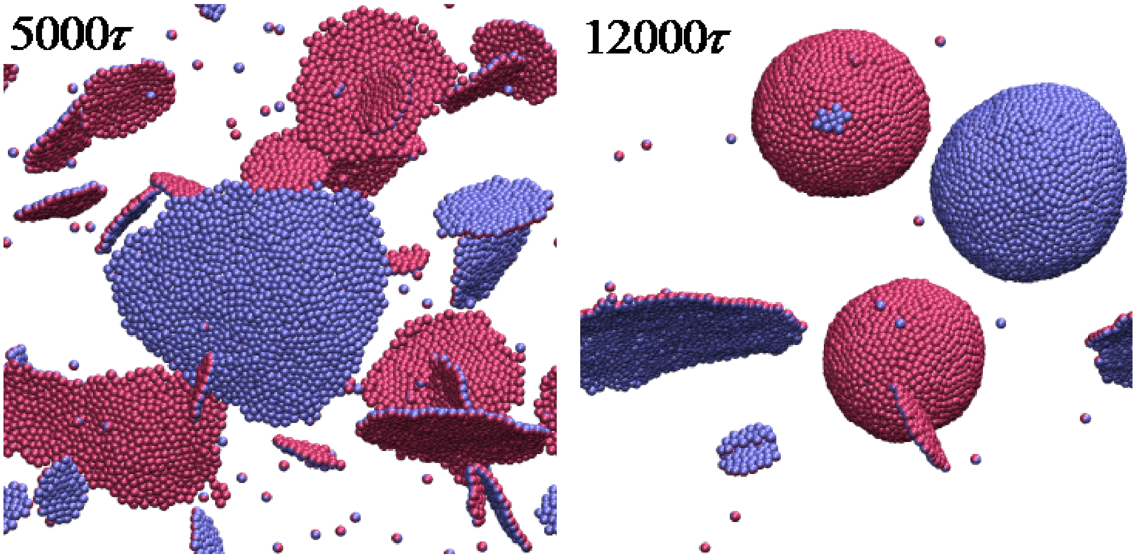

Figure 3.5. Snapshots from CGMD simulations demonstrating self-assembly of randomly distributed particles into vesicles. The parameters used in the simulations are ζ =4, μ =3, θ_0 =0, and k_BT = 0.17 ε . The two halves of each particle are colored distinctly to indicate its orientation, which facilitates visual observation of results.

3.3.2 Phase diagrams

We first characterize the diffusion constant as a function of the exponents η and ζ and temperature *T*. The preassembled square membrane adopted for this study consists of 5822 particles with side length ~70 σ . We maintain zero membrane tension in our simulations and set $\mu = 3$ and $\theta_0 = 0$. The in-plane diffusion constant $D = < s_i^2 > / 4t$ is systematically calculated at zero membrane tension, where s_i is the diffusion distance of particle *i* over time period *t*. The in-plane diffusion of particles is visually shown in Figure 3.6. A parametric study allows us to construct a phase diagrams of the diffusion constant on the (ζ, T) and (η, ζ) planes, as shown in Table 3.1 and 3.2. The particle membrane is considered in gel phase if D<0.01 σ^2 / τ , and in gas phase if at least one particle leaves the membrane during the simulations. The italic integer number in Table 3.1 and 3.2 denotes how many particles leave the membrane. We identified a broad fluid phase region in which the diffusion constant is on the order of 0.1 σ^2 / τ .

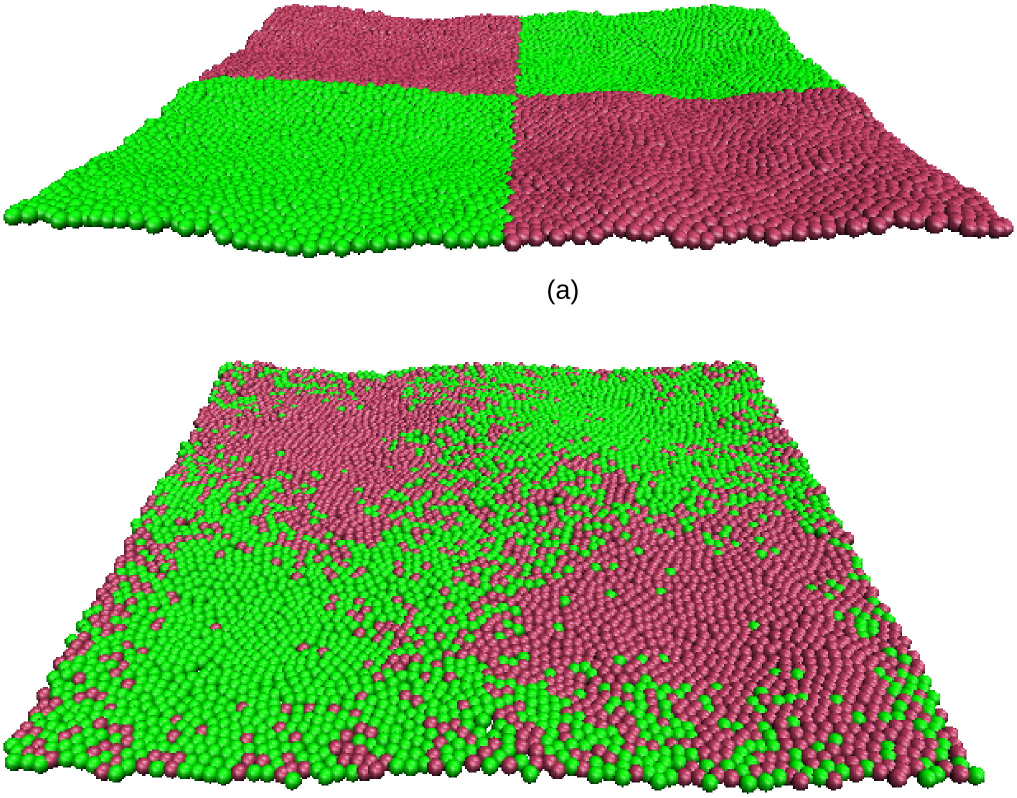

Figure 3.6. Particle diffusion in the lateral direction, (a) initial configuration, (b) configuration after a certain period of time.

Table 3.3 lists the average inter-particle distance d (first neighbor) for planar membranes in zero-tension state, which is calculated as follows. First, an equilibrium box size in the x-y plane is obtained by averaging box size over a long period of time. Then, the distance d is approximately obtained by assuming particles fill up the box (only in x-y) plane with hexagonal close-packed pattern. The average inter-particle distance d indicates

Table 3.1. The phase diagrams of the diffusion constant on the (T, ζ) plane. The abscissa represents temperature $k_B T$ in units of ε, the y-axis represents ζ. The value in the table elements denotes diffusion constant in units of σ^2 / τ.

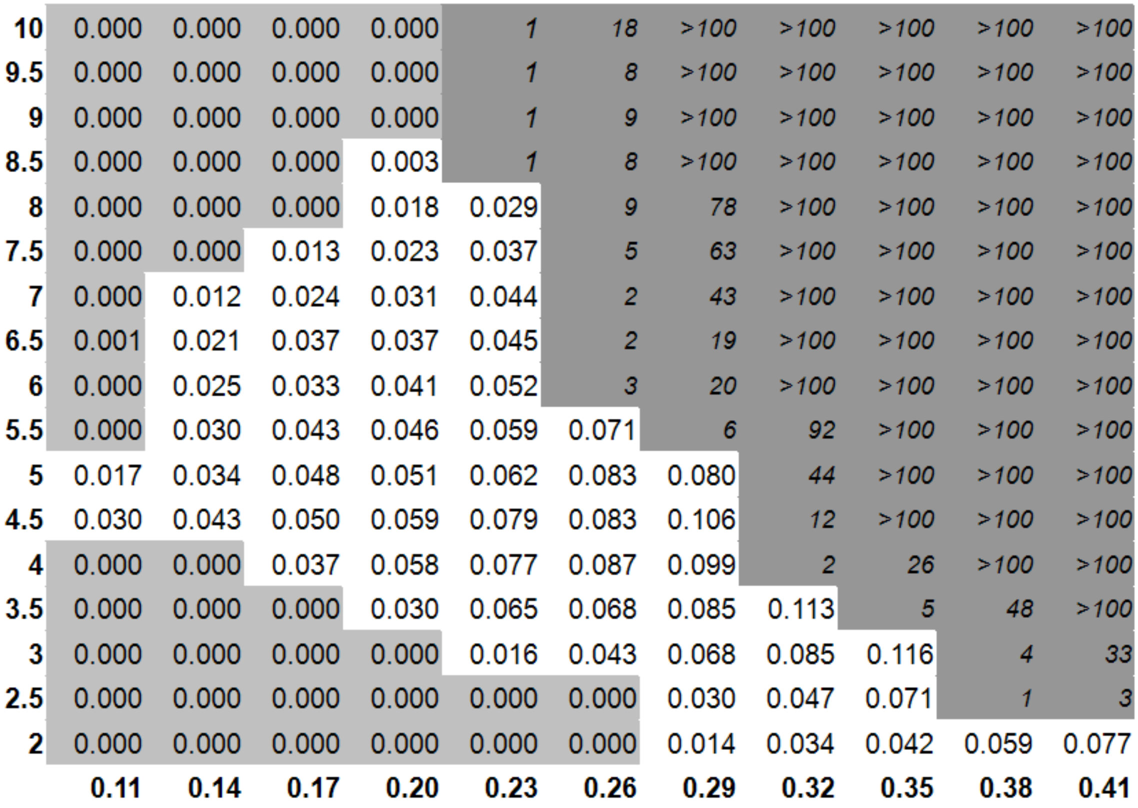

10	0.000	0.000	0.000	0.000	*1*	*18*	*>100*	*>100*	*>100*	*>100*	*>100*
9.5	0.000	0.000	0.000	0.000	*1*	*8*	*>100*	*>100*	*>100*	*>100*	*>100*
9	0.000	0.000	0.000	0.000	*1*	*9*	*>100*	*>100*	*>100*	*>100*	*>100*
8.5	0.000	0.000	0.000	0.003	*1*	*8*	*>100*	*>100*	*>100*	*>100*	*>100*
8	0.000	0.000	0.000	0.018	0.029	*9*	*78*	*>100*	*>100*	*>100*	*>100*
7.5	0.000	0.000	0.013	0.023	0.037	*5*	*63*	*>100*	*>100*	*>100*	*>100*
7	0.000	0.012	0.024	0.031	0.044	*2*	*43*	*>100*	*>100*	*>100*	*>100*
6.5	0.001	0.021	0.037	0.037	0.045	*2*	*19*	*>100*	*>100*	*>100*	*>100*
6	0.000	0.025	0.033	0.041	0.052	*3*	*20*	*>100*	*>100*	*>100*	*>100*
5.5	0.000	0.030	0.043	0.046	0.059	0.071	*6*	*92*	*>100*	*>100*	*>100*
5	0.017	0.034	0.048	0.051	0.062	0.083	0.080	*44*	*>100*	*>100*	*>100*
4.5	0.030	0.043	0.050	0.059	0.079	0.083	0.106	*12*	*>100*	*>100*	*>100*
4	0.000	0.000	0.037	0.058	0.077	0.087	0.099	*2*	*26*	*>100*	*>100*
3.5	0.000	0.000	0.000	0.030	0.065	0.068	0.085	0.113	*5*	*48*	*>100*
3	0.000	0.000	0.000	0.000	0.016	0.043	0.068	0.085	0.116	*4*	*33*
2.5	0.000	0.000	0.000	0.000	0.000	0.000	0.030	0.047	0.071	*1*	*3*
2	0.000	0.000	0.000	0.000	0.000	0.000	0.014	0.034	0.042	0.059	0.077
	0.11	**0.14**	**0.17**	**0.20**	**0.23**	**0.26**	**0.29**	**0.32**	**0.35**	**0.38**	**0.41**

Table 3.2. The phase diagrams of the diffusion constant on the (η,ζ) plane. The x-axis represents η, the y-axis represents ζ. The value in the table elements denotes diffusion constant in units of σ^2/τ.

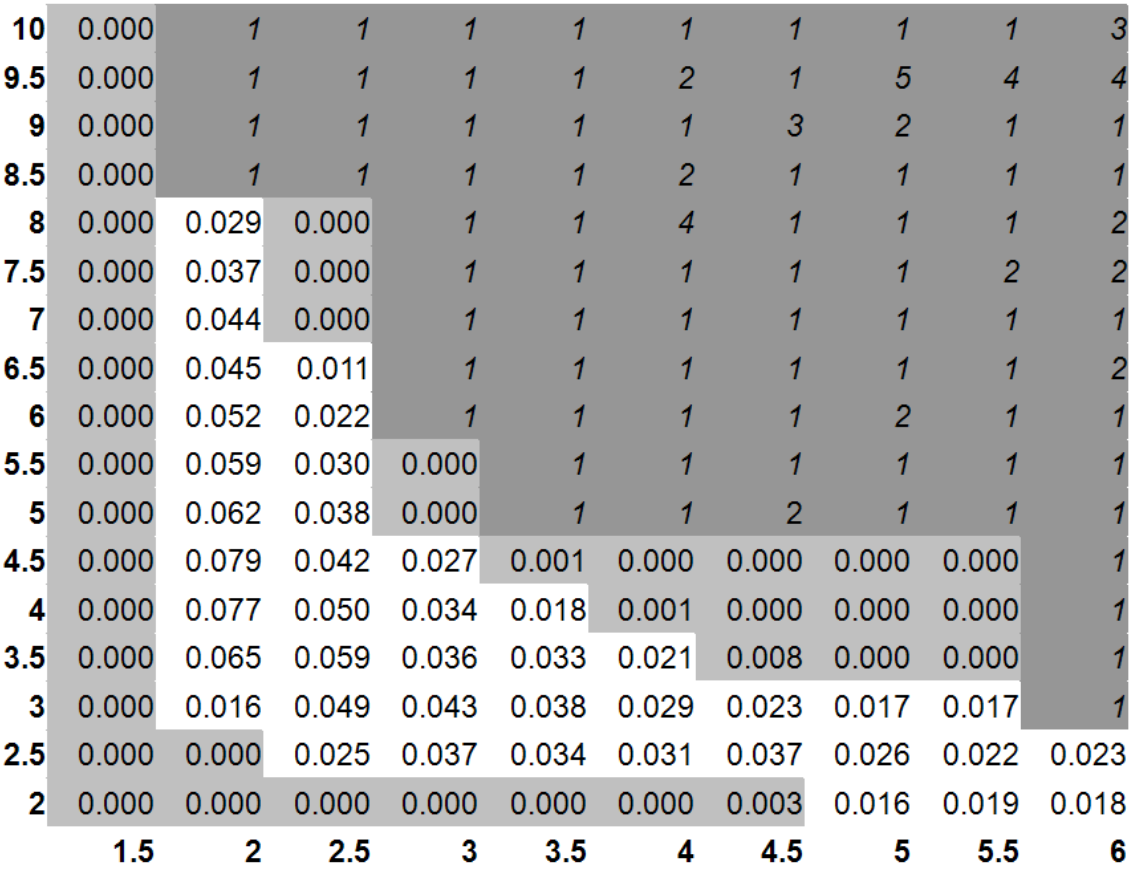

10	0.000	*1*	*1*	*1*	*1*	*1*	*1*	*1*	*1*	*3*
9.5	0.000	*1*	*1*	*1*	*1*	*2*	*1*	*5*	*4*	*4*
9	0.000	*1*	*1*	*1*	*1*	*1*	*3*	*2*	*1*	*1*
8.5	0.000	*1*	*1*	*1*	*1*	*2*	*1*	*1*	*1*	*1*
8	0.000	0.029	0.000	*1*	*1*	*4*	*1*	*1*	*1*	*2*
7.5	0.000	0.037	0.000	*1*	*1*	*1*	*1*	*1*	*2*	*2*
7	0.000	0.044	0.000	*1*	*1*	*1*	*1*	*1*	*1*	*1*
6.5	0.000	0.045	0.011	*1*	*1*	*1*	*1*	*1*	*1*	*2*
6	0.000	0.052	0.022	*1*	*1*	*1*	*1*	*2*	*1*	*1*
5.5	0.000	0.059	0.030	0.000	*1*	*1*	*1*	*1*	*1*	*1*
5	0.000	0.062	0.038	0.000	*1*	*1*	*2*	*1*	*1*	*1*
4.5	0.000	0.079	0.042	0.027	0.001	0.000	0.000	0.000	0.000	*1*
4	0.000	0.077	0.050	0.034	0.018	0.001	0.000	0.000	0.000	*1*
3.5	0.000	0.065	0.059	0.036	0.033	0.021	0.008	0.000	0.000	*1*
3	0.000	0.016	0.049	0.043	0.038	0.029	0.023	0.017	0.017	*1*
2.5	0.000	0.000	0.025	0.037	0.034	0.031	0.037	0.026	0.022	0.023
2	0.000	0.000	0.000	0.000	0.000	0.000	0.003	0.016	0.019	0.018
	1.5	**2**	**2.5**	**3**	**3.5**	**4**	**4.5**	**5**	**5.5**	**6**

Table 3.3. The inter-particle distance d on the (T, ζ) plane. The abscissa represents temperature $k_B T$ in units of ε, the y-axis represents ζ. The value in the table elements denotes d in units of σ.

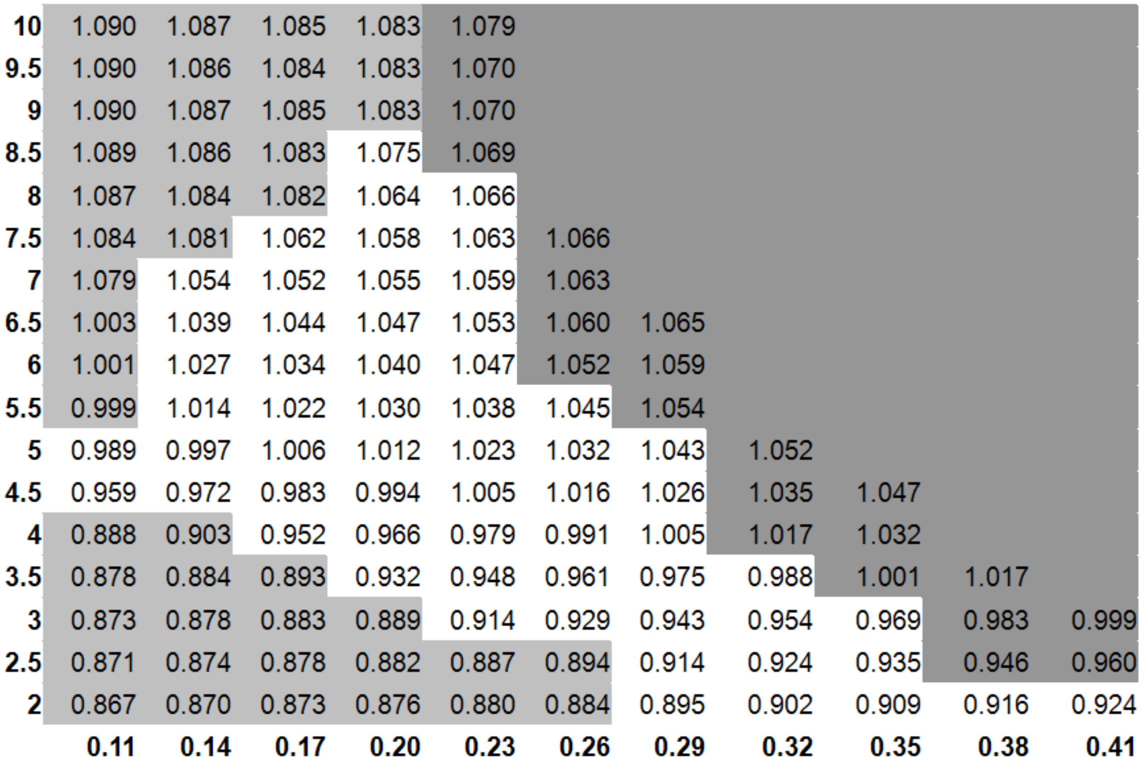

10	1.090	1.087	1.085	1.083	1.079						
9.5	1.090	1.086	1.084	1.083	1.070						
9	1.090	1.087	1.085	1.083	1.070						
8.5	1.089	1.086	1.083	1.075	1.069						
8	1.087	1.084	1.082	1.064	1.066						
7.5	1.084	1.081	1.062	1.058	1.063	1.066					
7	1.079	1.054	1.052	1.055	1.059	1.063					
6.5	1.003	1.039	1.044	1.047	1.053	1.060	1.065				
6	1.001	1.027	1.034	1.040	1.047	1.052	1.059				
5.5	0.999	1.014	1.022	1.030	1.038	1.045	1.054				
5	0.989	0.997	1.006	1.012	1.023	1.032	1.043	1.052			
4.5	0.959	0.972	0.983	0.994	1.005	1.016	1.026	1.035	1.047		
4	0.888	0.903	0.952	0.966	0.979	0.991	1.005	1.017	1.032		
3.5	0.878	0.884	0.893	0.932	0.948	0.961	0.975	0.988	1.001	1.017	
3	0.873	0.878	0.883	0.889	0.914	0.929	0.943	0.954	0.969	0.983	0.999
2.5	0.871	0.874	0.878	0.882	0.887	0.894	0.914	0.924	0.935	0.946	0.960
2	0.867	0.870	0.873	0.876	0.880	0.884	0.895	0.902	0.909	0.916	0.924
	0.11	**0.14**	**0.17**	**0.20**	**0.23**	**0.26**	**0.29**	**0.32**	**0.35**	**0.38**	**0.41**

Figure 3.7 gives a schematic phase diagram reproduced from Table 3.1. An interesting observation from the phase diagram is that the gel phase occurs at both small and large ζ. We attribute this phasic behavior to the variation of the equilibrium inter-particle distance d with ζ due to the second-nearest neighbor effects. Figure 3.8 (double y-axis) shows that d monotonically increases with ζ because of the effect of the second-nearest neighbor, and a maximum of D exists at $d = d_c \sim 1\,\sigma$. When $d < d_c$, the inter-particle interaction is dominated by the repulsive branch of the potential. In this regime, increasing ζ leads to a decrease in the repulsive force between particles, giving rise to a higher diffusivity. On the other hand, when $d > d_c$, the inter-particle interaction is dominated by the attractive branch of the potential. In this regime, increasing ζ leads to an increase in the attractive force, giving rise to a lower diffusivity.

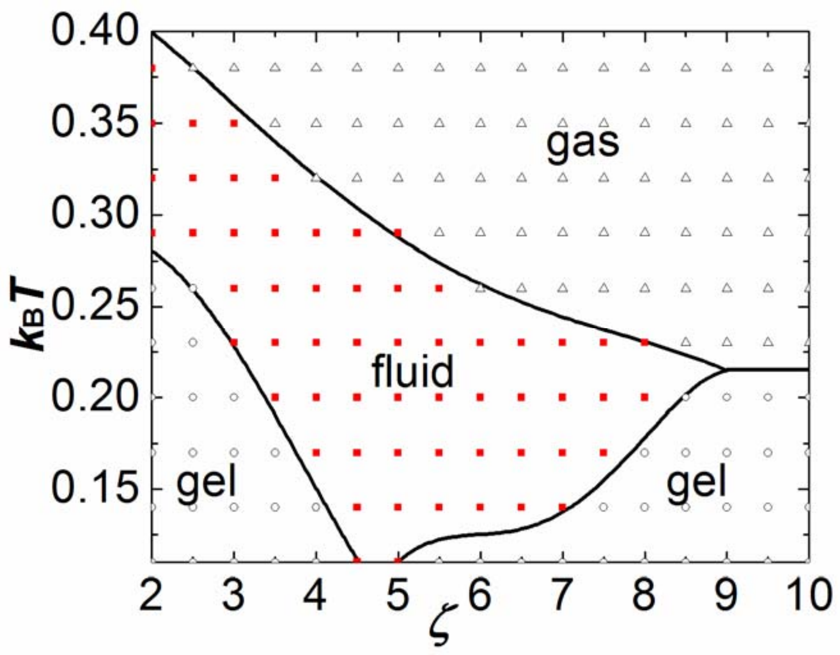

Figure 3.7. Phase diagram in the (ζ, T) plane at zero-tension. Three regions representing gel, fluid, and gas phases are identified, separated by solid lines. A broad fluid phase region with diffusion constant on the order of $0.1\,\sigma^2/\tau$ exists.

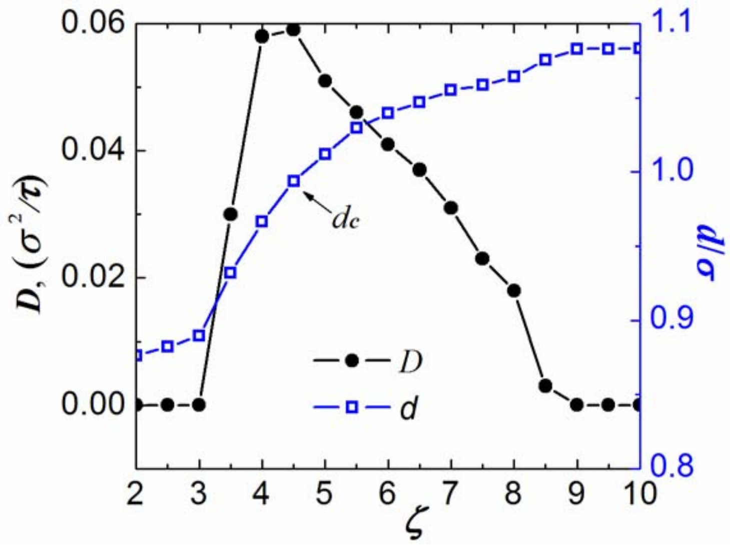

Figure 3.8. Diffusion constant D and inter-particle distance d as functions of the exponent ζ ($k_BT = 0.2\,\varepsilon$) for tensionless membranes.

The same trend of the diffusion constant applies to the other exponent η. As shown in Figure 3.9, d monotonically increases with η, and D reaches maximum at $d = d_c \sim 1\,\sigma$. Again, this is because the inter-particle interaction are dominated by the repulsive and attractive branches in two regions separated by d_c, respectively.

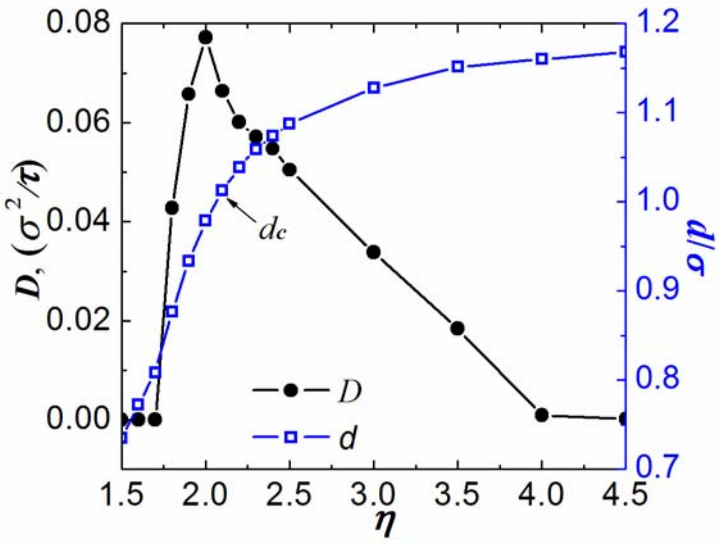

Figure 3.9. Diffusion constant D and inter-particle distance d as functions of the exponent η ($k_B T$ =0.23 ε) for tensionless membranes.

In Figure 3.10, both D and d monotonically increase with temperature and exhibit a sudden rise at $k_B T \sim 0.14\,\varepsilon$, implying a gel-to-fluid phase transition. The thermal expansion coefficient α_T of the model membrane is fitted at different regimes, as indicated in the figure. The relative error involved in calculating the diffusion constant is ~ 3%. The thermal expansion coefficient α_T of the membrane at different temperature ranges is fitted and indicated in the Figure.

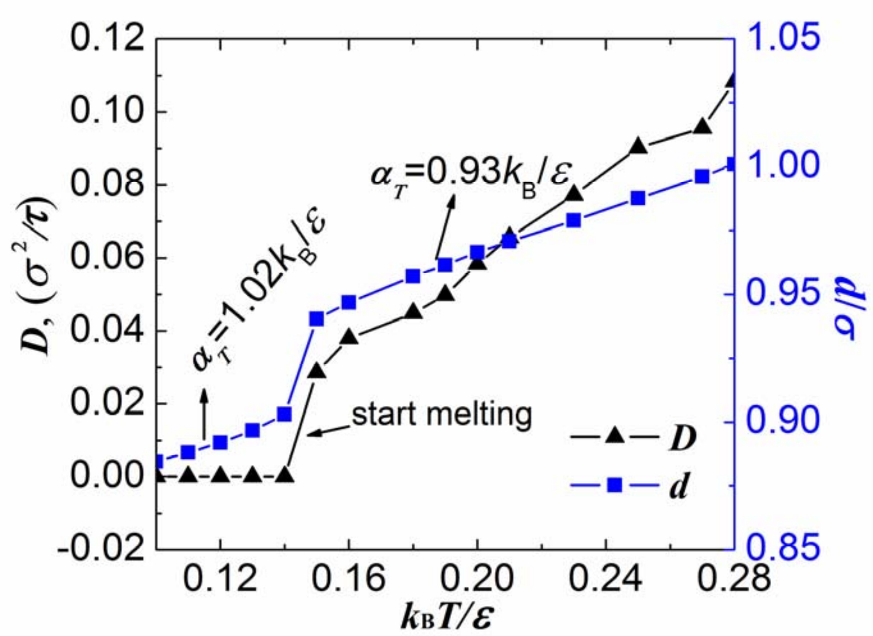

Figure 3.10. Diffusion constant D and inter-particle distance d as functions of temperature for tensionless membranes. The thermal expansion coefficient α_T of the membrane at different temperature ranges is fitted.

3.3.3 Bending rigidity and area compression modulus

We use Eq. (7) to fit the bending rigidity of the fluid membranes of the model. For each CGMD simulation, the tension, box size and energy take about $400\,\tau$ to equilibrate, and data collection started at $1200\,\tau$. Every $8\,\tau$, 2D nonuniform fast Fourier transform [112] was used to obtain the mode spectrum from the current membrane configuration. Bending rigidity was obtained by fitting the fluctuation spectrum into Equation (7) in the case of $\Sigma = 0$. A typical fluctuation spectrum from our MD simulations is shown in Figure 3.11.

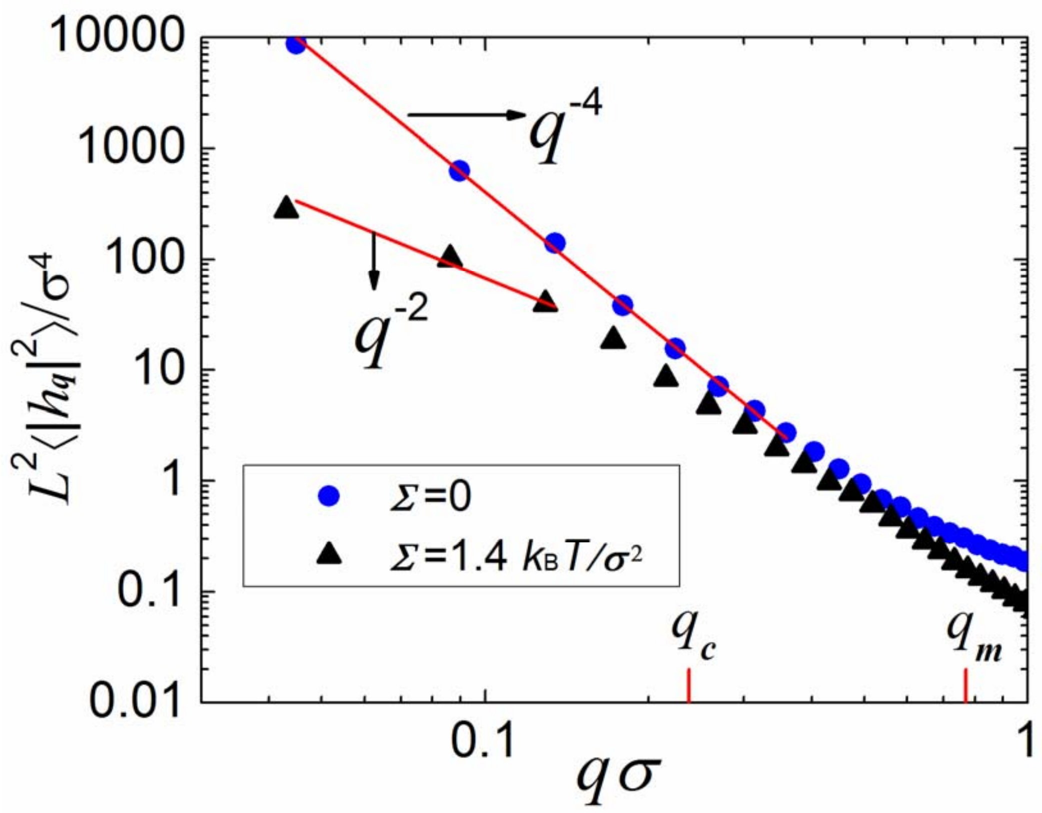

Figure 3.11. Fluctuation spectra under zero and finite tensions for planar membranes. Both q^{-4} and q^{-2} dependences are well predicted in simulations. The parameters used in the simulations are ζ =4, μ =3, θ_0 =0, and $k_B T = 0.23\,\varepsilon$.

The simulated fluctuation spectra of a square membrane (consists of 23595 particles) of side length $L \sim 140\,\sigma$ at zero and finite tensions were given in Figure 3.11. The q^{-4} dependence of the fluctuation spectrum under zero-tension is well predicted. At a finite membrane tension, there exists a critical wave number $q_c = \sqrt{\Sigma / B}$ below which the fluctuation amplitude starts deviating from the zero-tension curve and exhibits a clear q^{-2} dependence. Linear fitting of these two curves at zero and finite membrane tensions yields the bending rigidity and membrane tension, respectively. The fitted membrane tension is ~10% different from the imposed membrane tension. Corresponding to the wave length of ~8 σ , there exists an upper limit of $q = q_m$ beyond which Eq. (7) no longer holds. Both q_c and q_m are marked in Figure 3.11.

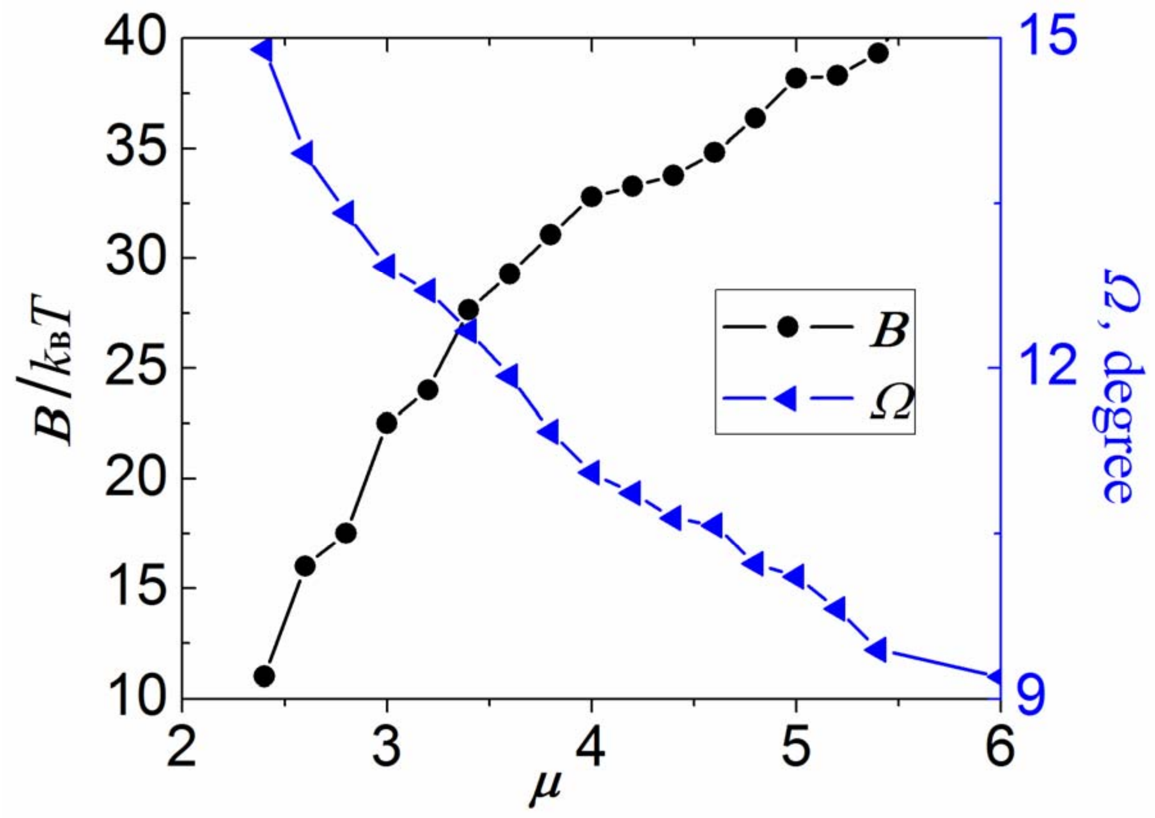

Figure 3.12. Membrane bending rigidity (in zero-tension states) monotonically increases with μ, while the order of alignment of the axis of symmetry of particles monotonically decreases with μ. Other parameters used in the simulations are η=2, ζ=4, θ_0=0, and $k_BT = 0.23\,\varepsilon$.

The parametric dependence of bending rigidity on μ, when $k_BT = 0.23\,\varepsilon$, is shown in Figure 3.12, where the bending rigidity is fitted at zero-tension simulations. The bending rigidity monotonically increases with μ. For μ in the range of 2.4 to 6, the obtained bending rigidity ranges from ~12 $k_\mathrm{B}T$ to ~40 $k_\mathrm{B}T$, which falls in the range of experimental data. There exists a threshold value of μ below which the membrane loses its integrity due to the weak orientation preference. The parameter μ also governs the order of alignment of particle-fixed vector $\mathbf{n}$, characterized by the average angle $\Omega = \cos^{-1}(<\mathbf{n}_i \cdot \mathbf{e}_z>)$, where $\mathbf{e}_z$ is the normal direction of the flat membrane. As shown in Figure 3.12, Ω ranges from about 9° to 15°, and decreases with increasing bending rigidity. The bending rigidity for fixed μ=3 but at different temperature and exponent ζ is listed in Table 3.4. Equation (7) was also used to fit the bending rigidity of membranes in the gel phase, which is an approximation.

Table 3.4. Membrane bending rigidity on the (T,ζ) plane. The x-axis represents temperature k_BT in units of ε, the y-axis represents ζ. The value in the table elements denotes bending rigidity in units of k_BT.

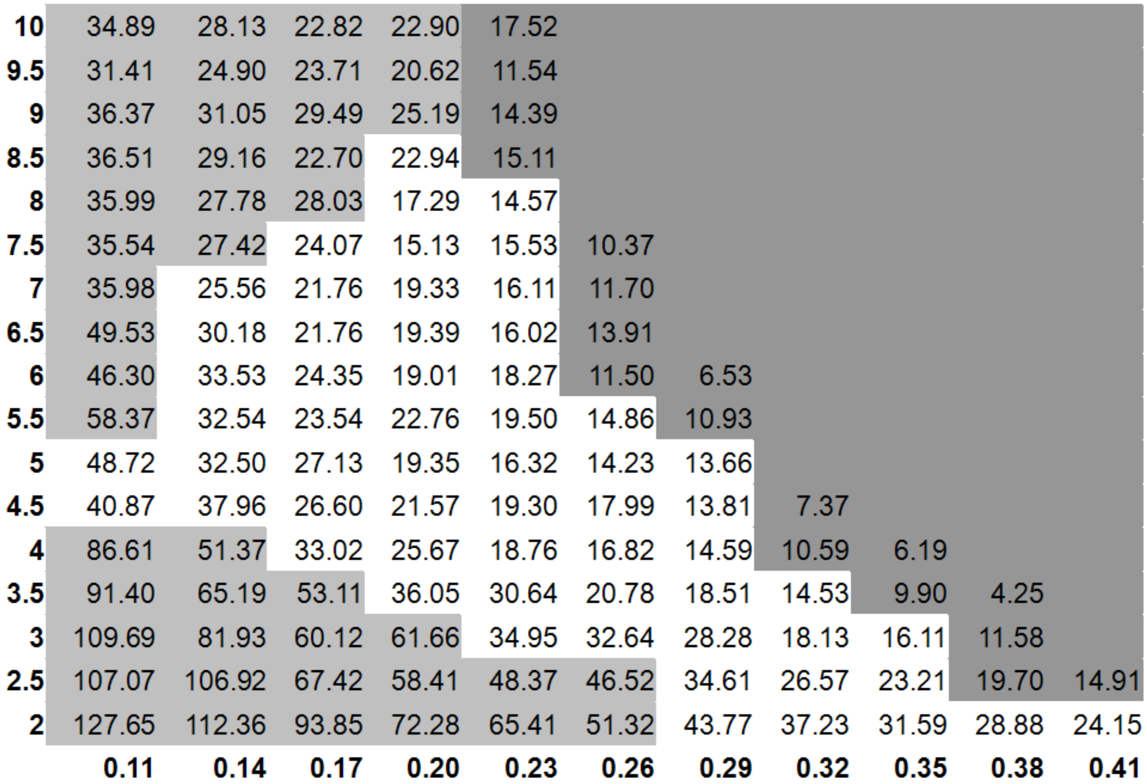

10	34.89	28.13	22.82	22.90	17.52						
9.5	31.41	24.90	23.71	20.62	11.54						
9	36.37	31.05	29.49	25.19	14.39						
8.5	36.51	29.16	22.70	22.94	15.11						
8	35.99	27.78	28.03	17.29	14.57						
7.5	35.54	27.42	24.07	15.13	15.53	10.37					
7	35.98	25.56	21.76	19.33	16.11	11.70					
6.5	49.53	30.18	21.76	19.39	16.02	13.91					
6	46.30	33.53	24.35	19.01	18.27	11.50	6.53				
5.5	58.37	32.54	23.54	22.76	19.50	14.86	10.93				
5	48.72	32.50	27.13	19.35	16.32	14.23	13.66				
4.5	40.87	37.96	26.60	21.57	19.30	17.99	13.81	7.37			
4	86.61	51.37	33.02	25.67	18.76	16.82	14.59	10.59	6.19		
3.5	91.40	65.19	53.11	36.05	30.64	20.78	18.51	14.53	9.90	4.25	
3	109.69	81.93	60.12	61.66	34.95	32.64	28.28	18.13	16.11	11.58	
2.5	107.07	106.92	67.42	58.41	48.37	46.52	34.61	26.57	23.21	19.70	14.91
2	127.65	112.36	93.85	72.28	65.41	51.32	43.77	37.23	31.59	28.88	24.15
	0.11	**0.14**	**0.17**	**0.20**	**0.23**	**0.26**	**0.29**	**0.32**	**0.35**	**0.38**	**0.41**

Figure 3.13 plots the kinetic and potential contributions and the total membrane tension as a function of the imposed area strain $\Theta_A = \Delta A / L^2$. The simulations were based on a square membrane of side length $L \sim 140\sigma$. At a critical area strain of ~0.09, membrane pore appears. This critical area strain agrees well with experimental data [4]. The kinetic and potential contributions to the membrane tension are on the same order of

magnitude, suggesting that neglecting the kinetic term would lead to misinterpretation of membrane tension. The resulting membrane tension is positive, and nearly linearly scales with the imposed area strain. The slope of the tension-strain curve in the large area strain regime corresponds to the area compression modulus, $K_A = \Sigma / \Theta_A$. A linear fitting of the curve yields $K_A \sim 18\, k_B T / \sigma^2$.

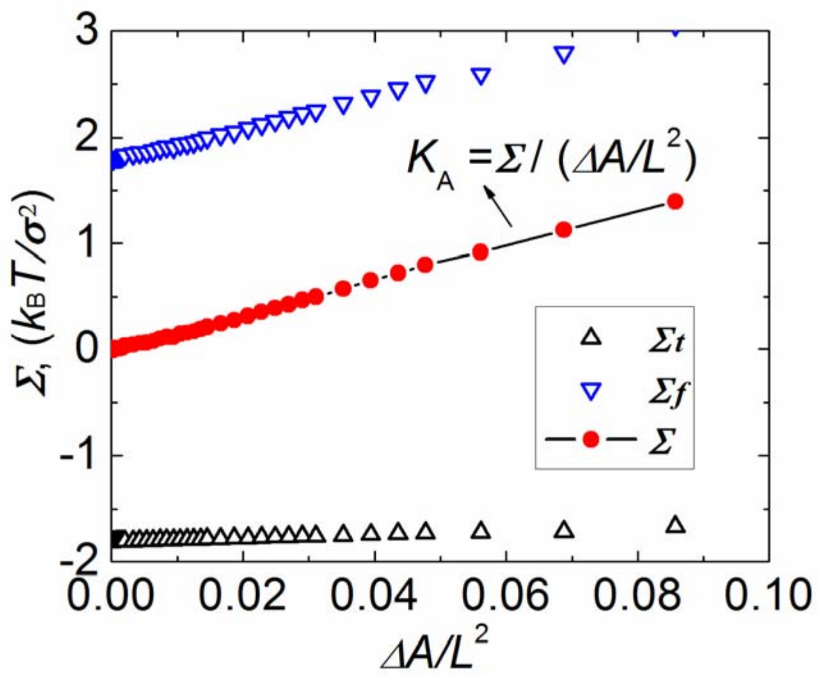

Figure 3.13. Membrane tension as a function of area strain $\Delta A / L^2$. Area compression modulus K_A is fitted to be about $18\, k_B T / \sigma^2$. The parameters used in the simulations are ζ =4, μ =3, θ_0 =0, and $k_B T = 0.23\, \varepsilon$.

3.3.4 Spontaneous curvature

In this section, we show that the spontaneous curvature can be easily defined in our model through model parameter θ_0. For bilayer membranes, “effective” spontaneous curvature may originate from molecule asymmetry [79], area mismatch between two leaflets [113] of the bilayer, or protein-lipid hydrophobic mismatch, or protein-assisted curvatures [11, 114]. Spontaneous curvature plays a critical role in determining shape transformations in vesicles and red blood cells [3, 10], and also thought to be related to lipid-sorting in biological membranes [115]. Figure 3.14 demonstrates phase separation in a binary lipid membrane. The number ratio of the particle types A (red) and B (green) is 1:10. We assign different θ_0 and μ to the different combinations of particle pairs, i.e., $\theta_0^{\mathrm{AA}} = \theta_0^{\mathrm{AB}} = 11.5^\circ$, $\theta_0^{\mathrm{BB}} = 0^\circ$, $\mu^{\mathrm{AA}} = \mu^{\mathrm{AB}} = 6$, and $\mu^{\mathrm{BB}} = 3$. Other parameters used in the simulations are: $k_B T = 0.23\varepsilon$, ζ =4. It should be noted that the spontaneous curvature difference between the two species results in a line tension that induces the phase separation. Starting from random mixture of the particle species, our CGMD simulations show that the two lipid species demix rapidly, forming small domains ($t = 800\tau$). The small domains gradually grow into budding domains ($t = 4000\tau$).

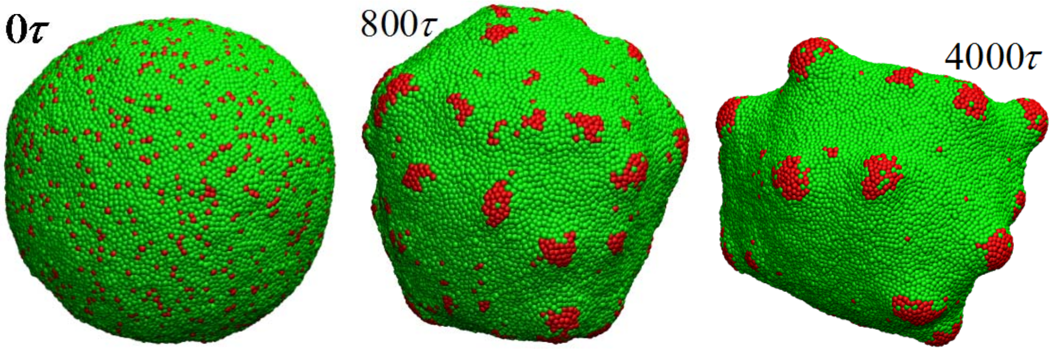

Figure 3.14. Spontaneous curvature (related to the model parameter θ_0) induced budding domains.

3.3.5 Length and time scale mapping

In the chain-of-bead models in which each lipid molecule is represented by a chain of beads, the repulsive potentials between beads not only determine the bead size in the membrane lateral direction, but also define the bead size in the membrane thickness direction. So for chain-of-bead membrane models, directly matching the thickness of the model membrane with that of the real bilayer membrane can lead to the length scale mapping. Different from the chain-of-bead membrane models, our membrane model is only one-particle-thick. The repulsive branch of the potential does define a particle size in the membrane lateral direction, but not in the out-of-plane direction. In other words, the membranes of our model do not have a explicitly defined thickness, they are truly 2D membrane. Therefore, we can not directly map the length scale through real membrane thickness.

For biological membranes, the bending rigidity B and the area compression modulus K_A follow approximately the relationship of the thin shell theory,

$$B = K_A d_{th}^2 / 12 , \tag{25}$$

where d_{th} is the membrane thickness. The fact that the bending rigidity B is related to the area compression modulus K_A and the membrane thickness via Eq. (25) is simply because bending the membrane causes membrane stretching or compression at locations not on the neutral plane. We can use Eq. (25) to find the "thickness" of the one-particle-thick membrane of this model. Substituting the fitted bending rigidity and area compression modulus ($K_A \sim 18\, k_{\mathrm{B}}T / \sigma^2$ and $B \sim 20\, k_{\mathrm{B}}T$) into Eq. (25), we obtain the thickness d_{th} to σ ratio, i.e., $d_{th} / \sigma \sim 3.7$. Since σ represents the particle size in the membrane lateral direction, this ratio is actually the particle aspect ratio of particle of the model. For the real membrane thickness, $d_{th} \sim$ 5 nm, which follows that $\sigma \sim 1.4$ nm. Note that the exact numerical value in this length mapping is not critical to the CGMD simulations. Nevertheless, we obtain a sense of the order of magnitude of the length scale.

A typical value for the diffusion constant of lipids in real phospholipid membranes is about 1 $\mu\mathrm{m}^2$/s [116]. The diffusion constant of our model is $\sim 0.1\, \sigma^2 / \tau$, assuming $0.1\, \sigma^2 / \tau$ = 1 $\mu\mathrm{m}^2$/s, we obtain an estimation of the time scale of the model as $\tau \sim 0.1$ μs.

Reduced unites are typically used for solvent-free coarse-grained models, and lipid length and diffusion constant are in practice used to map the reduced units back to real physical quantities. However, the speed-up process due to the coarse-graining may not be the same to all motions in system. Adoption of the soft-core potential in this model certainly facilitates the particle diffusion to a large extent.

Both the length and time scales are about one order of magnitude higher than the chain-of-bead coarse-grained model [55]. Here the length scale comparison is based on the fact that each particle in our model represents a few lipids in two leaflets of the bilayer. So the degrees of freedom involved in the same membrane area are about one order of magnitude fewer than the chain-of-bead models.

3.4 Volume-control algorithm for fluid vesicles

In biological processes, cells regulate their enclosed volumes by controlling the number of water molecules in the cytoplasm through the osmotic pressure difference across the membrane. Assuming V_0 is the osmotically desired vesicle volume at which the osmotic pressure difference across the membrane vanishes. Denote $\hat{V}$ the volume in the absence of osmotically active molecules in solution and inside the vesicle. Therefore, $\hat{V}$ is solely determined by the membrane elasticity. The actual equilibrium vesicle volume V is a competition of osmotic potential and the membrane elastic energy. For a small deviation of the volume V from the osmotically desired volume V_0, an energy penalty arises. For simplicity, we assume that the energy penalty takes a quadratic form:

$$E_V = \frac{1}{2} K_V \left(\frac{V}{V_0} - 1 \right)^2 , \tag{26}$$

where K_V is a constant related to the temperature, V_0, and the concentration of the osmotically active molecules [3]. In numerical simulations, K_V generally sets a higher energy scale than the bending rigidity, and thus can be regarded as a rather stiff volume spring. The hydrostatic pressure difference across the membrane, which is the negative of the osmotic pressure, is

$$p = \frac{K_V}{V_0}\left(1 - \frac{V}{V_0}\right), \tag{27}$$

where positive p means outward pressure. From Eq. (27), one follows that the hydrostatic pressure difference p is a function of the equilibrium vesicle volume V but usually not vice versa since V also depends on the membrane elasticity, as pointed out earlier.

To account for the volume constraint imposed by the enclosed water, the external potential E_V defined in Eq. (26) needs to be incorporated into the total system free energy as an external potential, which requires computation of the instantaneous enclosed volume of vesicles. Calculation of the volume enclosed by a surface comprised of discrete particles necessitates triangulation or tessellation of the surface. Once the triangulation is done, surface area and volume can be simply calclauted as the sum of the area of all triangles and tetrahedrons (formed by picking a space-fixed point), respectively. For such a dynamically evolving particle system, triangulation poses computational challenges for the following two reasons. First, triangulation needs to be performed at each time step due to random dynamic motion of particles. An efficient triangulation algorithm is highly desired or the simulation becomes unaffordable. Second, algorithms for exact triangulation developed in computational geometry exist only for convex shapes, whereas the conformations of the vesicles under consideration may evolve into concave shapes. To circumvent the difficulties, we assume that the particles are of hexagonal close packing, and propose an approximate local triangulation algorithm as follows. For an arbitrary particle i, we identify its six nearest neighbors, forming six triangles surrounding particle i (shown in Figure 3.15). Consider an triangle formed by particles i, j, and k, the volume of the corresponding tetrahedron formed by the triangle and the origin O (which can be arbitrary) can be simply computed as,

$$V_{O-ijk} = \frac{1}{6}\left(\mathbf{r}_j \times \mathbf{r}_k\right) \cdot \mathbf{r}_i \,. \tag{28}$$

The expression in Eq. (28) with only simple operations involved makes it convenient to compute the forces imposed on the particles due to the volume constraint, since force calculation involves taking derivative of V_{O-ijk} with respect to the position vector. The sequence of vectors $\mathbf{r}_j$ and $\mathbf{r}_k$ are chosen such that $\mathbf{r}_j \times \mathbf{r}_k$ points to the local outward normal of the vesicle. This is easily accomplished since the local outward normal is implied from the particle-fixed vector $\mathbf{n}_i$, but may be troublesome for other models in which the particles only carry translational degrees of freedom. In addition, for an triangle formed by particles i, j, and k, (particle j and k are first-nearest neighbors of particle i) the area can be computed as,

$$A_{ijk} = \frac{1}{2}\sqrt{\left(\mathbf{r}_{ji}\cdot\mathbf{r}_{ji}\right)\left(\mathbf{r}_{ki}\cdot\mathbf{r}_{ki}\right)-\left(\mathbf{r}_{ji}\cdot\mathbf{r}_{ki}\right)^2} \tag{29}$$

where $\mathbf{r}_{ji} = \mathbf{r}_j - \mathbf{r}_i$ and $\mathbf{r}_{ki} = \mathbf{r}_k - \mathbf{r}_i$.

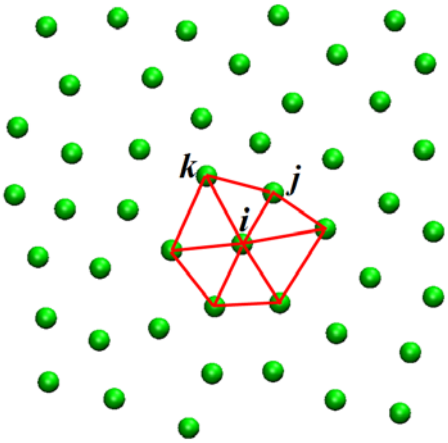

Figure 3.15. Schematics of the local triangulation algorithm.

This local triangulation algorithm is robust, simple and thus efficient. Due to the random Brownian motion of the particles, the hexagonal close-packed distribution is only approximately satisfied. Nevertheless, compared to the exact triangulation (Delaunay triangulation) for a spherical vesicle, the relative error of the vesicle volume calculated by our local triangulation scheme is only about 0.2%. The accuracy of this algorithm was also verified by its effective volume control of the vesicles in the shape transformation simulations (presented later).

3.5 Cauchy-Born analysis and zero-temperature properties

In our mesoscopic membrane model, an orientation-dependent inter-particle potential accounts for the two energies in the continuum description of membranes: bending energy and area stretching energy. Though the particle-based model stabilizes the membrane at the fluid phase, one may consider the particle aggregate as a lattice at zero-temperature case, where each particle is 6-coordinated (with 6 nearest neighbors). Through Cauchy-Born rule [117], we can relate the effective membrane properties including bending rigidity and area stretching modulus to the inter-particle potential parameters at zero-temperature. Here we treat the particle membrane as a crystal structure with a triangle lattice. A primitive unit cell can be identified, which contains only one particle but three "bonds", as shown in Figure 3.16(a). Assume that the unit cell is first biaxially stretched with a stretch λ, followed by a bending to curvature c (cylindrical) as shown in Figure 3.16(b). Following the Cauchy-Born hypothesis, the three "bonds" in the unit cell after the deformation can be represented by the two continuum deformation measure: λ and c. On the one hand, from continuum modeling, the strain energy density can be written as, assuming small deformation:

$$E(\lambda, c) = \frac{1}{2} K_A \left(\lambda^2 - 1\right)^2 + \frac{1}{2} B c^2 \tag{30}$$

On the other hand, the strain energy density can also be computed from the inter-particle interactions,

$$E(\lambda, c) = \frac{\sum_{"bond"} U\left(\mathbf{r}_{ij}, \mathbf{n}_i, \mathbf{n}_j\right)}{\sqrt{3} d_0^2}, \tag{31}$$

where the particle positions and orientations can be determined from the deformations λ and c imposed on the lattice structure. The essential idea of the Cauchy-Born rule is that for crystal structures, one can correlate the atomistic particle positions with descriptions of continuum deformation. Noting that the right-hand sides of Eq. (30) and Eq. (31) are equal, the bending rigidity B and area compression modulus K_A can thus be related to the inter-particle potential parameters. Through lengthy but straightforward calculations, the bending rigidity is obtained as,

$$B \sim \mu\varepsilon\,, \tag{32}$$

and the area expansion modulus is

$$k_{\mathrm{A}} \sim \eta^2 \frac{\varepsilon}{\sigma^2}\,. \tag{33}$$

In addition, the spontaneous curvature c_0 is related to θ_0 via

$$c_0 \sim 2\sin\theta_0 / d_0\,, \tag{34}$$

where d_0 is the inter-particle distance, as illustrated in Figure 3.1. Note that in order to simplify our analysis, we assume that the particles only interact with their nearest neighbors. However, in the design of the inter-particle interactions, the interactions of the second-nearest neighbors are taken into account. We thus emphasize that the above analysis only provides scaling laws that guide tuning of the mechanical properties through specific parameters in the potential, not exact relations. Finally, one can conclude from Equations (32), (33), and (34) that bending rigidity, area expansion modulus, and spontaneous curvature can be tuned by varying μ, η, and θ_0, respectively.

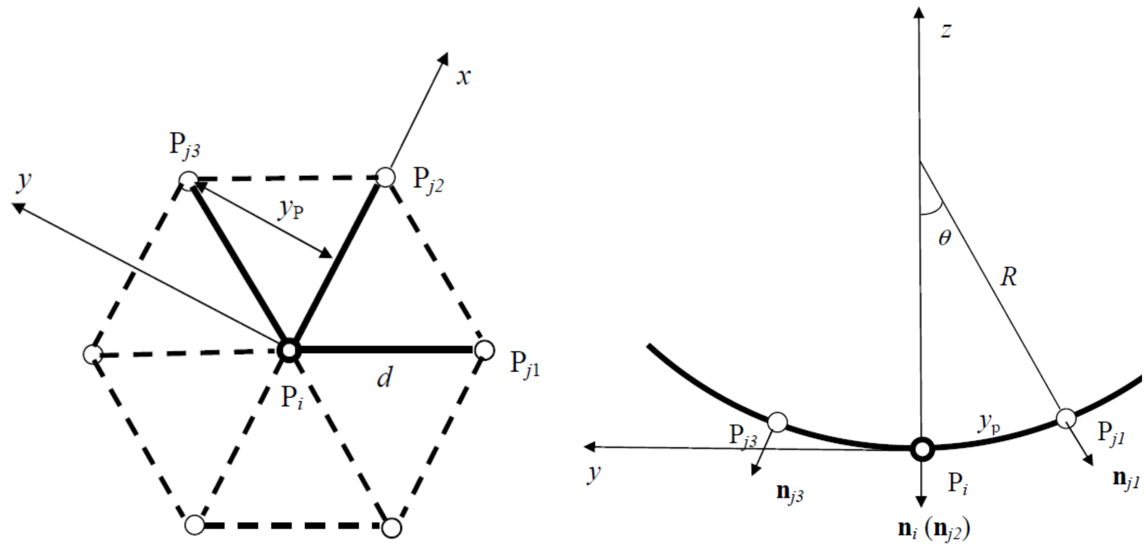
x
P_{j3}
y
P_{j2}
y_{P}
P_{j1}
P_i
d
z
θ
R
P_{j3}
y_{p}
P_{j1}
y
$\mathbf{n}_{j3}$
P_i
$\mathbf{n}_{j1}$
$\mathbf{n}_i\ (\mathbf{n}_{j2})$

(a) (b)

Figure 3.16. Invoking the Cauchy-Born hypothesis to analytically derive the relationships between the effective properties of the model membrane and the inter-particle potential parameters. (a) Biaxial stretch λ, (b) bending to curvature c.

As stated above, the first-neighbor calculation only yields general scaling relations. Next, we conduct numerical calculations to obtain the exact but tabulated relations between membrane elastic properties at zero temperature and the model parameters via the Cauchy-Born hypothesis. As shown in Figure 3.17, a flat membrane and a tube-like membrane of 2D hexagonal close-packed lattice are used in numerical calculations. In calculating the interaction energy, all interaction pairs within the cutoff radius are considered.

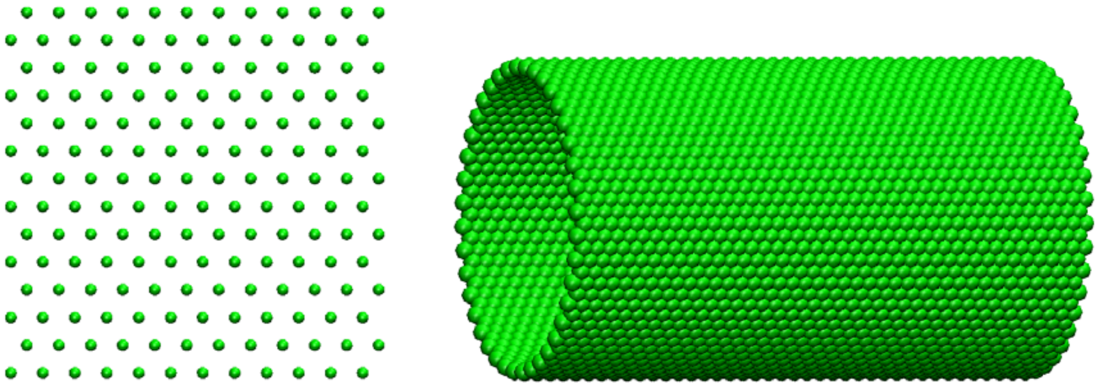

(a) (b)

Figure 3.17. A flat membrane (a) and a membrane tube (b) of 2D hexagonal close-packed lattice.

The bending rigidity of the zero-temperature membrane was numerically computed using an infinitely long tube (periodic boundary condition was used in calculations) as shown in Figure 3.17(b). The bending energy $U_b\left(\mathbf{r}_{ij},\mathbf{n}_i,\mathbf{n}_j\right)$ in the inter-particle potential given in Eq. (12) is defined as,

$$U_b\left(\mathbf{r}_{ij},\mathbf{n}_i,\mathbf{n}_j\right)=\begin{cases}\left[1-\phi\left(\hat{\mathbf{r}}_{ij},\mathbf{n}_i,\mathbf{n}_j\right)\right]\varepsilon & ,r<r_{\min}\\ u_A\left(r\right)\left[\phi\left(\hat{\mathbf{r}}_{ij},\mathbf{n}_i,\mathbf{n}_j\right)\text{-}1\right] & ,r_{\min}<r<r_c\end{cases}. \tag{35}$$

Via the Cauchy-Born hypothesis, the membrane bending energy per unit area $\hat{E}_b$ is calculated as a function of $c^2/2$, as plotted in Figure 3.18. The straight line in Figure 3.18 manifests the quadratic relation between the bending energy and the curvature c. The bending rigidity was fitted as,

$$B = 3.4\mu\varepsilon \tag{36}$$

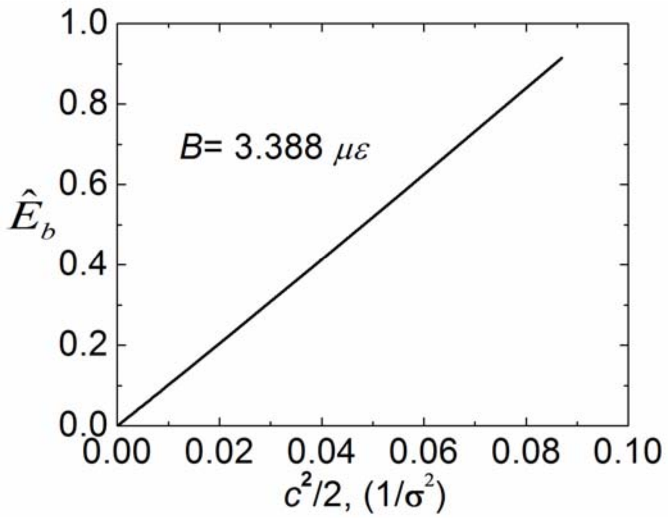

Figure 3.18. The bending rigidity of the zero-temperature membrane.

Chapter 4

Configurations of fluid vesicles

In cellular biology, fluid vesicles can be considered as simplified model of cell membranes and thus have been intensively used in experiments to study various biological processes [118-120]. In biomedical engineering, artificial vesicles (called liposomes in this field) have been used for drug delivery in the pharmaceutical market for decades [121]. Supported membranes have been proposed for many promising scientific and practical applications, such as exploring cell adhesion and developing membrane-based biosensors [17, 122].

Fluid vesicle configurations in equilibrium state have been extensively studied in the past several decades both experimentally and theoretically [3, 123]. Among several elastic models for fluid vesicle shape determination,[3] the spontaneous curvature model searches for the equilibrium shapes of vesicles by minimizing the curvature-elastic energy E_b given in Eq. (1) under the fixed area-to-volume ratio constraint [80] and a given spontaneous curvature c_0. One notes the intimate relation between the spontaneous curvature model and our mesoscopic model, which ensures that the present model is well suited for the simulation of vesicle shape transformations. In comparison, the bending energy and the spontaneous curvature in our mesoscopic model are incorporated in the orientation-dependent interaction of the potential and the potential parameter θ_0, respectively. The much larger in-plane modulus K_A sets a high energy scale than the bending rigidity B. This in-plane and out-of-plane energy scaling ensures that the simulated membrane in our model deforms nearly inextensibly, which fulfills the inextensibility condition imposed in the spontaneous curvature model. As an added feature, since the membrane particles are allowed to laterally diffuse and thus simulate the in-plane viscous effect, our model is capable of elucidating the rate effect of volume change on dynamics of shape transformations.

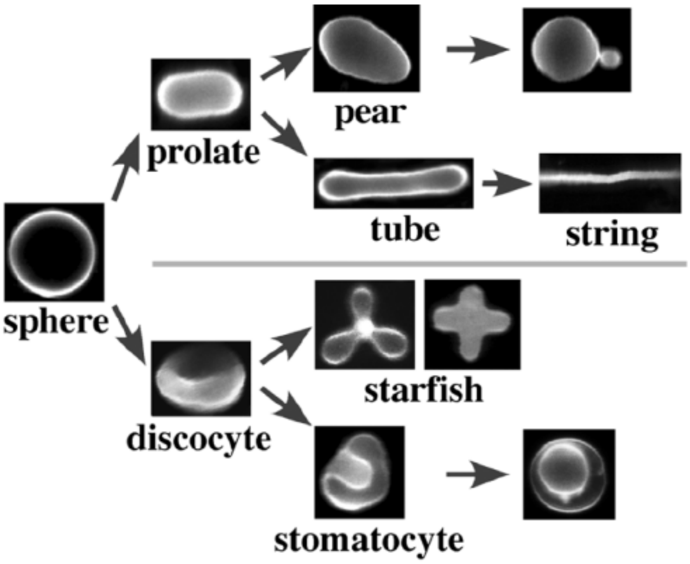

Figure 4.1. Shape change pathways of fluid vesicles induced by the volume change. The vesicle volume was controlled by adding salt into the solution. Reprinted with permission from [118]. Copyright 2008 American Physical Society.

4.1 Static shape transformations

We restrict our simulations on homogeneous vesicles, though the present model can simulate equally well shape transformations of heterogeneous vesicles. All our simulations start with a pre-assembled, spherically shaped vesicle consisting of totally 5861 particles. We assume that the flip-flop of lipid molecules between the outer and inner leaflets of the bilayer is a rare event in the course of vesicle shape transformation, and thus prescribe a constant θ_0 to all the particles in the simulation model. Here, positive (negative) θ_0 corresponds to a convex (concave) spontaneous. In experiments, osmotic pressure difference across the membrane is modulated by adding salts into the solution, effectively reducing the enclosed volume and driving the shape transformation of vesicles. We characterize the area-to-volume ratio by the reduced volume v, defined as the ratio of the instantaneous volume (V) of the vesicle and the volume (V_{sphere}) of the spherical vesicle of equal area. The enclosed volume of the vesicle is then gradually reduced to the desired volume V_0 with a constant volume change rate $\dot{v}$ using the volume-control algorithm described in the previous section. Afterwards, simulation continues for a sufficiently long period until the vesicle reaches its equilibrium conformation.

Figure 4.1 displays the equilibrium shapes and shape transformation pathways of vesicles at three different spontaneous curvatures. We vary the volume change rate by at least an order of magnitude to explore the possible rate dependence. For a negative spontaneous curvature ($\theta_0 = -2.3^{\circ}$), reducing the volume results in a shape transformation pathway consisting of a sequence of oblate, biconcave, stomatocyte shapes and inward budding. This pathway appears to be independent of the imposed volume change rates. For a positive spontaneous curvature ($\theta_0 = 3.4^{\circ}$), the first two shape transformations result in prolate and dumbbell shapes. Further reducing the volume leads to shape bifurcation depending on the volume change rate. A slow volume change rate of $\dot{v} = 1.94 \times 10^{-4} \tau^{-1}$ induces outward budding when further reducing the volume of the vesicle from the dumbbell shape. In contrast, a high volume change rate of $\dot{v} = 1.75 \times 10^{-3} \tau^{-1}$ leads to dumbbell-tubular shape transformation. At zero spontaneous curvature, the vesicle shape transformation depends on the imposed volume change rate and bifurcates into two distinct pathways, each of which resembles the pathway for the cases of the positive and negative spontaneous curvatures. Independent of volume change rate, the vesicle follows prolate-to-dumbbell shape transformation for the first two steps for relatively large reduced volume ($v \geq 0.7$). For smaller reduced volume, the shape transformation bifurcates depending on the imposed volume change rate. A low volume change rate ($\dot{v} = 1.94 \times 10^{-4} \tau^{-1}$) promotes formation of tubular shape. However, different from the pathways seen in the positive spontaneous curvature, the zero spontaneous curvature does not promote bifurcation from dumbbell shape to outward budding. On the other hand, the high volume change rate ($\dot{v} = 1.75 \times 10^{-3} \tau^{-1}$) promotes biconcave-stomatocyte-inward budding transformation. It should be pointed out that in our simulations such transformation cannot be induced from the dumbbell shape but directly from the spherical shape (indicated by a dashed arrow in Figure 4.1). This may be due to the high energy barrier from dumbbell to biconcave shapes as compared to the thermal energy. All these equilibrium shapes and shape transformation pathways agree strikingly well with the phase diagram based on the spontaneous curvature model [80] and a recent experiment.[118] Besides yielding the shape transformation pathways, our simulation results provide insights as to how to tune the key experimental parameters quantitatively in order to induce desired shapes and shape transformations.

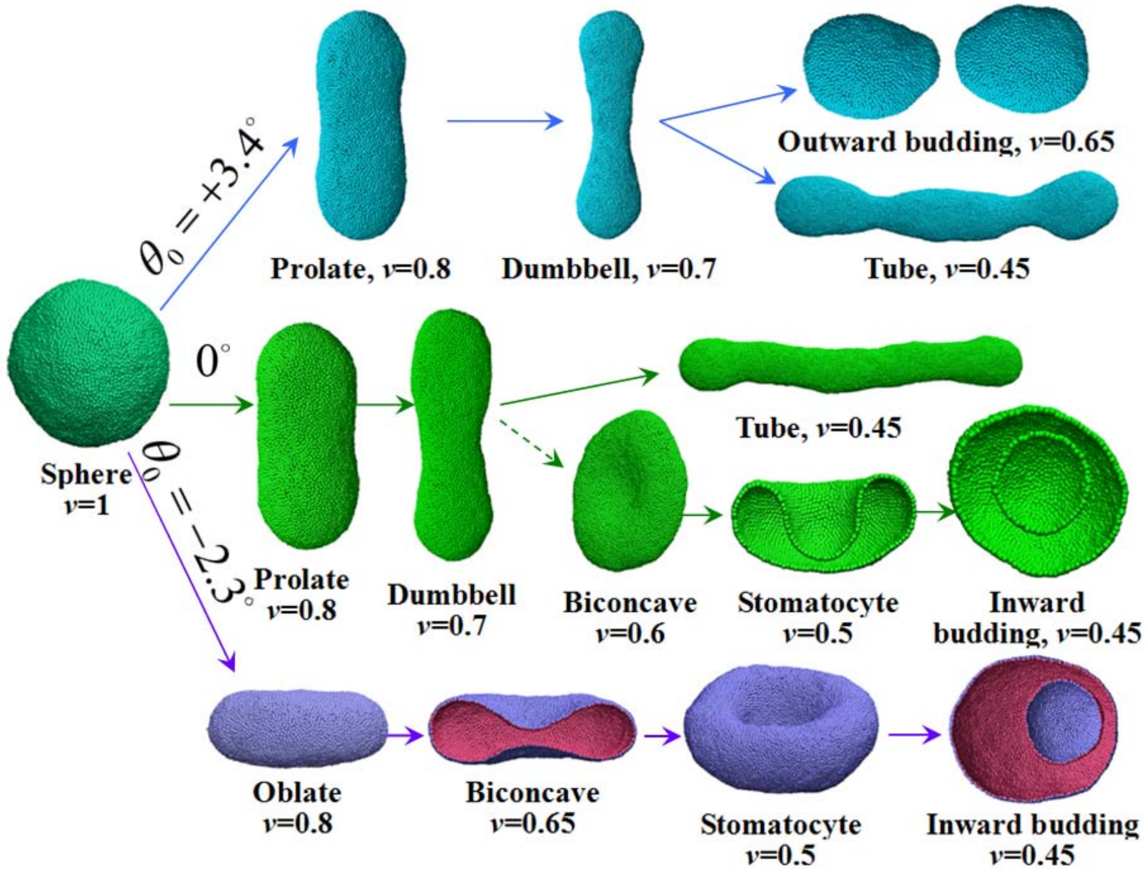
$\theta_0 = +3.4^\circ$
Prolate, ν=0.8
Dumbbell, ν=0.7
Outward budding, ν=0.65
Tube, ν=0.45
Sphere
ν=1
0°
Tube, ν=0.45
$\theta_0 = -2.3^\circ$
Prolate
ν=0.8
Dumbbell
ν=0.7
Biconcave
ν=0.6
Stomatocyte
ν=0.5
Inward
budding, ν=0.45
Oblate
ν=0.8
Biconcave
ν=0.65
Stomatocyte
ν=0.5
Inward budding
ν=0.45

Figure 4.1. Map of vesicle equilibrium shapes and shape transformation pathways. The upper pathway branch ($\theta_0 = 3.4^\circ$): sphere, prolate, dumbbell, and outward budding (or tubular) shape for slow (or fast) volume change rate; the lower pathway branch ($\theta_0 = -2.3^\circ$): sphere, biconcave, stomatocyte, and inward budding; the central pathway branch ($\theta_0 = 0^\circ$): spherical, prolate, and dumbbell shapes, and then bifurcates into two sub-pathways. A slow volume change rate promotes dumbbell to tube shape transformation; for fast volume change rate, the vesicle follows a biconcave-stomatocyte-inward budding transformation pathway. The biconcave shape cannot be directly induced from the dumbbell shape, but from the spherical shape.

To understand the mechanics of vesicle shape transformation, we analyzed the dynamic evolution of the hydrostatic pressure and membrane tension. Figure 4.2 plots membrane tension and hydrostatic pressure at two representative spontaneous curvatures, corresponding to two shape transformation pathways: sphere-prolate-dumbbell-tube transformation for $\theta_0 = 2.4^{\circ}$ and sphere-prolate-dumbbell-biconcave transformation for $\theta_0 = 0^{\circ}$. As an overall trend, as the volume of the vesicle reduces, the hydrostatic pressure exerted on the vesicle increases. From a force-balance point of view, a negative (compressive) membrane tension is necessary to balance a positive (outer-to-inner direction) hydrostatic pressure in a convex membrane segment. Figure 4.2 implies such force balance is approximately satisfied during vesicle shape transformation. It is also seen that the hydrostatic pressure abruptly decreases when the vesicle transforms from a convex to a concave conformation (e.g., dumbbell-to-biconcave transformation).

It should be pointed out that at given hydrostatic pressure the vesicle may be stabilized at different conformations. For example, for zero spontaneous curvature at hydrostatic pressure of ~0.01 ε/σ^2, the vesicle may adopt either a biconcave or dumbbell shape (see Figure 4.2(a)). From mechanics point of view, hydrostatic pressure and volume control play roles of load-controlled and displacement-controlled loading. We adopt the latter loading mechanism since it better mimics the relevant experimental conditions.

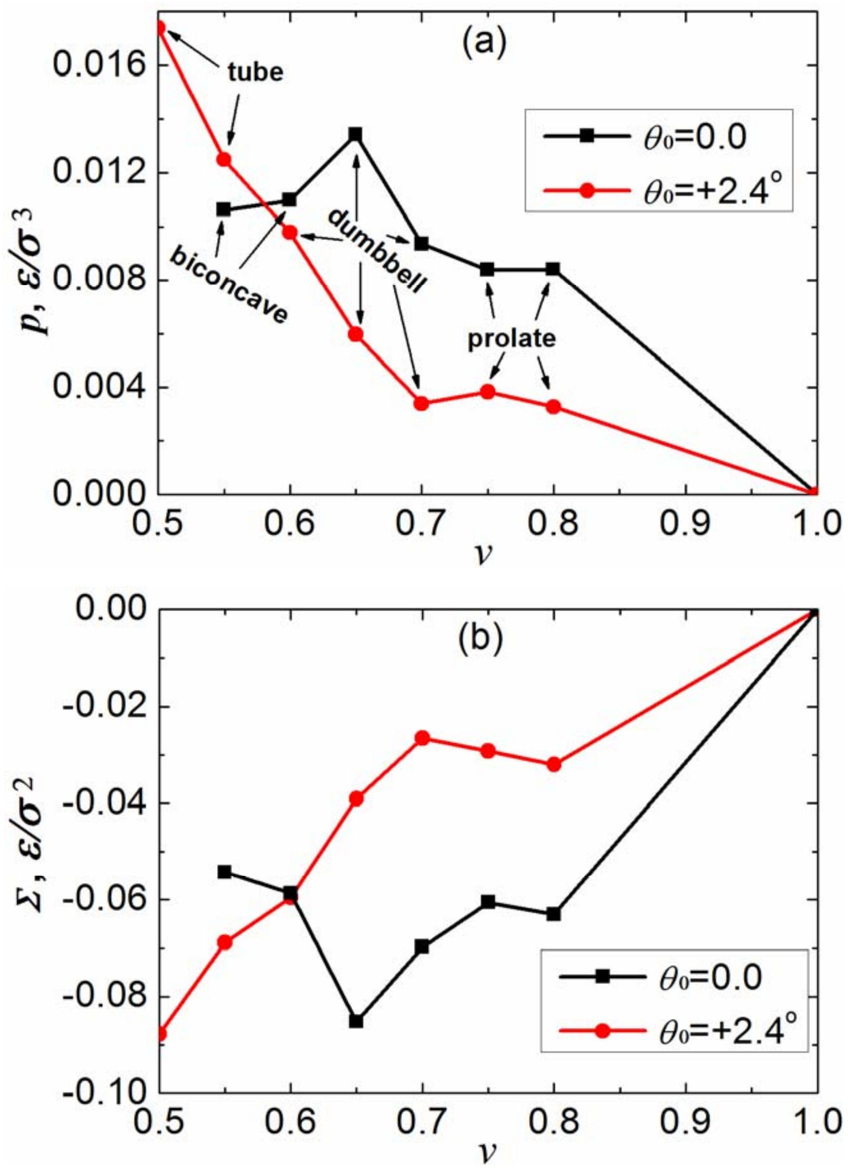

Figure 4.2. Changes of the hydrostatic pressure (a) and average membrane tension (b) with vesicle volume.

4.2 Dynamic shape transformations

Vesicle shape transformation is a result of strain energy relaxation of the vesicle under the prescribed enclosed volume. Considering the vesicle in our model as a viscous material whose internal stress state depends on the loading rate (the volume change rate in this case), which in turn regulates the dynamic shape transformation of the vesicles. By performing a non-equilibrium molecular dynamics simulation of the Couette flow in a planar membrane, the viscosity of the fluid membrane was found to be in the order of 1 $\varepsilon\tau/\sigma^2$ (for 2D fluid membranes, viscosity is defined as the force per unit length divided by the velocity gradient). For a low volume change rate, the vesicle has sufficient time to relax its internal stresses. On the other hand, for a relatively high volume change rate, significant stresses in the membrane could be accumulated within the vesicle. The dynamic shape transformation pathways induced by different volume change rates shown in Figure 6 clearly manifests such a dynamic stress relaxation mechanism. For the fast volume change rate ($\dot{v}=1.75\times10^{-3}\tau^{-1}$), the shape transformation follows a pathway sequence of spherical, triconcave, asymmetric biconcave, and biconcave shapes. Differently, a slow volume change rate ($\dot{v}=1.94\times10^{-4}\tau^{-1}$) generates a shape transformation pathway consists of spherical, prolate, dumbbell, and tubular shapes. It should be mentioned that, unlike the shapes presented in Figure 4 that are dynamically equilibrated, the conformations in Figure 6 are snapshots in the dynamic volume change processes, which are not equilibrium shapes.

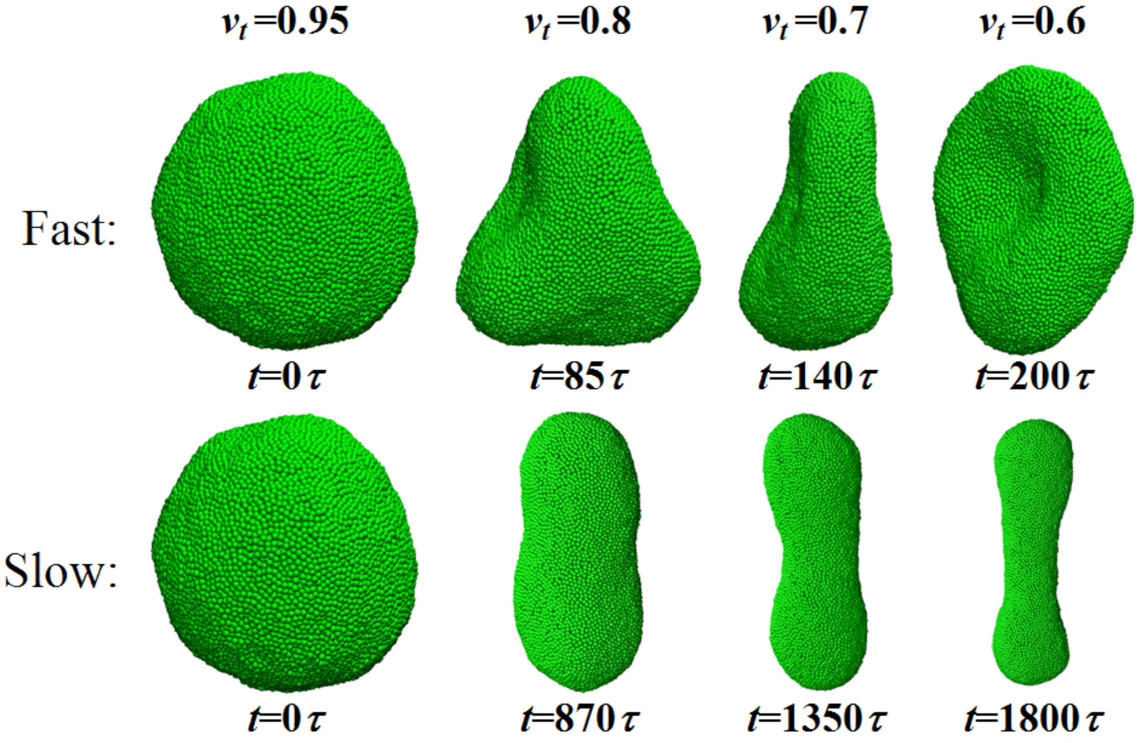

Figure 4.3. Effect of the volume-change rate on the vesicle shape transformation pathways. Top panel: shape transformation pathway for fast volume-change rate ($\dot{v} = 1.75 \times 10^{-3} \tau^{-1}$); bottom panel: shape transformation pathway for low volume-change rate ($\dot{v} = 1.94 \times 10^{-4} \tau^{-1}$).

To see the role of the stress relaxation in vesicle shape transformation, Figure 7 shows the evolutions of the shear stress (a) and membrane tension (b) with changing vesicle volume. The shear stress is calculated by the virial formula. For the high volume change rate, the shear stress and membrane tension undergo large undulations in the period of volume change from $v = 1.0$ to 0.6. Afterwards, the shear stress is fully relaxed to zero, while the membrane tension is relaxed to a state set by the force balance with the hydrostatic pressure. The undulations in the fully relaxed state are mainly caused by thermal fluctuations. In contrast, for the low volume change rate, both the shear stress and membrane tension undergo small undulations in the entire simulation period, indicating that the vesicle is almost fully relaxed.

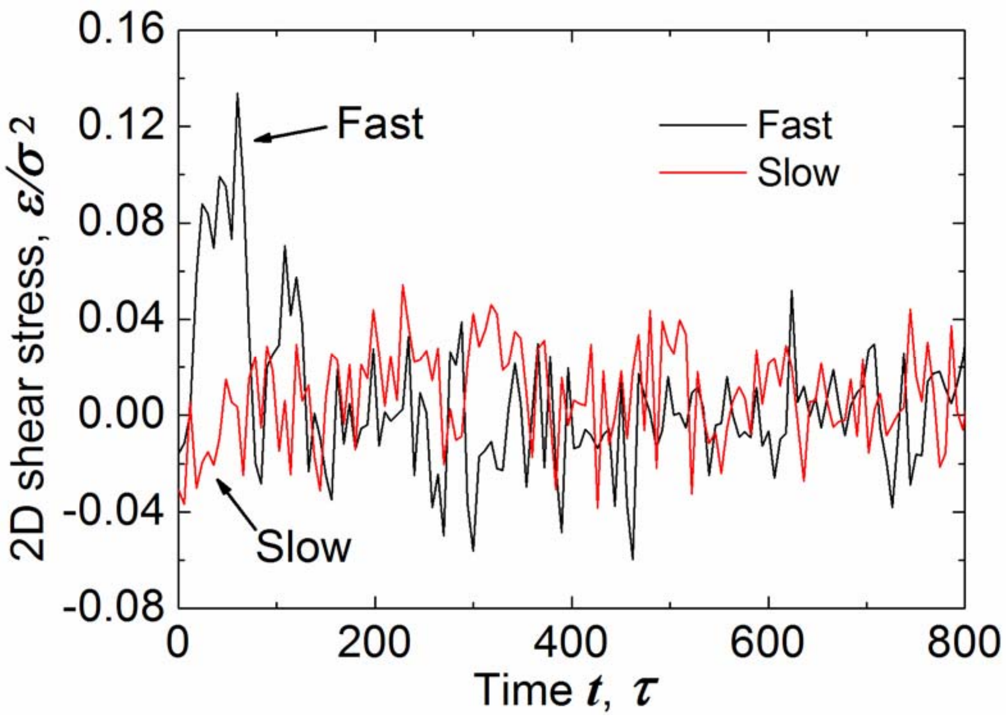

(a)

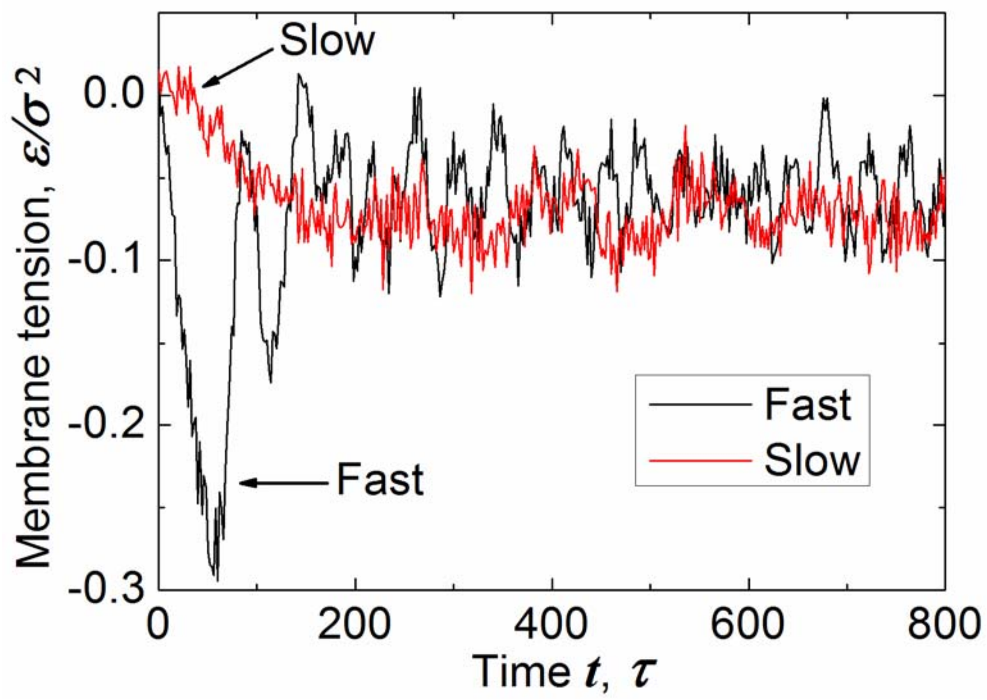

(b)

Figure 4.4. Stress relaxation in dynamically evolving homogeneous vesicles at different volume-change rates. (a) Shear stress; (b) membrane tension. Note that shear stress is shifted by subtracting the average value, so the resulting average value in (a) is zero.

4.3 Conclusions

Shape transformation pathways of homogeneous vesicles were elaborated together with analyses of dynamic stress relaxation. The produced shape transformation pathways agree strikingly well with the experimental observations and those of previous elastic membrane models, thereby validating the simulation model. Given its great ease in modeling arbitrary vesicle conformations, the present model may be exploited to the studies of vesicle-substrate interactions,[124, 125] vesicle fusions and fissions,[39, 96, 126] membrane-protein interactions,[96] and membrane tethering,[70] where the vesicles under investigations may adopt complex morphologies.

In contrast to elastic membrane models for which equilibrium shapes of vesicles are of the major concern, particles in our numerical model are diffusible in the lateral direction, thereby allowing the study of rate dependence of vesicle shape transformations. Our simulations showed that the shape transformation pathways can be altered by different volume-change rates, which clearly manifests the role of in-plane viscosity. The rate dependence provides an additional controlling factor for regulating vesicle shapes and vesicle shape transformation pathways in experiments.

Chapter 5

Domain growth and interactions in a fluid vesicle

5.1 Introduction

Recently, phase separation dynamics in multi-component (mixture of lipids) fluid vesicles have attracted considerable attentions [13, 14, 46-48, 118, 127-129] largely motivated by the discovery of lipid raft. Lipid rafts are defined as sterol- and sphingolipid-enriched lateral organizations found in plasma membranes with size ranging from 10 to 200 nm [37, 130, 131]. Increasing evidences have shown that such microdomains play an important role in regulating numerous cellular processes including cell polarity, protein trafficking, and signal transduction. Despite of the biological significance continuously being discovered, some fundamental issues of lipid raft, such as finite domain size, remain a matter of debate. Both experiments and coarse-grained molecular dynamics simulations have reproduced the formation of microdomains in model membranes [38, 128] and shown that phase separation leads to domain formations. Using fluorescence microscopy to observe ternary vesicles consisting of cholesterols, unsaturated and saturated lipids has become a standard experimental method to study domain formations. Quenching the ternary vesicle below a miscibility transition temperature leads to the separation of two phases: a liquid-ordered phase composed of saturated lipids and cholesterols and liquid-disordered phase consisting of unsaturated lipids. It has long been postulated that such a phase separation is a result of minimizing the line tension between two phases [132]. Phase separation is a classical topic in statistical mechanics; completely separated two phases are the most stable state if only the line tension dominates in the total free energy. However, lipid rafts are dispersed microdomains in plasma membrane with stable finite sizes in experimentally or biologically relevant time scale. Such a puzzle stimulated a reminiscent look at phase separation dynamics in recent years [14, 46, 48, 128].

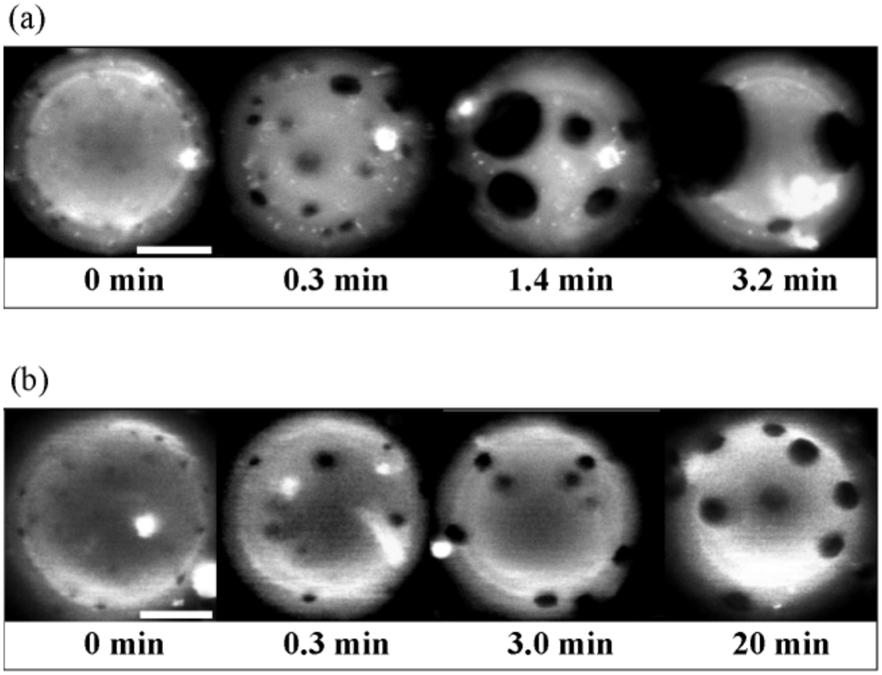

Figure 5.1. Two different coarsening speeds in giant ternary vesicles using fluorescence microscopy. (a) Normal coarsening, (b) slower coarsening. Reprinted with permission from [128]. Copyright 2007 Biophysical Society.

In general, phase separation in fluid membranes follows a diffusion-coalescence manner. The diffusion of finite size domains in fluid membranes has been hypothesized to be affected in several scenarios. Using large-scale dissipative particle dynamics, Laradji and Kumar studied the effects of hydrodynamics, vesicle area-to-volume ratio constraints [48], and asymmetric transbilayer lipid distribution [46] on the phase separation dynamics on self-assembled binary vesicles, particularly focusing on the anomalous slow down of phase separation. Recently, Yanagisawa et al. observed two different coarsening speeds in giant ternary vesicles using fluorescence microscopy. They found that in vesicles with flat domains (domains have the same curvature as vesicles), complete phase separation occurred within several minutes, while in vesicles with budding domains (domains are cap-shaped), domain coarsening was substantially slower, as shown in Figure 5.1. They pointed out that the membrane bending between two approaching cap-shaped domains results in a repulsive interaction that hinders the diffusion-coalescence process. The membrane morphologies in the flat domain case and the budded domain case are shown in Figure 5.2. Membrane mediated elastic interaction between two curved domains on a planar fluid membrane has long been studied theoretically [133]. Very recently, Ursell et al. [14] showed a detailed theoretical and experimental study on the elastic interactions of two dimpled domains, and estimated the repulsive interaction energy in experiments.

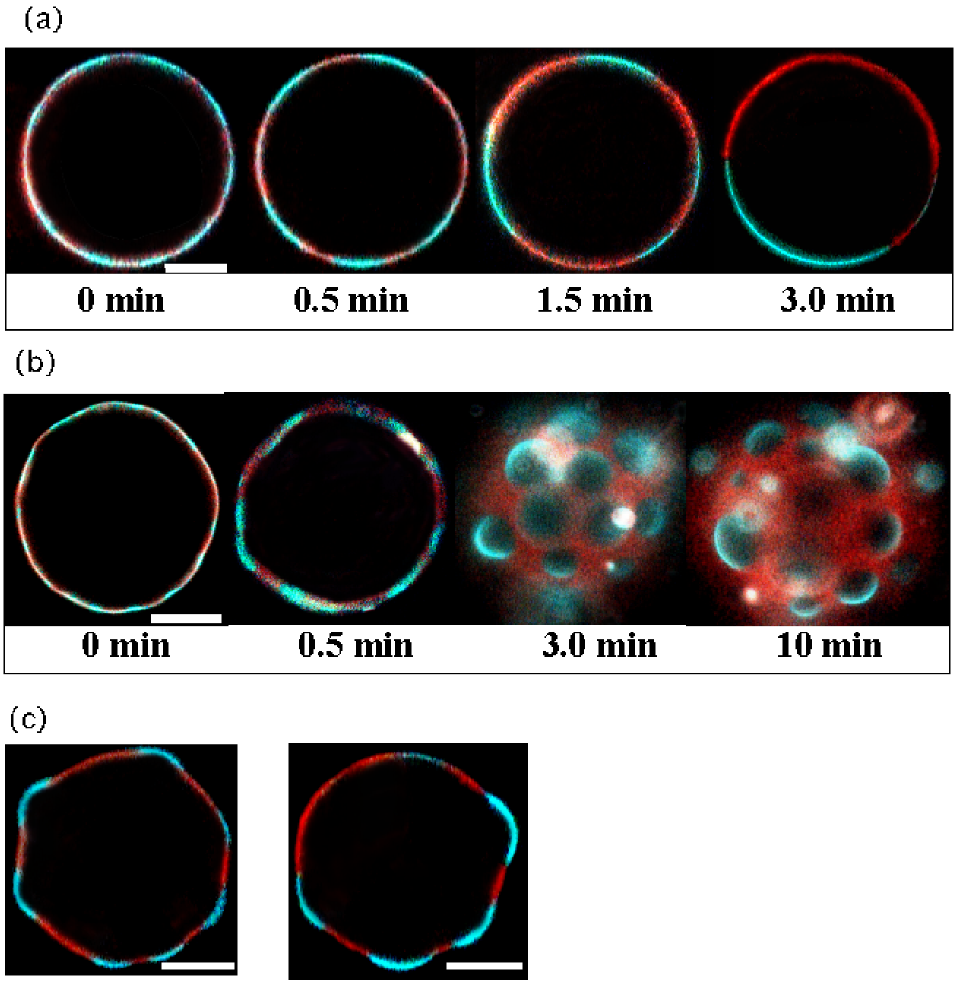

Figure 5.2. The membrane morphologies in the flat domain case (a) and the budded domain case (b) and (c).

In theoretical studies of the membrane-mediated elastic interactions between domains, in order to be mathematical tractable, several assumptions were usually made to simplify the problem, such as membrane deformation is small, there are only two domains on an infinite large planar membrane, domains are rigid. In this chapter, we study the effect of elastic interactions on domain growth in a fluid vesicle by CGMD simulations, aiming to simulate more complex experimental conditions such as large curvature and multi-domain interactions.

5.2 Simulations and preliminary results

To study the dynamics of phase separation, we randomly label particles in the vesicle as component A or B. The number ratio between component A (red) and B (green) is 1:2 and is conserved throughout simulations, so component A is the minority and clusters of type-A particles are treated as domains. The line tension between two phases is mimicked in simulations by assigning different interaction strength between AA, BB and AB pairs as: $\varepsilon^{AA} = \varepsilon$, $\varepsilon^{BB} = \varepsilon$, $\varepsilon^{AB} = 0.7\varepsilon$. The vesicle in the simulations consists of 11054 particles. The line tension induced by the AB interactions alone is not large enough to drive single domain budding. In order to explore the elastic interaction between two budding domains, spontaneous curvature of type-A component is varied to mimic different domain curvature in experimental conditions caused by either the line tension or intrinsic lipid or protein curvature. Other parameters used in the simulations are: $k_B T$ =0.23ε, η=2, ζ =4. $\mu^{\mathrm{AA}} = \mu^{\mathrm{AB}} = 6$, and $\mu^{\mathrm{BB}} = 3$, unless mentioned otherwise.

The phase separation dynamics is depicted in Figure 5.3, in which three rows from top to bottom correspond to three cases with different spontaneous curvature $\theta_0^{\mathrm{AA}} = 0.0^\circ$, $\theta_0^{\mathrm{AA}} = 2.3^\circ$, and $\theta_0^{\mathrm{AA}} = 4.6^\circ$, respectively. Dimpled domains composed of type-A particles forms in the diffusion-coalescence manner. The slope at the domain boundary increase with the spontaneous curvatures of type-A particles. The apparent slowdown of domain growth can be observed in Figure 5.3 for $\theta_0^{\mathrm{AA}} = 2.3^\circ$ and $\theta_0^{\mathrm{AA}} = 4.6^\circ$ cases. Furthermore, the larger the domain curvature, the slower the domain coarsening. Flat or budded domains in our simulations are induced by the different spontaneous curvatures, while in the experimental conditions the area-to-volume constraint induces large membrane tension in the spherical vesicle limit and thus results in flat domains. Since there is no volume constraint in our simulations, membrane tension is automatically relaxed to zero for all three cases. The simple scenario in our simulations is intentionally setup to iron out possible factors that can affect the domain coarsening. The membrane curvature change in domains and matrix induced by the budded domains seems to be the only difference between three cases. From the visual observation of the domain growth dynamics, three steps can be defined for two budded domains merging into one domain. In the first step, two domains are far enough from each other and are approaching each other due to pure diffusion. As they are closer in the second step, curved matrix membrane mediates elastic interactions between them and thus affects the diffusion. In the third step, two domains first become connected and thus undergo fast mixing into one circular domain. Even though the membrane thermal fluctuation (undulation) is faithfully taken in account in CGMD simulations, we at this point neglect its possible role of inducing long-range forces between domains [134] in our following analysis. Since the budded domains are still slightly curved, we neglect the effect of membrane morphology on the pure diffusion of domains. Two-domain merging in our simulations is a fast dynamic process due to the large line tension, thus can hardly affect the overall domain growth dynamics. Therefore, as shown in Figure 5.3, it is reasonable to believe that the matrix membrane mediates repulsive elastic interactions between two approaching curved domains which hinders the domain growth. It is interesting to see that the simulation results in Figure 5.3 closely resemble that of the experiments shown in Figure 5.1. The cross sections of the vesicles in the simulations are given in Figure 5.4, providing a visual comparison to the experimental vesicle morphologies shown in Figure 5.2.

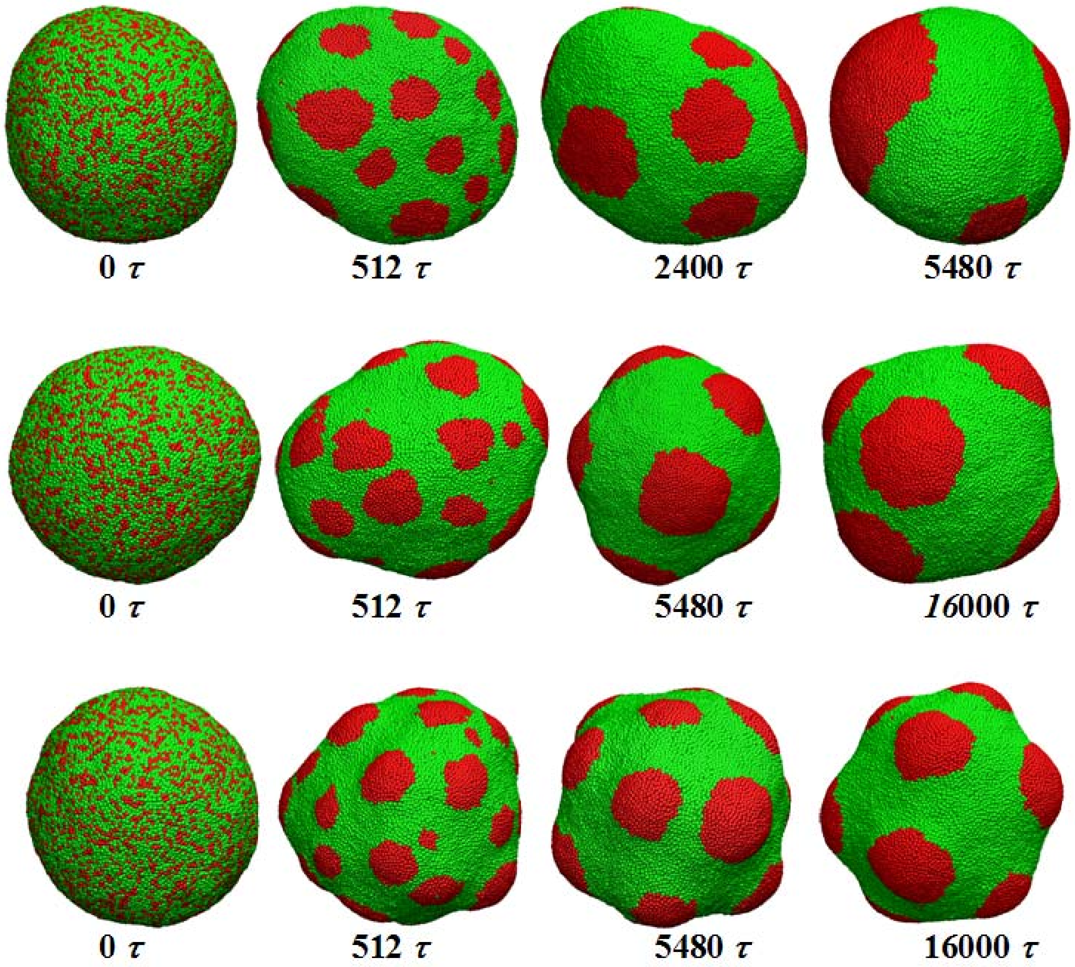
0 τ
512 τ
2400 τ
5480 τ
0 τ
512 τ
5480 τ
16000 τ
0 τ
512 τ
5480 τ
16000 τ

Figure 5.3. The phase separation dynamics. Three rows from top to bottom correspond to three different spontaneous curvature $\theta_0^{AA} = 0.0^\circ$, $\theta_0^{AA} = 2.3^\circ$, and $\theta_0^{AA} = 4.6^\circ$, respectively.

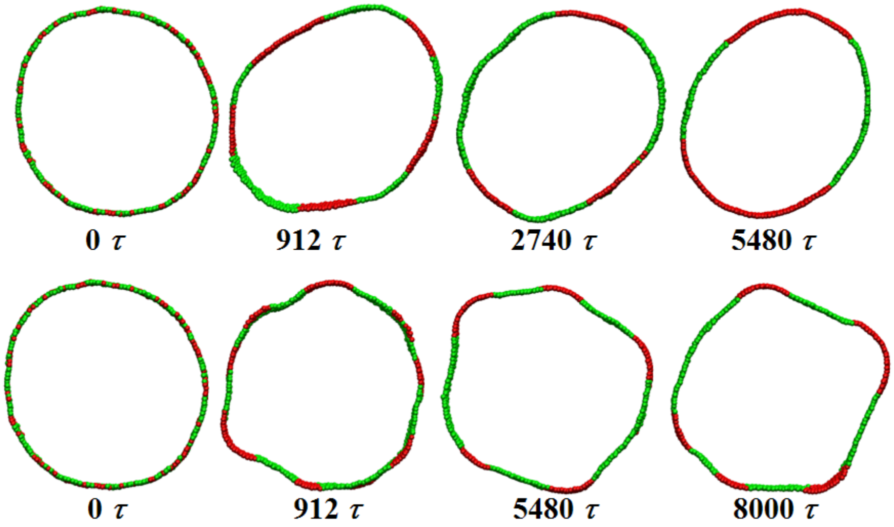

$0\ \tau$ $912\ \tau$ $2740\ \tau$ $5480\ \tau$

$0\ \tau$ $912\ \tau$ $5480\ \tau$ $8000\ \tau$

Figure 5.4. The cross sections of the vesicles in the simulations, showing curved domains and the deformed matrix membrane. Top row: $\theta_0^{\mathrm{AA}} = 0.0^\circ$, bottom row: $\theta_0^{\mathrm{AA}} = 4.6^\circ$.

In figure 5.5, the domain number N_d as a function of time t is plotted. The coarsening of all three cases obeys the same power law as $N_d \sim t^{-2/3}$ in the initial stage up to $1000\,\tau$, and then deviates from each other at different time depending on the imposed curvature. Since the amount of A and B components of the binary vesicle are conserved in the simulations, we have $R_d \sim \sqrt{\frac{A_d}{N_d}}$, where R_d is the domain size (radius) and A_d is the total domain area. Since A_d is constant if we assume the change of membrane area due to domain budding is negligible, the domain size obeys the power law $R_d \sim t^{1/3}$. The growth power law $R_d \sim t^{1/3}$ can understood as follow. Assuming that each domain is a colloidal particle with Brownian motion and the average distance between circular domains is proportional to the average domain size R_d, we have $R_d \sim \sqrt{Dt}$ [128], where D is the diffusion constant of the domains. If we further assume $D \sim 1/R_d$ in the 2D fluid (similar to the Einstein-Stokes equation for 3D), we arrive the power law $R_d \sim t^{1/3}$. It is worth mentioning that a faster domain growth was observed in the experiments as $R_d \sim t^{2/3}$ [128], which was explained by the authors as the result of two-body hydrodynamic interactions between domains.

In the experiments, domains become dimpled only when the domain size is larger than a certain value so that dimpled shape is energetically more favored than the flat shape [14, 128], and the onset time of slowing down of domain growth coincides with that of domain budding. In contrast, in our simulations domain budding starts from the beginning. However, in the initial stage where domain growth rate of case $\theta_0^{\mathrm{AA}} = 2.3^\circ$ and $\theta_0^{\mathrm{AA}} = 4.6^\circ$ exhibit no difference than that of case $\theta_0^{\mathrm{AA}} = 0.0^\circ$, a plausible explanation is that membrane mediated repulsive interactions are negligible compared with the thermal energy in the initial stage. This is supported by the theoretical studies under the small-gradient assumption that predicted the repulsive energy between two dimpled domains on a infinitely large planar membrane is proportional to the domain size and the slope at the domain boundary [14, 133]. As budded domains grow bigger in case $\theta_0^{\mathrm{AA}} = 2.3^\circ$ and $\theta_0^{\mathrm{AA}} = 4.6^\circ$, the repulsive energy becomes comparable to the thermal energy and thus set an energy barrier to slow down the approach and coalescence of domains. The repulsive energy can be roughly estimated from the delay of the domain growth using equation $\Delta E = \ln\left(t_2 / t_1\right)$, where t_2 and t_1 are the domain growth time to reach the same domain number for budded and flat domain cases, respectively.

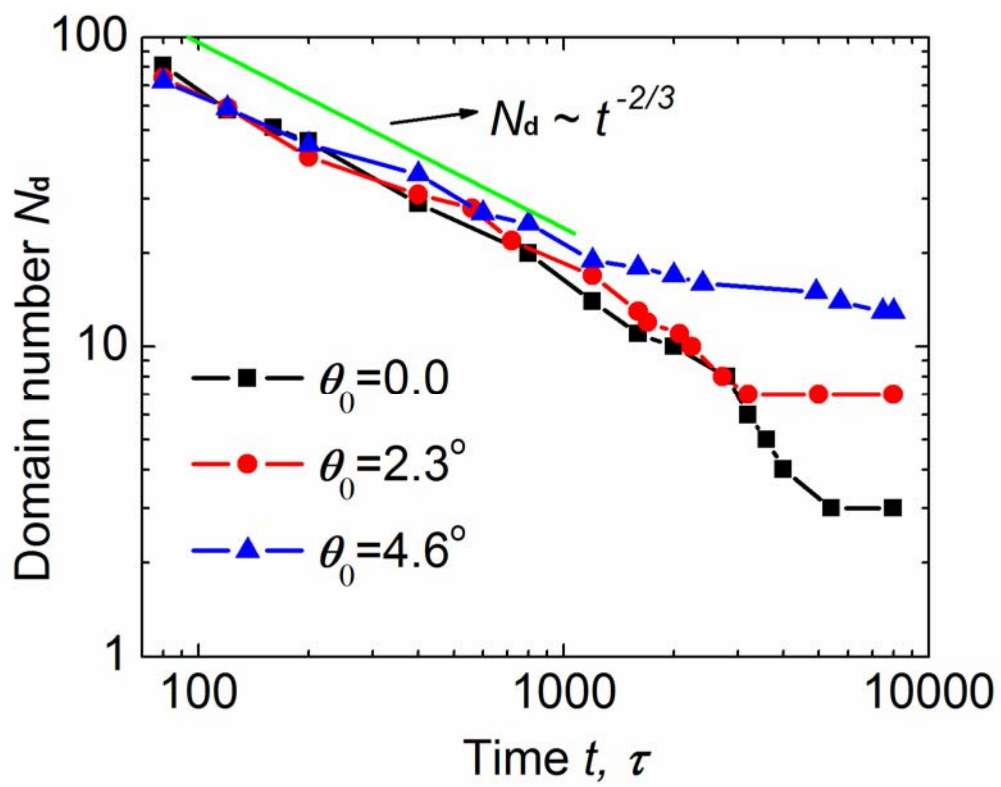

Figure 5.5. Domain number as a function of time. Three sets of data correspond to different spontaneous curvature of component A. The guide line is $N_d \sim t^{-2/3}$.

Chapter 6

Conclusions and future work

6.1 Conclusions

6.1.1 The membrane model

In this thesis, we presented an efficient solvent-free coarse-grained fluid membrane model. The mesoscopic membrane model features an orientation-dependent inter-particle potential that effectively captures the dual character of lipid membranes as solid shells with out-of-plane bending rigidity and as 2D fluids with in-plane viscosity. Particle-based models are well suited for simulating membrane topological changes and can simulate the hydrodynamics naturally. To mimic the osmotic conditions in experiments, an external potential that constrains the enclosed volume of vesicles is incorporated into the model, which enables studies of fluid vesicles under prescribed area-to-volume ratios.

As reviewed in Section 2.2.3, considerable effort in the past has been devoted to develop one- or two-particle-thick particle-based solvent-free models to obtain the highest level of coarse-graining possible. The aim of this class of models is to push the length and time scale of the mesoscopic membrane simulations to the limit. Many features of our model make it well suited for practical membrane simulations as demonstrated in Chapter 4 and 5. The features include,

- ✧ pair potential only,
- ✧ the potential is simple to follow (a distance-dependent potential with interaction strength weighed by the orientation),
- ✧ robust self-assembly into membranes,
- ✧ stable fluid phase,

- tunable membrane properties, biologically relevant bending rigidity,
- diffusion constant and bending rigidity are determined by two potential parameters thus can be tuned separately,
- being able to define the spontaneous curvature by a potential parameter,
- an efficient and robust volume control algorithm for fluid vesicles,

Most of abovementioned features are the targeted properties that previous membrane models in the class of “aggressive” solvent-free coarse-grained models attempts to capture. Developing such a solvent-free model has proven not easy. One of the reasons is that there is no systematical way to determine the form of the potential. Two aspects of our model that differ from previous such class of models are believed to be the key that leads to the success of our model in capturing the above listed features. One is the strongly biased orientation-dependence; the other is the soft-core repulsive branch.

6.1.2 Non-equilibrium shape transformations of fluid vesicles

The Equilibrium configurations of fluid vesicles have been well studied in the past decades. In contrast, the dynamic behaviors of fluid vesicles in non-equilibrium conditions are less explored. The hydrodynamics of fluid membranes and the surrounding fluid have become an active field of research. In this thesis research, we investigate the dynamic shape transformations of fluid vesicles in different volume-change rate. An interesting finding is that the dynamic shape transformation pathways depend on the volume-change rate. The in-plane shear stress was found to be non-zero in the case of fast volume change, which manifests that membrane viscosity affect the shape change dynamics. In this study, we have neglected the bulk fluid by assuming the membrane is much more viscous than the water. Our simulations may inspire experimental study on the effect of hydrodynamics on the vesicle shape change.

6.1.3 Membrane mediated interactions between domains

The membrane-mediated repulsive interactions between liquid-ordered domains in model membranes are believed to play important role in stabilize the finite domain size, which may improve the fundamental understanding of the formation of lipid raft. The study of membrane-mediated elastic interactions only involves large scale effective membrane properties. Such a problem can be adequately and faithfully investigated sing the membrane model developed here. We studied the domain growth dynamics on a fluid vesicle. The both normal and slow domain growth dynamics observed in the experiments was reproduced in our simulations. The results show that the repulsive force depends on domain size and domain curvature. As budded domains grow bigger, the repulsive energy becomes comparable to or larger than the thermal energy, and thus forms an energy barrier to slow down the approach and coalescence of domains.

6.2 Future work

6.2.1 Membrane fluctuations

Over past decades, considerable attention has been paid to simulate vesicle-substrate interactions and interpret experimentally measured membrane fluctuations of human red blood cells (RBC) at normal or disease states [73, 135-137]. Theoretical analysis of membrane fluctuations has been mainly limited to planar membranes [73] or quasi-spherical vesicles [138]. As demonstrated previously that our model faithfully reproduces fluctuation spectrum at zero and finite tensions, it stands as an ideal model for studying fluctuations of membranes in gel or fluid phase, or membrane fluctuations constrained by substrate or coupled to protein network [137].

6.2.2 Domain diffusion on a non-Euclidian 2D space

The lipid bilayer membrane exhibit highly curved morphology in endoplasmic reticulum and Golgi apparatus (see Figure 1.1), and many kinds of protein inclusions or sculpting protins present in those cellular organelles. It is interesting to study how the morphology of the membrane affects the domain diffusion. Theoretical studies of phase-ordering kinetics were inevitably in Euclidian spaces [139]. In Figure 6.1, a two-component vesicle with component A(red) and B(green) is shown. Volume control is applied to keep the vesicle in an oblate shape. Phase separation is induced by assigning different interaction strength between AA, BB and AB pairs as: $\varepsilon^{AA} = \varepsilon$, $\varepsilon^{BB} = \varepsilon$, $\varepsilon^{AB} = 0.7\varepsilon$. Potential parameters for AA and BB pair interactions are the same. Therefore, this setup is different than the scenario in Chapter 5, as there is no elastic interaction between domains. An interesting observation is found that domains (red patches) tend to locate in the rim region of the oblate vesicle. Further systematical study is ongoing.

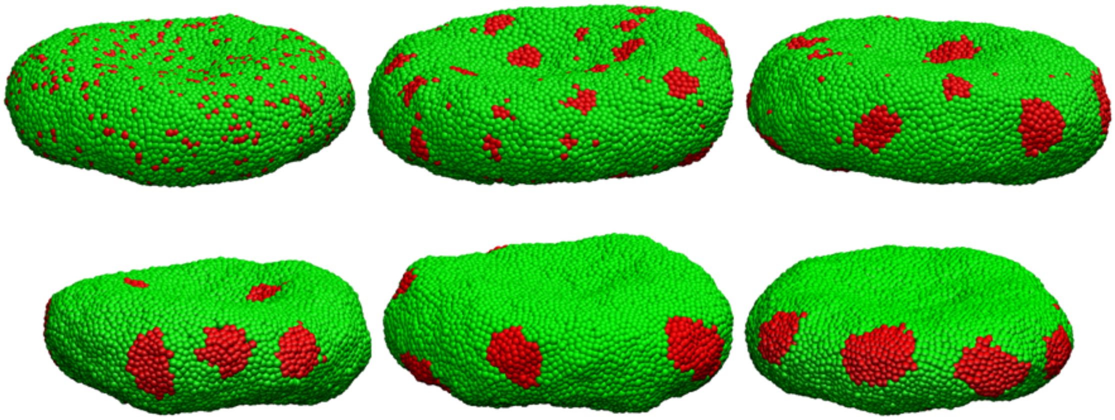

Figure 6.1. Domain diffusion on a non-Euclidian 2d space. Six snapshots in time sequence (from top to bottom, left to right) show that domains tend to locate in the rim region of the oblate vesicle.

6.2.3 Simulating nanoparticle endocytosis

Figure 9 shows four snapshots of our simulations of adhesion-driven endocytosis of nanoparticles (NP) (red). The interaction between the NP and the membrane particles is nonspecific and described by the 4-2 LJ potential with a cutoff of $3.0\,\sigma$. The parameters for membrane particles are: $k_B T = 0.23\,\varepsilon$, ζ =4, $\mu = 3.0$, $\theta_0 = 0^\circ$. The energy depth of the 4-2 LJ potential is ε, corresponding to ~4.4 $k_B T$. The total resulting adhesion energy (depending on the number of membrane particles that adhere to the NP) is sufficient to overcome the bending energy penalty ($8\pi B$) and drive NP endocytosis [140-142]. The membrane particles in blue are within the interaction range of the NP. For the clarity of visualization, the front half of the membrane model is not shown. The snapshots show the sequence of endocytosis of the NP (from left to right): docking, partial wrapping, pinching off. The NP is then internalized, while acquiring a layer of membrane particles.

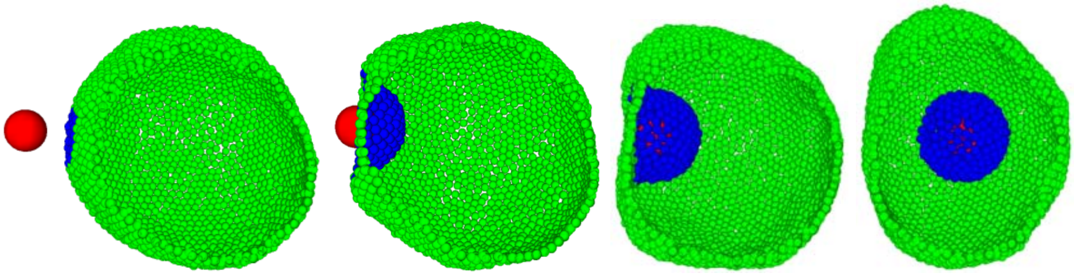

Figure 6.2. Simulation snapshots of nanoparticle endocytosis. The snapshots show the sequence of endocytosis of the NP (from left to right): docking, partial wrapping, pinching off.

6.2.4 Extending the model to dissipative particle dynamics

Intracellular environment is a complex fluid made of water, liquid crystal (bilayer), polymers (cytoskeleton), colloids (organelles), etc. Physicists have studied complex fluid for a long time. Since dissipative particle dynamics has been developed as a suitable simulation framework for studying complex fluids. An interesting future work will be to add the bulk fluid particles into the model and use dissipative particle dynamics to establish the equations of motion. In this direction, the effect of hydrodynamics of the surrounding fluid can be fully evaluated for dynamic processes such as vesicle budding, nanoparticle endocytosis. In addition, dissipative particle dynamics will replace Nose-Hoover thermostat in the current to maintain constant temperature. Dissipative particle dynamics not only can simulate hydrodynamics correctly for coarse-grained particle systems, but also is a thermostat to maintain the system temperature [51].

6.2.5 Parallelizing the MD code

Although the model is highly efficient and of high level of coarse-graining, the current serial code severely limits the system size we can simulate and thus prohibits studies involving large membranes such as tethering. It is planned to parallelize the code in the near future.

Appendix

A1 Euler's equations of rigid body dynamics

Kinetically, the particles are taken to be solid particles of mass m and moment of inertia $1 \cdot m\sigma^2$. The total potential of a many-particle system containing N particles is,

$$V = \sum_{i=1}^{N-1} \sum_{j=i+1}^{N} U\left(\mathbf{r}_{ij}, \mathbf{n}_{i1}, \mathbf{n}_{j1}\right).$$

Note that in this section, three particle-fixed unit vectors $\mathbf{n}_{i1}$, $\mathbf{n}_{i2}$, and $\mathbf{n}_{i3}$ are adopted to describe the orientation of an particle in arbitrary shape, $\mathbf{n}_{i1}$ takes the role of $\mathbf{n}_i$ of the axisymmetric particles. The evolution of the system in time is governed by Newton's equation of motion,

$$m\ddot{\mathbf{r}}_i = \mathbf{F}_i = -\frac{\partial V}{\partial \mathbf{r}_i}, \tag{37}$$

and by Euler's equations for rigid body dynamics, given in the body-fixed coordinate system whose axes coincide with the principal axes of inertia (i.e., $\mathbf{n}_{i1}$, $\mathbf{n}_{i2}$, $\mathbf{n}_{i3}$),

$$\frac{d}{dt}\begin{pmatrix} I_1\Omega_{i1} \\ I_2\Omega_{i2} \\ I_3\Omega_{i3} \end{pmatrix} = \begin{pmatrix} \left(I_2 - I_3\right)\Omega_{i2}\Omega_{i3} + T_{i1} \\ \left(I_3 - I_1\right)\Omega_{i3}\Omega_{i1} + T_{i2} \\ \left(I_1 - I_2\right)\Omega_{i1}\Omega_{i2} + T_{i3} \end{pmatrix}, \tag{38}$$

where I_1, I_2, and I_3 are three principal inertial moments; Ω_{i1}, Ω_{i2}, and Ω_{i3} are instantaneous angular velocity components; T_{i1}, T_{i2}, and T_{i3} are torque components acting on particle i in the body-fixed coordinate system. Torque applied on particle i can be calculated from the total potential of the system [143],

$$\boldsymbol{\tau}_i = -\sum_{m=1}^{3} \mathbf{n}_{im} \times \frac{\partial V}{\partial \mathbf{n}_{im}}. \tag{39}$$

Torque $\boldsymbol{\tau}_i = \left(\tau_{i1}, \tau_{i2}, \tau_{i3}\right)^T$ calculated by Equation (39) is in the global-space coordinate system. It is connected with $\mathbf{T}_i = \left(T_{i1}, T_{i2}, T_{i3}\right)^T$ by a rigid-body rotation matrix $\mathbf{Q}_i$ via

$$\mathbf{T}_i = \mathbf{Q}_i^T \boldsymbol{\tau}_i \, . \tag{40}$$

Matrix $\mathbf{Q}_i$ can be substituted for Euler angles to represent the orientation of particle i at each instant. However, in molecular dynamics simulation codes, such as LAMMPS (Large-scale Atomic/Molecular Massively Parallel Simulator) [144], neither matrix $\mathbf{Q}_i$ nor Euler angles are used to describe the rotational degrees of freedom. Instead, a quaternion is defined for each particle to record the current orientation. The time evolution of the quaternion $\mathbf{q}_i = \left(q_{i0}, q_{i1}, q_{i2}, q_{i3}\right)^T$ of particle i is governed by the following equation [145],

$$\frac{d}{dt}\begin{pmatrix} q_{i0} \\ q_{i1} \\ q_{i2} \\ q_{i3} \end{pmatrix} = \frac{1}{2}\begin{pmatrix} 0 & -\Omega_{i1} & -\Omega_{i2} & -\Omega_{i3} \\ \Omega_{i1} & 0 & \Omega_{i3} & -\Omega_{i2} \\ \Omega_{i2} & -\Omega_{i3} & 0 & \Omega_{i1} \\ \Omega_{i3} & \Omega_{i2} & -\Omega_{i1} & 0 \end{pmatrix}\begin{pmatrix} q_{i0} \\ q_{i1} \\ q_{i2} \\ q_{i3} \end{pmatrix} \tag{41}$$

The rotation matrix $\mathbf{Q}_i$ is given in terms of the components of $\mathbf{q}_i$ by

$$\mathbf{Q}_i = \begin{pmatrix} \left(q_{i0}^2 + q_{i1}^2 - q_{i2}^2 - q_{i3}^2\right)/2 & q_{i1}q_{i2} - q_{i0}q_{i3} & q_{i1}q_{i3} + q_{i0}q_{i2} \\ q_{i1}q_{i2} + q_{i0}q_{i3} & \left(q_{i0}^2 - q_{i1}^2 + q_{i2}^2 - q_{i3}^2\right)/2 & q_{i2}q_{i3} - q_{i0}q_{i1} \\ q_{i1}q_{i3} - q_{i0}q_{i2} & q_{i2}q_{i3} + q_{i0}q_{i1} & \left(q_{i0}^2 - q_{i1}^2 - q_{i2}^2 + q_{i3}^2\right)/2 \end{pmatrix} \tag{42}$$

Equations (38)-to-(42) are utilized in LAMMPS to perform the time-integration of rotational degrees of freedom.

A2 Implementation of Nose-Hoover thermostat

Back in 1983, Nose proposed a rigorous methodology for molecular dynamics simulations in the canonical ensemble (*NVT*). An external degree of freedom is introduced in the system to account for the heat reservoir that is coupled with the system.

The implement algorithm widely used in molecular dynamics code was proposed by Hoover [109].

The equations of motion with Nose-Hoover temperature coupling for the model read,

$$\ddot{\mathbf{r}} = \frac{\mathbf{F}_r}{m} - \xi\dot{\mathbf{r}},$$

$$\ddot{\mathbf{n}} = \frac{\mathbf{F}_n}{I} - \xi\dot{\mathbf{n}},$$

$$\dot{\xi} = \frac{1}{Q}\left(T - T_0\right),$$

where $\mathbf{F}_r = -\frac{\partial V}{\partial \mathbf{r}_i}$, $\mathbf{F}_n = -\frac{\partial V}{\partial \mathbf{n}} + \left(\frac{\partial V}{\partial \mathbf{n}}\cdot\mathbf{n} - I\ \dot{\mathbf{n}}\cdot\dot{\mathbf{n}}\right)\mathbf{n}$, $Q = \frac{\tau_T^2 T_0}{4\pi^2}$, ξ is the friction variable introduced by Hoover [109], τ_T is the relaxation time, T_0 is the desired temperature.

To put the equations of motion in a abstract mathematic form, we have $\ddot{x} = f_m - \xi\dot{x} = a$. The numerical integration of the governing equations is implemented using the velocity Verlet algorithm [146-148], which includes the following discretized equations:

$$x_{t+\Delta t} = x_t + v_t\Delta t + \frac{1}{2}a_t\Delta t^2,$$

$$v_{t+\Delta t} = v_t + \frac{1}{2}\left(a_t + a_{t+\Delta t}\right)\Delta t.$$

Plugging $a = f_m - \xi\dot{x}$ into them, we have,

$$x_{t+\Delta t} = x_t + v_t\Delta t + \frac{1}{2}\left(f_{m-t} - \xi_t v_t\right)\Delta t^2 = x_t + v_t\Delta t\left(1 - \frac{1}{2}\xi_t\Delta t\right) + \frac{1}{2}f_{m-t}\Delta t^2,$$

$$\begin{aligned} v_{t+\Delta t} &= v_t + \frac{1}{2}\left(f_{m-t} - \xi_t v_t + f_{m-t+\Delta t} - \xi_{t+\Delta t}v_{t+\Delta t}\right)\Delta t \\ &= v_t\left(1 - \frac{1}{2}\xi_t\Delta t\right) - \frac{1}{2}\xi_{t+\Delta t}v_{t+\Delta t}\Delta t + \frac{1}{2}\left(f_{m-t} + f_{m-t+\Delta t}\right)\Delta t \end{aligned}.$$

Transformation of the last equation yields,

$$v_{t+\Delta t} = \frac{\left(1 - \frac{1}{2}\xi_t \Delta t\right)}{\left(1 + \frac{1}{2}\xi_{t+\Delta t}\Delta t\right)} v_t + \frac{1}{\left(1 + \frac{1}{2}\xi_{t+\Delta t}\Delta t\right)} \frac{1}{2}\left(f_{m-t} + f_{m-t+\Delta t}\right)\Delta t .$$

In summary, we have the following two equations,

$$x_{t+\Delta t} = x_t + v_t \Delta t \cdot factor1 + \frac{1}{2} f_{m-t} \Delta t^2 ,$$

$$v_{t+\Delta t} = factor1 \cdot factor2 \cdot v_t + factor2 \cdot \frac{1}{2}\left(f_{m-t} + f_{m-t+\Delta t}\right)\Delta t ,$$

where $factor1 = \left(1 - \frac{1}{2}\xi_{mt}\Delta t\right)$, $factor2 = \frac{1}{\left(1 + \frac{1}{2}\xi_{mt+\Delta t}\Delta t\right)}$.

Non-memory-consuming procedure of the velocity Verlet algorithm is implemented through a two-step procedure. The first half of integration reads,

$$v_{t+\Delta t/2} = v_t \cdot factor1 + \frac{1}{2} f_{m-t} \Delta t ,$$

$$x_{t+\Delta t} = x_t + v_{t+\Delta t/2} \Delta t .$$

After updating force $f_{m-t+\Delta t}$ and external variable $\xi_{t+\Delta t}$, the second half of integration is done as,

$$v_{t+\Delta t} = \left(v_{t+\Delta t/2} + \frac{1}{2} f_{mt+\Delta t} \Delta t\right) \cdot factor2 .$$

Note that if factor1 and factor2 are set to be one, then conventional velocity-verlet algorithm without Nose-Hoover thermostat is resumed, corresponding to NVE ensembles.

The central differential scheme is used to integrate the friction variable according to the equation $\dot{\xi} = \frac{1}{Q}\left(T - T_0\right) = f_\xi$, the discretized equation is $\xi_{t+\Delta t} = \xi_{t-\Delta t} + 2\Delta t f_\xi$. To start the recursion, $\xi_{-\Delta t} = \xi_0 - \Delta t f_{\xi - 0}$ is used.

A3 Membrane tension formula in one-particle-thick fluid membranes

Note that for the one-particle-thick 2D curved fluid membranes undulating in 3D space, computing membrane in-plane tension is different both in formula and in numerical implementation from the calculation of the pressure for a 3D liquid system in classical MD simulations. For a 3D liquid system (liquid particles fills up the 3D simulation box) in equilibrium (no shear stresses), the stress tensor **S** (which is the negative of the pressure tensor) is [149],

$$\mathbf{S}=\frac{1}{V}\left(-\sum_{i}^{N}m_i\mathbf{v}_i\otimes\mathbf{v}_i-\sum_{i,j>i}^{N}\mathbf{r}_{ij}\otimes\mathbf{F}_{ij}\right), \tag{43}$$

where V is the volume of the simulation box, $\mathbf{r}_{ij}=\mathbf{r}_i-\mathbf{r}_j$, $\mathbf{F}_{ij}$ is the force exerted on particle i by j. For a 2D system in 2D Euclidean space, a 2D stress tensor $\hat{\mathbf{S}}$ (in the unit of force per unit length) can be deduced from Eq. (43) as,

$$\hat{\mathbf{S}}=\frac{1}{A}\left(-\sum_{i}^{N}m_i\mathbf{v}_i\otimes\mathbf{v}_i-\sum_{i,j>i}^{N}\mathbf{r}_{ij}\otimes\mathbf{F}_{ij}\right), \tag{44}$$

where A is the area, and $\mathbf{v}_i$, $\mathbf{r}_{ij}$, $\mathbf{F}_{ij}$ are 2D vectors in Eq. (44). The 2D normal stress, which is the membrane tension Σ, can be obtained by taking the trace of the stress tensor $\hat{\mathbf{S}}$,

$$\Sigma=\frac{1}{2}\mathrm{Trace}\left(\hat{\mathbf{S}}\right). \tag{45}$$

Note that $\hat{\mathbf{S}}$ is a 2D tensor, so the numerical coefficient before $\mathrm{trace}\left(\hat{\mathbf{S}}\right)$ is $\frac{1}{2}$, instead of $\frac{1}{3}$ in the 3D case. Substituting Eq. (44) into Eq. (45), and using the identity $\mathrm{Trace}\left(\mathbf{v}_1\otimes\mathbf{v}_2\right)=\mathbf{v}_1\cdot\mathbf{v}_2$ (where $\mathbf{v}_1$ and $\mathbf{v}_2$ are arbitrary vectors), we have,

$$\Sigma=\frac{1}{2A}\left(-\sum_{i}^{N}m_i\mathbf{v}_i\cdot\mathbf{v}_i-\sum_{i,j>i}^{N}\mathbf{r}_{ij}\cdot\mathbf{F}_{ij}\right). \tag{46}$$

Equation (46) is obtained based on a statistically isotropic and homogenous 2D system in the 2D Euclidean space. The membrane in our model is one-particle-thick, which is essentially a 2D surface constructed by discrete particles. For a small membrane patch of an area A_L consisting of only a few particles, one may consider it as locally flat, and the out-of-plane stresses are negligibly small. Therefore, Eq. (46) is suited to calculate the local membrane tension $\varSigma_L$, i.e.,

$$2A_L \cdot \varSigma_L = \left(-\sum_{i}^{N_L} m_i \mathbf{v}_i \cdot \mathbf{v}_i - \sum_{i,j>i}^{N_L} \mathbf{r}_{ij} \cdot \mathbf{F}_{ij} \right) \tag{47}$$

One notes that Eq. (47) can be applied to all the membrane patches. Summing up Eq. (47) over all the patches, (this operation is valid since both sides are scalar, independent of the local coordinate system), one follows

$$\sum_L \left(2A_L \cdot \varSigma_L \right) = \left(-\sum_{i}^{N} m_i \mathbf{v}_i \cdot \mathbf{v}_i - \sum_{i,j>i}^{N} \mathbf{r}_{ij} \cdot \mathbf{F}_{ij} \right) \tag{48}$$

It has been rigorously proven that for a fluid membrane in equilibrium, membrane tension is a constant everywhere. That implies, locally calculated membrane tension is equal to the global membrane tension within the thermal fluctuation induced error, i.e., $\Sigma_L = \Sigma$ for all *L*. This follows that the left-hand side of Eq. (48) is simply $2A\varSigma$, where for curved membranes, A should be interpreted as the membrane contour area. Thus, Eq. (46) is obtained. Substituting $\sum_{i}^{N} m_i \mathbf{v}_i \cdot \mathbf{v}_i = 3Nk_{\mathrm{B}}T$ into Eq. (46), we finally obtain the Eq. (24):

$$\varSigma = \frac{1}{2A} \left(-3Nk_{\mathrm{B}}T - \sum_{i,j>i}^{N} \mathbf{r}_{ij} \cdot \mathbf{F}_{ij} \right).$$

One may think that the kinetic term $\sum_{i}^{N} m_i \mathbf{v}_i \cdot \mathbf{v}_i$ should only include the in-plane component, which means $\sum_{i}^{N} m_i \mathbf{v}_i^{\text{in-plane}} \cdot \mathbf{v}_i^{\text{in-plane}} = 2Nk_{\mathrm{B}}T$ should be included in the above equation. The term $3Nk_\mathrm{B}T$ in the above equation has been validated by performing molecular dynamics simulation in a fluid vesicle. For a fluid vesicle without the volume constraint, the equilibrium membrane tension should be zero. By calculating membrane tension of the equilibrated fluid vesicle, we confirmed that the above equation is valid.

A4 Removal of rigid body motion

We remove rigid-body translational motion using equation $\mathbf{v}_i = \mathbf{v}_i - \mathbf{v}_G$, where $\mathbf{v}_G$ is the velocity of the center-of-mass of the whole system, $\mathbf{v}_i$ is the velocity of particle i. Through this process, the center-of-mass becomes a fixed point, which coincides with the origin in our simulation setting. To remove the rigid-body rotational motion at each time step, we first calculate the inertia tensor using the following equations:

$$\mathbf{I} = \begin{bmatrix} I_{xx} & -I_{xy} & -I_{xz} \\ -I_{xy} & I_{yy} & -I_{yz} \\ -I_{xz} & -I_{yz} & I_{zz} \end{bmatrix},$$

where $I_{xx} = \sum m_i \left(y_i^2 + z_i^2\right)$, $I_{yy} = \sum m_i \left(x_i^2 + z_i^2\right)$, $I_{zz} = \sum m_i \left(x_i^2 + y_i^2\right)$, $I_{xy} = \sum m_i x_i y_i$, $I_{yz} = \sum m_i y_i z_i$, $I_{zx} = \sum m_i x_i z_i$. Then we calculate the angular momentum about the origin (the center-of-mass) $\mathbf{H} = \sum m_i \mathbf{r}_i \times \mathbf{v}_i$. Since $\mathbf{H} = \mathbf{I} \cdot \mathbf{w}$, we obtain $\mathbf{w} = \mathbf{I}^{-1} \cdot \mathbf{H}$, where $\mathbf{w}$ is the instantaneous angular velocity. Finally, we remove the rigid-body rotational motion using equation $\mathbf{v}_i = \mathbf{v}_i - \mathbf{w} \times \mathbf{r}_i$.

A5 Derivations for inter-particle forces

A compact and clear expression for forces in molecular dynamics simulations of rigid bodies has been presented by Allen and Germano [143]. The force exerted on particle i by particle j is

$$\mathbf{f}_{ij} = -\frac{\partial U}{\partial \mathbf{r}_i} = -\frac{\partial U}{\partial r}\frac{\partial r}{\partial \mathbf{r}_i} - \frac{\partial U}{\partial \hat{\mathbf{r}}_{ij}}\frac{\partial \hat{\mathbf{r}}_{ij}}{\partial \mathbf{r}_i} = -\frac{\partial U}{\partial r}\hat{\mathbf{r}}_{ij} - r^{-1}\frac{\partial U}{\partial \hat{\mathbf{r}}_{ij}} \cdot \left(\mathbf{I} - \hat{\mathbf{r}}_{ij} \otimes \hat{\mathbf{r}}_{ij}\right). \tag{49}$$

For convenience, we copy all equations of the pair potential below,

$$U\left(\mathbf{r}_{ij}, \mathbf{n}_i, \mathbf{n}_j\right) = \begin{cases} u_R\left(r\right) + \left[1 - \phi\left(\hat{\mathbf{r}}_{ij}, \mathbf{n}_i, \mathbf{n}_j\right)\right]\varepsilon \ \ , r < r_{\min} \\ u_A\left(r\right)\phi\left(\hat{\mathbf{r}}_{ij}, \mathbf{n}_i, \mathbf{n}_j\right) \ \ , r_{\min} < r < r_c \end{cases},$$

$$\phi = 1 + \mu\left[a\left(\hat{\mathbf{r}}_{ij}, \mathbf{n}_i, \mathbf{n}_j\right) - 1\right],$$

$$\begin{aligned} a &= \left(\mathbf{n}_i \times \hat{\mathbf{r}}_{ij}\right) \cdot \left(\mathbf{n}_j \times \hat{\mathbf{r}}_{ij}\right) + \sin\theta_0\left(\mathbf{n}_j - \mathbf{n}_i\right) \cdot \hat{\mathbf{r}}_{ij} - \sin^2\theta_0 \\ &= \mathbf{n}_i \cdot \mathbf{n}_j - (\mathbf{n}_i \cdot \hat{\mathbf{r}}_{ij})(\mathbf{n}_j \cdot \hat{\mathbf{r}}_{ij}) + \sin\theta_0\left(\mathbf{n}_j - \mathbf{n}_i\right) \cdot \hat{\mathbf{r}}_{ij} - \sin^2\theta_0 \end{aligned},$$

$$u\left(r\right) = \begin{cases} u_R\left(r\right) = \varepsilon\left[\left(\dfrac{r_{\min}}{r}\right)^{2\eta} - 2\left(\dfrac{r_{\min}}{r}\right)^{\eta}\right] \ , & r < r_{\min} \\ u_A\left(r\right) = -\varepsilon\cos^{2\varsigma}\left(\dfrac{\pi}{2}\dfrac{\left(r - r_{\min}\right)}{\left(r_{\mathrm{c}} - r_{\min}\right)}\right) \ , & r_{\min} < r < r_c \end{cases},$$

Below we simply list the derivation results for terms in Eq. (49).

$$\frac{\partial U}{\partial r} = \begin{cases} \varepsilon\dfrac{2\eta}{r}\left[-\left(\dfrac{r_{\min}}{r}\right)^{2\eta} + \left(\dfrac{r_{\min}}{r}\right)^{\eta}\right], r < r_{\min} \\ \phi\varepsilon\dfrac{n\pi}{\left(r_{\mathrm{c}} - r_{\min}\right)}\cos^{2n-1}\left(\dfrac{\pi}{2}\dfrac{\left(r - r_{\min}\right)}{\left(r_{\mathrm{c}} - r_{\min}\right)}\right)\sin\left(\dfrac{\pi}{2}\dfrac{\left(r - r_{\min}\right)}{\left(r_{\mathrm{c}} - r_{\min}\right)}\right), r_{\min} < r < r_{\mathrm{c}} \end{cases}.$$

$$\frac{\partial U_{ij}^P}{\partial \hat{\mathbf{r}}_{ij}} = \begin{cases} -\mu\dfrac{\partial a}{\partial \hat{\mathbf{r}}_{ij}}, r < r_{\min} \\ u_A\left(r\right)\mu\dfrac{\partial a}{\partial \hat{\mathbf{r}}_{ij}}, r_{\min} < r < r_{\mathrm{c}} \end{cases}.$$

$$\frac{\partial a}{\partial \hat{\mathbf{r}}_{ij}} = \mathbf{n}_i(\beta - \mathbf{n}_j \cdot \hat{\mathbf{r}}_{ij}) - (\beta + \mathbf{n}_i \cdot \hat{\mathbf{r}}_{ij})\mathbf{n}_j.$$

For the “torque” corresponding to $\mathbf{n}_i$ and $\mathbf{n}_j$, we have,

$$\frac{\partial U}{\partial \mathbf{n}_i} = \begin{cases} -\mu \dfrac{\partial a}{\partial \mathbf{n}_i}, r \le r_{\min} \\ u_A(r)\mu \dfrac{\partial a}{\partial \mathbf{n}_i}, r_{\min} < r \le r_{\mathrm{c}} \end{cases} .$$

$$\frac{\partial a}{\partial \mathbf{n}_i} = \mathbf{n}_j + \hat{\mathbf{r}}_{ij}(\beta - \mathbf{n}_j \cdot \hat{\mathbf{r}}_{ij}) .$$

$$\frac{\partial a}{\partial \mathbf{n}_j} = \mathbf{n}_i - \hat{\mathbf{r}}_{ij}(\beta + \mathbf{n}_i \cdot \hat{\mathbf{r}}_{ij}) .$$

References

1. Nelson, D., S. Weinberg, and T. Piran, eds. *Statistical Mechanics of Membranes and Surfaces*. Second ed. 2004, World Scientific Publishing Company.
2. Boal, D., *Mechanics of the cell*. 2002: Cambridge university press.
3. Seifert, U., Configurations of fluid membranes and vesicles. Advances in Physics. **46**: p. 13-137, (1997).
4. Lipowsky, R. and E. Sackmann, eds. *Structure and Dynamics of Membranes*. Vol. 1&2. 1995, Elsevier Science: Amesterdam.
5. Nelson, P., *Biological Physics: Energy, Information, Life*. First ed. 2003: W. H. Freeman.
6. Marrink, S.J., A.H. de Vries, and D.P. Tieleman, Lipids on the move: Simulations of membrane pores, domains, stalks and curves. Biochimica Et Biophysica Acta-Biomembranes. **1788**(1): p. 149-168, (2009).
7. Venturoli, M., M. Maddalena Sperotto, M. Kranenburg, and B. Smit, Mesoscopic models of biological membranes. Physics Reports. **437**(1-2): p. 1-54, (2006).
8. Ou-Yang, Z.-C., J.-X. Liu, and Y.-Z. Xie, *Geometric Methods in the Elastic Theory of Membranes in Liquid Crystal Phases*. Advanced Series on Theoretical Physical Science, ed. Y.-B. Dai, B.-L. Hao, and Z.-B. Su. 1999, Singapore: World Scientific Publishing Company.
9. Purcell, E.M., Life at Low Reynolds-Number. American Journal of Physics. **45**(1): p. 3-11, (1977).
10. Lim, H.W.G., M. Wortis, and R. Mukhopadhyay, Stomatocyte-discocyte-echinocyte sequence of the human red blood cell: Evidence for the bilayer-couple hypothesis from membrane mechanics. Proceedings of the National Academy of Sciences of the United States of America. **99**: p. 16766-16769, (2002).
11. Blood, P.D. and G.A. Voth, Direct observation of Bin/amphiphysin/Rvs (BAR) domain-induced membrane curvature by means of molecular dynamics simulations. Proceedings of the National Academy of Sciences of the United States of America. **103**(41): p. 15068-15072, (2006).
12. Peter, B.J., H.M. Kent, I.G. Mills, Y. Vallis, P.J.G. Butler, P.R. Evans, and H.T. McMahon, BAR domains as sensors of membrane curvature: The amphiphysin BAR structure. Science. **303**(5657): p. 495-499, (2004).
13. Ramachandran, S., M. Laradji, and P.B.S. Kumar, Lateral Organization of Lipids in Multi-component Liposomes. Journal of the Physical Society of Japan. **78**(4): p. 9, (2009).
14. Ursell, T.S., W.S. Klug, and R. Phillips, Morphology and interaction between lipid domains. Proceedings of the National Academy of Sciences of the United States of America. **106**(32): p. 13301-13306, (2009).
15. Discher, D.E. and A. Eisenberg, Polymer vesicles. Science. **297**(5583): p. 967-973, (2002).

16. Srinivas, G., D.E. Discher, and M.L. Klein, Self-assembly and properties of diblock copolymers by coarse-grain molecular dynamics. Nat Mater. **3**(9): p. 638-644, (2004).
17. Tanaka, M. and E. Sackmann, Supported membranes as biofunctional interfaces and smart biosensor platforms. Physica Status Solidi a-Applications and Materials Science. **203**(14): p. 3452-3462, (2006).
18. Kasza, K.E., A.C. Rowat, J.Y. Liu, T.E. Angelini, C.P. Brangwynne, G.H. Koenderink, and D.A. Weitz, The cell as a material. Curr Opin Cell Biol. **19**(1): p. 101-107, (2007).
19. Alberts, B., A. Johnson, J. Lewis, M. Raff, K. Roberts, and P. Walter, *Molecular Biology of the Cell*. 4th ed. 2002: Garland Science.
20. Singer, S.J. and G.L. Nicolson, Fluid Mosaic Model of Structure of Cell-Membranes. Science. **175**: p. 720-731, (1972).
21. Engelman, D.M., Membranes are more mosaic than fluid. Nature. **438**(7068): p. 578-580, (2005).
22. Butler, P.J., T.C. Tsou, J.Y.S. Li, S. Usami, and S. Chien, Rate sensitivity of shear-induced changes in the lateral diffusion of endothelial cell membrane lipids: a role for membrane perturbation in shear-induced MAPK activation. Faseb Journal. **15**(14): p. 216-+, (2001).
23. Butler, P.J., G. Norwich, S. Weinbaum, and S. Chien, Shear stress induces a time- and position-dependent increase in endothelial cell membrane fluidity. American Journal of Physiology-Cell Physiology. **280**(4): p. C962-C969, (2001).
24. McMahon, H.T. and J.L. Gallop, Membrane curvature and mechanisms of dynamic cell membrane remodelling. Nature. **438**(7068): p. 590-596, (2005).
25. Deserno, M., Mesoscopic Membrane Physics: Concepts, Simulations, and Selected Applications. Macromolecular Rapid Communications. **30**(9-10): p. 752-771, (2009).
26. Tieleman, D.P., S.J. Marrink, and H.J.C. Berendsen, A computer perspective of membranes: molecular dynamics studies of lipid bilayer systems. Bba-Rev Biomembranes. **1331**(3): p. 235-270, (1997).
27. Saiz, L. and M.L. Klein, Computer simulation studies of model biological membranes. Accounts of Chemical Research. **35**(6): p. 482-489, (2002).
28. Pandit, S.A. and H.L. Scott, Multiscale simulations of heterogeneous model membranes. Biochimica Et Biophysica Acta-Biomembranes. **1788**(1): p. 136-148, (2009).
29. Bennun, S.V., M.I. Hoopes, C.Y. Xing, and R. Faller, Coarse-grained modeling of lipids. Chemistry and Physics of Lipids. **159**(2): p. 59-66, (2009).
30. Noguchi, H., Membrane Simulation Models from Nanometer to Micrometer Scale. Journal of the Physical Society of Japan. **78**(4): p. 9, (2009).
31. Ayton, G.S. and G.A. Voth, Hybrid Coarse-Graining Approach for Lipid Bilayers at Large Length and Time Scales. Journal of Physical Chemistry B. **113**(13): p. 4413-4424, (2009).
32. Liu, W.K., E.G. Karpov, S. Zhang, and H.S. Park, An introduction to computational nanomechanics and materials. Computer Methods in Applied Mechanics and Engineering. **193**: p. 1529-1578, (2004).

33. Zhang, S.L., W.K. Liu, and R.S. Ruoff, Atomistic simulations of double-walled carbon nanotubes (DWCNTs) as rotational bearings. Nano Letters. **4**: p. 293-297, (2004).
34. Zhang, S.L., H.T. Johnson, G.J. Wagner, W.K. Liu, and K.J. Hsia, Stress generation mechanisms in carbon thin films grown by ion-beam deposition. Acta Materialia. **51**(17): p. 5211-5222, (2003).
35. Zhong, Y. and T. Zhu, Simulating nanoindentation and predicting dislocation nucleation using interatomic potential finite element method. Computer Methods in Applied Mechanics and Engineering. **197**(41-42): p. 3174-3181, (2008).
36. Gullapalli, R.R., M.C. Demirel, and P.J. Butler, Molecular dynamics simulations of DiI-C-18(3) in a DPPC lipid bilayer. Physical Chemistry Chemical Physics. **10**(24): p. 3548-3560, (2008).
37. Simons, K. and W.L.C. Vaz, Model systems, lipid rafts, and cell membranes. Annual Review of Biophysics and Biomolecular Structure. **33**: p. 269-295, (2004).
38. Risselada, H.J. and S.J. Marrink, The molecular face of lipid rafts in model membranes. Proceedings of the National Academy of Sciences of the United States of America. **105**(45): p. 17367-17372, (2008).
39. Noguchi, H. and M. Takasu, Fusion pathways of vesicles: A Brownian dynamics simulation. Journal of Chemical Physics. **115**(20): p. 9547-9551, (2001).
40. Gao, L.H., R. Lipowsky, and J. Shillcock, Tension-induced vesicle fusion: pathways and pore dynamics. Soft Matter. **4**(6): p. 1208-1214, (2008).
41. Marrink, S.J., H.J. Risselada, S. Yefimov, D.P. Tieleman, and A.H. de Vries, The MARTINI force field: Coarse grained model for biomolecular simulations. Journal of Physical Chemistry B. **111**(27): p. 7812-7824, (2007).
42. Ayton, G. and G.A. Voth, Bridging microscopic and mesoscopic simulations of lipid bilayers. Biophysical Journal. **83**(6): p. 3357-3370, (2002).
43. Goetz, R., G. Gompper, and R. Lipowsky, Mobility and elasticity of self-assembled membranes. Physical Review Letters. **82**(1): p. 221-224, (1999).
44. Goetz, R. and R. Lipowsky, Computer simulations of bilayer membranes: Self-assembly and interfacial tension. Journal of Chemical Physics. **108**(17): p. 7397-7409, (1998).
45. Li, X.J., I.V. Pivkin, H.J. Liang, and G.E. Karniadakis, Shape Transformations of Membrane Vesicles from Amphiphilic Triblock Copolymers: A Dissipative Particle Dynamics Simulation Study. Macromolecules. **42**(8): p. 3195-3200, (2009).
46. Laradji, M. and P.B. Kumar, Anomalously slow domain growth in fluid membranes with asymmetric transbilayer lipid distribution. Physical Review E. **73**: p. 040901, (2006).
47. Laradji, M. and P.B.S. Kumar, Domain growth, budding, and fission in phase-separating self-assembled fluid bilayers. Journal of Chemical Physics. **123**: p. 10, (2005).
48. Laradji, M. and P.B. Sunil Kumar, Dynamics of domain growth in self-assembled fluid vesicles. Physical Review Letters. **93**(19): p. 198105, (2004).

49. Hoogerbrugge, P.J. and J. Koelman, Simulating Microscopic Hydrodynamic Phenomena with Dissipative Particle Dynamics. Europhysics Letters. **19**(3): p. 155-160, (1992).
50. Espanol, P. and P. Warren, Statistical-Mechanics of Dissipative Particle Dynamics. Europhysics Letters. **30**(4): p. 191-196, (1995).
51. Soddemann, T., B. Dunweg, and K. Kremer, Dissipative particle dynamics: A useful thermostat for equilibrium and nonequilibrium molecular dynamics simulations. Physical Review E. **68**(4): p. 8, (2003).
52. Noguchi, H. and M. Takasu, Self-assembly of amphiphiles into vesicles: A Brownian dynamics simulation. Physical Review E. **64**(4): p. 041913, (2001).
53. Farago, O., "Water-free" computer model for fluid bilayer membranes. Journal of Chemical Physics. **119**(1): p. 596-605, (2003).
54. Wang, Z.J. and D. Frenkel, Modeling flexible amphiphilic bilayers: A solvent-free off-lattice Monte Carlo study. Journal of Chemical Physics. **122**(23): p. 234711, (2005).
55. Cooke, I.R. and M. Deserno, Solvent-free model for self-assembling fluid bilayer membranes: Stabilization of the fluid phase based on broad attractive tail potentials. J Chem Phys. **123**(22): p. 224710, (2005).
56. Brannigan, G., P.F. Philips, and F.L.H. Brown, Flexible lipid bilayers in implicit solvent. Physical Review E. **72**(1): p. 011915, (2005).
57. Revalee, J.D., M. Laradji, and P.B.S. Kumar, Implicit-solvent mesoscale model based on soft-core potentials for self-assembled lipid membranes. Journal of Chemical Physics. **128**(3): p. 9, (2008).
58. Sintes, T. and A. Baumgartner, Protein attraction in membranes induced by lipid fluctuations. Biophysical Journal. **73**(5): p. 2251-2259, (1997).
59. Lenz, O. and F. Schmid, A simple computer model for liquid lipid bilayers. Journal of Molecular Liquids. **117**(1-3): p. 147-152, (2005).
60. Gay, J.G. and B.J. Berne, MODIFICATION OF THE OVERLAP POTENTIAL TO MIMIC A LINEAR SITE-SITE POTENTIAL. J Chem Phys. **74**(6): p. 3316-3319, (1981).
61. Berardi, R., C. Fava, and C. Zannoni, A Gay-Berne potential for dissimilar biaxial particles. Chem Phys Lett. **297**(1-2): p. 8-14, (1998).
62. Drouffe, J.M., A.C. Maggs, and S. Leibler, COMPUTER-SIMULATIONS OF SELF-ASSEMBLED MEMBRANES. Science. **254**(5036): p. 1353-1356, (1991).
63. Brannigan, G. and F.L.H. Brown, Solvent-free simulations of fluid membrane bilayers. Journal of Chemical Physics. **120**(2): p. 1059-1071, (2004).
64. Ballone, P. and M.G. Del Popolo, Simple models of complex aggregation: Vesicle formation by soft repulsive spheres with dipolelike interactions. Physical Review E. **73**(3): p. 031404, (2006).
65. Kohyama, T., Simulations of flexible membranes using a coarse-grained particle-based model with spontaneous curvature variables. Physica a-Statistical Mechanics and Its Applications. **388**(17): p. 3334-3344, (2009).
66. Noguchi, H. and G. Gompper, Shape transitions of fluid vesicles and red blood cells in capillary flows. Proceedings of the National Academy of Sciences of the United States of America. **102**(40): p. 14159-14164, (2005).

67. Discher, D.E., D.H. Boal, and S.K. Boey, Simulations of the erythrocyte cytoskeleton at large deformation. II. Micropipette aspiration. Biophysical Journal. **75**(3): p. 1584-1597, (1998).
68. Das, S. and J.T. Jenkins, An analysis of micropipette aspiration of one-phase and two-phase vesicles. Biophysical Journal: p. 584A-584A, (2007).
69. Brochard-Wyart, F., N. Borghi, D. Cuvelier, and P. Nassoy, Hydrodynamic narrowing of tubes extruded from cells. Proceedings of the National Academy of Sciences of the United States of America. **103**: p. 7660-7663, (2006).
70. Cuvelier, D., I. Derenyi, P. Bassereau, and P. Nassoy, Coalescence of membrane tethers: experiments, theory, and applications. Biophysical Journal. **88**(4): p. 2714-2726, (2005).
71. Farago, O., Membrane fluctuations near a plane rigid surface. Physical Review E. **78**(5): p. 9, (2008).
72. Evans, J., W. Gratzer, N. Mohandas, K. Parker, and J. Sleep, Fluctuations of the red blood cell membrane: Relation to mechanical properties and lack of ATP dependence. Biophysical Journal. **94**(10): p. 4134-4144, (2008).
73. Auth, T., S.A. Safran, and N.S. Gov, Fluctuations of coupled fluid and solid membranes with application to red blood cells. Physical Review E. **76**(5): p. 18, (2007).
74. Fischer, T.M., Shape memory of human red blood cells. Biophysical Journal. **86**(5): p. 3304-3313, (2004).
75. Li, J., G. Lykotrafitis, M. Dao, and S. Suresh, Cytoskeletal dynamics of human erythrocyte. Proceedings of the National Academy of Sciences of the United States of America. **104**(12): p. 4937-4942, (2007).
76. Timoshenko, S. and S. Woinowsky-Krieger, *Theory of plates and shells*. 2d ed. Engineering societies monographs. 1959: McGraw-Hill.
77. Fung, Y.C.B. and P. Tong, Theory of Sphering of Red Blood Cells. Biophysical Journal. **8**: p. &, (1968).
78. Canham, P.B., Minimum Energy of Bending as a Possible Explanation of Biconcave Shape of Human Red Blood Cell. Journal of Theoretical Biology. **26**(1): p. 61-81, (1970).
79. Helfrich, W., Elastic Properties of Lipid Bilayers - Theory and Possible Experiments. Zeitschrift Fur Naturforschung C-a Journal of Biosciences. **C 28**: p. 693-703, (1973).
80. Seifert, U., K. Berndl, and R. Lipowsky, Shape Transformations of Vesicles - Phase-Diagram for Spontaneous-Curvature and Bilayer-Coupling Models. Physical Review A. **44**(2): p. 1182-1202, (1991).
81. Brochard, F. and J.F. Lennon, Frequency Spectrum of Flicker Phenomenon in Erythrocytes. Journal De Physique. **36**(11): p. 1035-1047, (1975).
82. Engelhardt, H., H.P. Duwe, and E. Sackmann, *Bilayer bending elasticity measured by Fourier analysis of thermally excited surface undulations of flaccid vesicles*. 1985, HAL - CCSD.
83. Zilker, A., H. Engelhardt, and E. Sackmann, *Dynamic reflection interference contrast (RIC-) microscopy : a new method to study surface excitations of cells and to measure membrane bending elastic moduli*. 1987, HAL - CCSD.

84. Peterson, M.A., H. Strey, and E. Sackmann, Theoretical and Phase-Contrast Microscopic Eigenmode Analysis of Erythrocyte Flicker - Amplitudes. Journal De Physique Ii. **2**(5): p. 1273-1285, (1992).
85. Duwe, H.P., J. Kaes, and E. Sackmann, Bending Elastic-Moduli of Lipid Bilayers - Modulation by Solutes. Journal De Physique. **51**(10): p. 945-962, (1990).
86. Helfrich, W. and R.M. Servuss, Undulations, Steric Interaction and Cohesion of Fluid Membranes. Nuovo Cimento Della Societa Italiana Di Fisica D-Condensed Matter Atomic Molecular and Chemical Physics Fluids Plasmas Biophysics. **3**(1): p. 137-151, (1984).
87. Schwarz, U., Soft matters in cell adhesion: rigidity sensing on soft elastic substrates. Soft Matter. **3**(3): p. 263-266, (2007).
88. Tittmann, B.R., C. Miyasaka, A.M. Mastro, and R.R. Mercer, Study of cellular adhesion with scanning acoustic microscopy. Ieee Transactions on Ultrasonics Ferroelectrics and Frequency Control. **54**(8): p. 1502-1513, (2007).
89. Evans, E. and W. Rawicz, Entropy-Driven Tension and Bending Elasticity in Condensed-Fluid Membranes. Physical Review Letters. **64**(17): p. 2094-2097, (1990).
90. Arroyo, M. and A. DeSimone, Relaxation dynamics of fluid membranes. Physical Review E. **79**(3): p. 031915, (2009).
91. Hu, D., P.W. Zhang, and W. E, Continuum theory of a moving membrane. Physical Review E. **75**(4): p. 11, (2007).
92. Jülicher, F. and R. Lipowsky, Shape transformations of vesicles with intramembrane domains. Physical Review E. **53**(3): p. 2670, (1996).
93. Gompper, G. and D.M. Kroll, Network models of fluid, hexatic and polymerized membranes. Journal of Physics-Condensed Matter. **9**(42): p. 8795-8834, (1997).
94. Feng, F. and W.S. Klug, Finite element modeling of lipid bilayer membranes. Journal of Computational Physics. **220**(1): p. 394-408, (2006).
95. Noguchi, H. and G. Gompper, Meshless membrane model based on the moving least-squares method. Physical Review E. **73**(2): p. 021903, (2006).
96. Atilgan, E. and S.X. Sun, Shape transitions in lipid membranes and protein mediated vesicle fusion and fission. Journal of Chemical Physics. **126**(9): p. 095102, (2007).
97. Dobereiner, H.G., G. Gompper, C.K. Haluska, D.M. Kroll, P.G. Petrov, and K.A. Riske, Advanced flicker spectroscopy of fluid membranes. Physical Review Letters. **91**(4): p. 4, (2003).
98. Li, J., M. Dao, C.T. Lim, and S. Suresh, Spectrin-level modeling of the cytoskeleton and optical tweezers stretching of the erythrocyte. Biophys J. **88**(5): p. 3707-3719, (2005).
99. Dao, M., J. Li, and S. Suresh, Molecularly based analysis of deformation of spectrin network and human erythrocyte. Materials Science & Engineering C-Biomimetic and Supramolecular Systems. **26**(8): p. 1232-1244, (2006).
100. Chen, L.Q., Phase-field models for microstructure evolution. Annual Review of Materials Research. **32**: p. 113-140, (2002).

101. Gao, L.T., X.Q. Feng, and H.J. Gao, A phase field method for simulating morphological evolution of vesicles in electric fields. Journal of Computational Physics. **228**(11): p. 4162-4181, (2009).
102. Biben, T., K. Kassner, and C. Misbah, Phase-field approach to three-dimensional vesicle dynamics. Physical Review E. **72**(4): p. 041921, (2005).
103. Du, Q., C. Liu, and X.Q. Wang, A phase field approach in the numerical study of the elastic bending energy for vesicle membranes. Journal of Computational Physics. **198**(2): p. 450-468, (2004).
104. Du, Q., C. Liu, and X.Q. Wang, Simulating the deformation of vesicle membranes under elastic bending energy in three dimensions. Journal of Computational Physics. **212**(2): p. 757-777, (2006).
105. Zhang, J., S. Das, and Q. Du, A phase field model for vesicle-substrate adhesion. Journal of Computational Physics. **228**(20): p. 7837-7849, (2009).
106. Everaers, R. and M.R. Ejtehadi, Interaction potentials for soft and hard ellipsoids. Phys Rev E. **67**(4), (2003).
107. Ginsberg, J.H., *Advanced engineering dynamics*. 2nd ed. 1995: Cambridge University Press.
108. Nose, S., A Molecular-Dynamics Method for Simulations in the Canonical Ensemble. Molecular Physics. **52**: p. 255-268, (1984).
109. Hoover, W.G., CANONICAL DYNAMICS - EQUILIBRIUM PHASE-SPACE DISTRIBUTIONS. Phys Rev A. **31**(3): p. 1695-1697, (1985).
110. Berendsen, H.J.C., J.P.M. Postma, W.F. Vangunsteren, A. Dinola, and J.R. Haak, Molecular-Dynamics with Coupling to an External Bath. Journal of Chemical Physics. **81**(8): p. 3684-3690, (1984).
111. Lee, H.J., E.L. Peterson, R. Phillips, W.S. Klug, and P.A. Wiggins, Membrane shape as a reporter for applied forces. Proceedings of the National Academy of Sciences of the United States of America. **105**(49): p. 19253-19257, (2008).
112. Greengard, L. and J.Y. Lee, Accelerating the nonuniform fast Fourier transform. Siam Review. **46**(3): p. 443-454, (2004).
113. Sheetz, M.P. and S.J. Singer, Biological-Membranes as Bilayer Couples - Molecular Mechanism of Drug-Erythrocyte Interactions. Proceedings of the National Academy of Sciences of the United States of America. **71**(11): p. 4457-4461, (1974).
114. Reynwar, B.J., G. Illya, V.A. Harmandaris, M.M. Muller, K. Kremer, and M. Deserno, Aggregation and vesiculation of membrane proteins by curvature-mediated interactions. Nature. **447**(7143): p. 461-464, (2007).
115. Seifert, U., Curvature-Induced Lateral Phase Segregation in 2-Component Vesicles. Physical Review Letters. **70**(9): p. 1335-1338, (1993).
116. Fahey, P.F. and W.W. Webb, Lateral Diffusion in Phospholipid Bilayer Membranes and Multilamellar Liquid-Crystals. Biochemistry. **17**(15): p. 3046-3053, (1978).
117. Ericksen, J.L., On the Cauchy-Born rule. Mathematics and Mechanics of Solids. **13**(3-4): p. 199-220, (2008).

118. Yanagisawa, M., M. Imai, and T. Taniguchi, Shape deformation of ternary vesicles coupled with phase separation. Physical Review Letters. **100**(14): p. 148102, (2008).
119. Baumgart, T., S.T. Hess, and W.W. Webb, Imaging coexisting fluid domains in biomembrane models coupling curvature and line tension. Nature. **425**(6960): p. 821-824, (2003).
120. Baumgart, T., S. Das, W.W. Webb, and J.T. Jenkins, Membrane elasticity in giant vesicles with fluid phase coexistence. Biophysical Journal. **89**: p. 1067-1080, (2005).
121. Torchilin, V.P., Recent advances with liposomes as pharmaceutical carriers. Nat Rev Drug Discov. **4**(2): p. 145-160, (2005).
122. Sackmann, E., Supported membranes: Scientific and practical applications. Science. **271**(5245): p. 43-48, (1996).
123. Kas, J. and E. Sackmann, Shape Transitions and Shape Stability of Giant Phospholipid-Vesicles in Pure Water Induced by Area-to-Volume Changes. Biophysical Journal. **60**(4): p. 825-844, (1991).
124. Radler, J.O., T.J. Feder, H.H. Strey, and E. Sackmann, FLUCTUATION ANALYSIS OF TENSION-CONTROLLED UNDULATION FORCES BETWEEN GIANT VESICLES AND SOLID SUBSTRATES. Phys Rev E. **51**(5): p. 4526-4536, (1995).
125. Albersdorfer, A., T. Feder, and E. Sackmann, Adhesion-induced domain formation by interplay of long-range repulsion and short-range attraction force: A model membrane study. Biophysical Journal. **73**: p. 245-257, (1997).
126. Shillcock, J.C. and R. Lipowsky, The computational route from bilayer membranes to vesicle fusion. Journal of Physics-Condensed Matter. **18**(28): p. S1191-S1219, (2006).
127. Kumar, P.B.S., G. Gompper, and R. Lipowsky, Budding dynamics of multicomponent membranes. Physical Review Letters. **86**(17): p. 3911-3914, (2001).
128. Yanagisawa, M., M. Imai, T. Masui, S. Komura, and T. Ohta, Growth dynamics of domains in ternary fluid vesicles. Biophysical Journal. **92**(1): p. 115-125, (2007).
129. Gomez, J., F. Sagues, and R. Reigada, Actively maintained lipid nanodomains in biomembranes. Phys Rev E. **77**(2), (2008).
130. Jacobson, K., O.G. Mouritsen, and R.G.W. Anderson, Lipid rafts: at a crossroad between cell biology and physics. Nat Cell Biol. **9**(1): p. 7-14, (2007).
131. Edidin, M., The state of lipid rafts: From model membranes to cells. Annual Review of Biophysics and Biomolecular Structure. **32**: p. 257-283, (2003).
132. Rietveld, A. and K. Simons, The differential miscibility of lipids as the basis for the formation of functional membrane rafts. Biochimica et Biophysica Acta (BBA) - Reviews on Biomembranes. **1376**(3): p. 467-479, (1998).
133. Weikl, T.R., M.M. Kozlov, and W. Helfrich, Interaction of conical membrane inclusions: Effect of lateral tension. Physical Review E. **57**(6): p. 6988-6995, (1998).

134. Goulian, M., R. Bruinsma, and P. Pincus, Long-Range Forces in Heterogeneous Fluid Membranes. Europhysics Letters. **22**(2): p. 145-150, (1993).
135. Strey, H. and M. Peterson, Measurement of Erythrocyte-Membrane Elasticity by Flicker Eigenmode Decomposition. Biophysical Journal. **69**(2): p. 478-488, (1995).
136. Park, Y., C.A. Best, T. Auth, N.S. Gov, S.A. Safran, G. Popescu, S. Suresh, and M.S. Feld, Metabolic remodeling of the human red blood cell membrane. Proceedings of the National Academy of Sciences of the United States of America. **107**(4): p. 1289-1294, (2010).
137. Park, Y.K., M. Diez-Silva, G. Popescu, G. Lykotrafitis, W.S. Choi, M.S. Feld, and S. Suresh, Refractive index maps and membrane dynamics of human red blood cells parasitized by Plasmodium falciparum. Proceedings of the National Academy of Sciences of the United States of America. **105**(37): p. 13730-13735, (2008).
138. Milner, S.T. and S.A. Safran, DYNAMIC FLUCTUATIONS OF DROPLET MICROEMULSIONS AND VESICLES. Phys Rev A. **36**(9): p. 4371-4379, (1987).
139. Bray, A.J., Theory of Phase-Ordering Kinetics. Advances in Physics. **43**(3): p. 357-459, (1994).
140. Yuan, H.Y. and S.L. Zhang, Effects of particle size and ligand density on the kinetics of receptor-mediated endocytosis of nanoparticles. Applied Physics Letters. **96**(3): p. 033704, (2010).
141. Zhang, S.L., J. Li, G. Lykotrafitis, G. Bao, and S. Suresh, Size-Dependent Endocytosis of Nanoparticles. Advanced Materials. **21**(4): p. 419-424, (2009).
142. Deserno, M. and T. Bickel, Wrapping of a spherical colloid by a fluid membrane. Europhys Lett. **62**(5): p. 767-773, (2003).
143. Allen, M.P. and G. Germano, Expressions for forces and torques in molecular simulations using rigid bodies. Mol Phys. **104**(20-21): p. 3225-3235, (2006).
144. Plimpton, S., Fast Parallel Algorithms for Short-Range Molecular-Dynamics. Journal of Computational Physics. **117**(1): p. 1-19. LAMMPS WWW Site (http://lammps.sandia.gov), (1995).
145. Coutsiasy, E.A. and L. Romeroz, The Quaternions with an application to rigid body dynamics. unpublished, (1999).
146. Griebel, M., S. Knapek, and G. Zumbusch, *Numerical Simulation in Molecular Dynamics*. 2007: Springer.
147. Verlet, L., COMPUTER EXPERIMENTS ON CLASSICAL FLUIDS .I. THERMODYNAMICAL PROPERTIES OF LENNARD-JONES MOLECULES. Phys Rev. **159**(1): p. 98-&, (1967).
148. Verlet, L., COMPUTER EXPERIMENTS ON CLASSICAL FLUIDS .2. EQUILIBRIUM CORRELATION FUNCTIONS. Phys Rev. **165**(1): p. 201-&, (1968).
149. Zhou, M., A new look at the atomic level virial stress: on continuum-molecular system equivalence. Proc Roy Soc London Ser A. **459**(2037): p. 2347-2392, (2003).

Curriculum Vitae

Hongyan Yuan

EDUCATION

PhD, Engineering Science and Mechanics, Pennsylvania State University, University Park, Pennsylvania, August 2010. Dissertation: "A Solvent-Free Coarse-Grained Model for Biological and Biomimetic Fluid Membranes" Advisor: Dr. Sulin Zhang

MS, Mechanical Engineering, University of Alaska Fairbanks, Fairbanks, Alaska, 2007. Thesis: "Stochastic Reconstruction of Snow Microstructure from X-Ray Microtomography Images" Advisor: Dr. Jonah H. Lee

BEng, Engineering Mechanics, Tsinghua University, Beijing, China, 2002.

PUBLICATIONS

Yuan, H., C. Huang, J. Li, G. Lykotrafitis, and S. Zhang, One-particle-thick, solvent-free, coarse-grained model for biological and biomimetic fluid membranes. Physical Review E. 82(1): p. 011905, (2010).

Yuan, H., C. Huang, and S. Zhang, Dynamic Shape Transformations of fluid vesicles. Soft Matter. (in press), (2010).

Yuan, H., J.H. Lee, and J.E. Guilkey, Stochastic reconstruction of the microstructure of equilibrium form snow and computation of effective elastic properties. Journal of Glaciology. 56(197): p. 12, (2010).

Yuan, H. and S. Zhang, Effects of particle size and ligand density on the kinetics of receptor-mediated endocytosis of nanoparticles. Applied Physics Letters. 96(3): p. 033704, (2010).

Yuan, H., C. Huang, and S. Zhang, Elastic interactions and growth dynamics of dispersed domains on a binary fluid vesicle. In writting, (2010).

Yuan, H., J. Li, and S. Zhang, Variable Nanoparticle-Cell Adhesion Strength Regulates Cellular Uptake. Physical Review Letters. In review, (2010).

Yuan, H. and S. Zhang, Virus-Inspired Design Maps of Nanoparticle-Based Bioagents. PLoS ONE. (Submitted), (2010).

Huang, C., H. Yuan, and S. Zhang, Coupled Shape Transformation and Phase Separation in Binary Vesicles. Submitted, (2010).

Huang, X., H. Yuan, K.J. Hsia, and S. Zhang, Coordinated Buckling of Thick Multi-Walled Carbon Nanotubes Under Uniaxial Compression. Nano Research. 3(1): p. 32-42, (2010).

Huang, X., H. Yuan, W. Liang, and S. Zhang, Mechanical Properties and Deformation Morphologies of Covalently Bridged Multi-Walled Carbon Nanotubes: Multiscale Modeling. Journal of the Mechanics and Physics of Solids. In press, (2010).

Terdalkar, S.S., S. Huang, H. Yuan, J.J. Rencis, T. Zhu, and S. Zhang, Nanoscale fracture in graphene. Chemical Physics Letters. 494(4-6): p. 218-222, (2010).